Radiative corrections to hadrons-photons interactions

Ph.D. Thesis

Szymon Tracz

Supervisor: prof. dr hab. Henryk Czyż

University of Silesia
Institute of Physics
Division of Field Theory and Elementary Particle Physics

Katowice, 2018

Abstract

In this thesis the results of theoretical calculations for the electron-positron annihilation into hadrons and photons are presented. The wide range of the subjects is covered with the emphasis on the calculations of the radiative corrections and its implementation in the PHOKHARA Monte Carlo event generator. The important part of this thesis constitutes the modeling of the interactions of hadrons with photons.

The subjects important from the point of view of the discrepancy between experimental value and the Standard Model predictions of the the anomalous magnetic moment of the muon are presented. One of them is modeling of the two-photon pseudoscalar mesons transition form factors, which have an impact for determination of the hadronic light-by-light contribution. The second, calculations of the next-to-leading-order radiative corrections for the pion pair production cross section, which are important input for the data analysis of the BABAR and KLOE measurements, where one observes the discrepancy.

The another subject considered in this thesis, is connected with the photon radius puzzle. The modeling of the nucleon form factors is the first step in calculation of the complete radiative corrections to the electron-proton scattering as the two-photon contributions to this reaction involve knowledge of the proton transition form factors.

The last subject covers the production of the states with even charge conjugation and parity. The model for electronic widths of the χ_{c_1} and χ_{c_2} is presented. A reaction is proposed, where the resonant signal of these states could be observed through the interference with the radiative return background.

Streszczenie

W pracy tej zostały przedstawione wyniki teoretycznych obliczeń dla procesów anihilacji elektron-pozytron do hadronów+fotony. Został poruszony szeroki zakres tematów ze szczególnym uwzględnieniem obliczeń poprawek radiacyjnych i ich implementacji w generatorze Monte Carlo PHOKHARA. Ważną część tej pracy stanowi modelowanie oddziaływań hadronów z fotonami.

Przedstawione są istotne tematy z punktu widzenia niezgodności pomiędzy eksperymentalną, a przewidywaną w ramach Modelu Standardowego wartością anomalnego momentu magnetycznego mionu. Jednym z nich jest modelowanie dwufotonowych form faktorów dla mezonów pseudoskalarnych, które są istotne dla wyznaczenia wkładów od hadronowego rozpraszania światło-światło. Drugim jest obliczenie poprawek radiacyjnych wyższego rzędu dla przekroju czynnego na produkcję pary pionów, które stanowią istotny wkład do analizy danych wykonywanej w eksperymentach BABAR i KLOE, których pomiary nie zgadzają się pomiędzy sobą.

Kolejny rozważany w tej pracy temat jest związany z niezgodnościami jakie obserwuje się w przypadku pomiaru promienia protonu przy użyciu różnych metod eksperymentalnych. Modelowanie form faktorów nukleonowych jest pierwszym krokiem w celu obliczenia pełnych poprawek radiacyjnych dla procesu rozpraszania elektron-proton. Obliczenie wkładów od wymiany dwufotonowej dla tego procesu wymagają znajomości form faktorów opisujących przejścia pomiędzy różnymi stanami.

Ostatni temat porusza kwestię związane z produkcją stanów o dodatnich wartościach własnych operatorów sprzężenia ładunkowego i parzystości. Przedstawiony jest model na elektronowe szerokości połówkowe χ_{c_1} i χ_{c_2} oraz zaproponowana jest reakcja w której ich obserwacja byłaby możliwa poprzez interferencję z tłem pochodzącym od amplitud dla powrotu radiacyjnego.

Contents

Chapter 1

Introduction

During the last years enormous progress in our understanding of the fundamental interactions has been done. The systematic comparisons of the precise experimental data with the theory predictions give us a better constraints on the experimental observables and set a very strict limits for the new physics phenomena. Despite the big success of the Standard Model and the discovery of the Higgs boson [1] there are still a few observables, which measurements exhibits disagreements and could indicate that there is physics beyond the Standard Model. Moreover, the phenomena like dark matter, which are not described within the Standard Model, indicate that it is not a fundamental theory of nature. Precision tests of the Standard Model requires mutual work of the experimental collaborations and theory groups [2]. As the experimental measurements are performed with the higher and higher accuracy, testing the Standard Model, from the theory side, involves calculations and implementation of the higher order radiative corrections in the Monte Carlo event generators as well as the precise knowledge of the input parameters as masses and couplings.

One of the most important observable in particle physics is the hadronic cross section. Its value governs the running of the electromagnetic coupling constant at low energy up to the mass of Z^0 boson and it is therefore very important for precision analysis of the electroweak interaction. It constitutes the crucial input for determination of strong coupling constant, quark masses, Z^0 mass and its width and low energy quantities like pion or nucleon form factors. Furthermore the hadronic cross section is very important for a precise determination of the muon anomalous magnetic moment $(g-2)_\mu$. The quantity, where one observes the discrepancy between experimental data and the Standard Model predictions, which exceed 3σ [3,4]. The error of this discrepancy is dominated by the hadronic contributions [3,4], which cannot be calculated perturbatively with a desired precision. One of the crucial contribution

to the hadronic part comes from the hadronic vacuum polarization diagrams. This contribution can be calculated using dispersive integral approach, which relates the HVP contribution to the measured value of the $e^+e^- \to$ hadrons cross section. The second crucial contribution, the hadronic light-by-light (HLbL) is mainly calculated using effective models. Since the tensor structure of the (HLbL) contributions is quite complicated and there is not enough precise experimental data, only recently some progress in application of the dispersive integral approach to HLbL part of the $(g-2)_\mu$ has been done [5]. The dominant contribution to the HVP part and its uncertainty comes from the pion pair production cross section. Its precise determination is limited by the observed discrepancy between BABAR and KLOE measurements. As this discrepancy might have originated partly from the missing radiative corrections, including of the higher order effects in the data analysis may help to resolve this issue. For HLbL part the biggest contribution to its value and uncertainty comes from the exchange of the neutral pseudoscalar mesons. Its precise determination involve modeling of the pseudoscalar-two-photon transition form factors in the space-like region. Since the form factors in the space-like and the time-like regions are connected via analyticity, the transition form factors can be tested in the electron-positron collisions giving access to the production of different resonance states.

The low energy form factors for the nucleons play important role for resolving the proton radius puzzle [6]. The observed discrepancy between two different measurements using muonic hydrogen and electronic hydrogen can be resolved by the more precise measurements of the ratio of proton electric and magnetic form factors in the scattering $e^-p \to e^-p$. To obtain the high precision data including higher order radiative corrections is indispensable. As the knowledge of the proton transition form factors is necessary to calculate this corrections, the modeling of the nucleon form factors can constitute the first step in including complete radiative corrections to the reaction $e^-p \to e^-p$.

The production of the narrow resonances in electron-positron annihilation up to now has been observed experimentally only for states with negative charge and parity ($J^{CP} = J^{--}$). This states are produced by ordinary annihilation through one photon. The possibility to observe the resonances with even charge conjugation and parity ($J^{CP} = J^{++}$) are strongly suppressed. As these states have a different quantum numbers from photon, their production at the lowest order go through two photons or neutral current (only 1^{++}state). Since the production rate for J^{++} states is tiny the only possible way of observing this states is through the interference process. Small production rate can be compensated by the high luminosity. The observation of the resonant signal is within the range of the experiments as BES-III.

The layout of this thesis is the following. Chapter 2 presents the results for modeling the nucleon form factors and calculation of the final state radiative corrections to the proton-antiproton cross section. Chapter 3 describes modeling of the electronic widths of the χ_{c_1} and the χ_{c_2} and application of this results to the reaction $e^+e^- \to \chi_{c_{1,2}} \to \gamma J/\psi(\to \mu^+\mu^-)$. Chapter 3 presents the Lagrangian approach to the modeling the two-photon transition form factors for pseudoscalar mesons and analysis of the size of the radiative corrections in the pseudoscalar photon production cross section. In Chapter 5 the procedure for calculation of the next-to-leading order radiative corrections is presented and analysis of their size in the context of the BABAR and KLOE discrepancy is performed. In the Chapter 6 the final conclusions are presented. The thesis is based on the publications [7–13], with my coauthorship.

Chapter 2

Nucleon form factors and final state radiative corrections to the reaction $e^+e^- \longrightarrow p\bar{p}(\gamma)$

2.1 Motivation

The electromagnetic structure of the nucleons is described by the electric and magnetic form factors, which describe the distribution of the charge inside nucleus as a function of the transferred momentum Q^2. During the past years a lot of effort have been done to extract electric and magnetic form factors in electron-proton scattering experiments. Two methods were developed for this purpose. First of them is the Rosenbluth technique [14], which base on the formula of unpolarized differential cross section for elastic scattering.

$$\frac{d\sigma}{d\Omega} = \sigma_{Mott}\Big[\frac{G_E^2(Q^2) + \tau G_M^2(Q^2)}{1+\tau} + 2\tau G_M^2 \,\mathrm{tg}^2(\theta/2)\Big], \tag{2.1}$$

with

$$\sigma_{Mott} = \frac{\alpha^2 \cos^2(\theta/2)}{eE^2 \sin^4(\theta/2)} \frac{E'}{E}, \tag{2.2}$$

where, G_E and G_M are electric and magnetic form factors, $\tau = Q^2/4M_N^2$, M_N is nucleon mass, θ is electron scattering angle $Q^2 = (p'-p)^2 = 4EE' \sin^2(\theta/2)$, where p, p' and E, E' are incoming and scattered electron momenta and energies. One can define the reduced cross section

$$\sigma_R = \frac{d\sigma}{d\Omega}\frac{\epsilon(1+\tau)}{\sigma_{Mott}} = \tau G_M^2(Q^2) + \epsilon G_E^2(Q^2), \tag{2.3}$$

where $\epsilon^{-1} = 1 + 2(1+\tau)\,\mathrm{tg}^2(\theta/2)$. The G_E can be extracted from the slope of the reduced cross section and τG_M from the intercept of the σ_R with the ϵ axis.

The second method is the recoil polarization technique [15]. It is based on the fact that the polarized elastic electron-proton scattering is sensitive to different combinations of electric and magnetic form factors. The ratio of the form factors G_E/G_M is related to the components of the recoil polarization through [16]

$$\frac{G_E}{G_M} = -\frac{P_t}{P_l}\frac{(E+E')\,\mathrm{tg}(\theta/2)}{2M_N}, \tag{2.4}$$

where P_t and P_l are the longitudinal and the transverse components of the final proton polarization.

The electron-proton scattering experiments give information about the form factors in the space-like region, where one can separate the electric and magnetic form factors by analysis of the angular distribution of the scattered particles. On the other hand, a measurement of the cross section of the reaction $e^+e^- \to p\bar{p}$ gives access to a specific combination of the form factors in the time-like region, where the separation of electric and magnetic contributions can be done by analysis of the angular distributions. The measured values of the ratio of electric and magnetic form factors of the proton using the Rosenbluth separation exhibited large discrepancies [17] with the measurements using the recoil polarization technique. Theoretically, this inconsistency is now mainly understood in terms of two-photon exchange effects, which have a strong impact on the result of the Rosenbluth separation but affect a polarization technique only minimally. These two-photon effects were not taken into account in the first analyses. The impact of the two-photon exchange diagrams have been shown using two calculations, one in the partonic framework and the second using a single hadronic intermediate state [18–20]. Experimental verification of the size of the two-photon effects, which will help in better understanding of the nucleon form factors structure is necessary. Since the form factors in the space-like and the time-like region are connected by the analyticity, the measurement of the proton-antiproton cross section may give more important information about the nucleons structure.

The cross section for proton-antiproton production can be measured via the radiative return method. The BABAR collaboration, which measured that cross section using the radiative return method [21], argued that the final state emission was negligible. If one can obtain an independent data set with higher precision, the size of the final state corrections have to be re-examined.

This part of my thesis is based on the work presented in [7]. The modeling

of the nucleon form factors and the final state radiative corrections to the proton-antiproton pair production were also the subject of my master thesis, which results were partly shown in [22]. The model of the nucleon form factors presented here, which has an impact on the size of the final state radiative corrections is modified as compared to my master thesis. In addition the cross section $e^- p \to e^- p$ was considered.

The layout of this Chapter is the following. In Section 2.2 the general information about nucleon form factors is presented and the modeling of the new form factor model is described together with the procedure used to determine the model parameters [7]. Section 2.3 contains the information about final state radiative corrections to the reaction $e^+e^- \to p\bar{p}\gamma$ and describes new development in this subject. In Section 2.4 the impact of the final state radiative corrections on the $p\bar{p}\gamma$ cross section is investigated. Section 2.5 contains conclusions.

2.2 Nucleon form factors

The most general hadronic current of the nucleon-antinucleon interaction with a photon, which is conserved and preserves parity (P), charge conjugation (C) and time reversal (T) symmetries has the following form:

$$J^\mu = -ie\bar{v}(p_2)\Big[F_1^N(Q^2)\gamma^\mu - \frac{F_2^N(Q^2)}{4M_N}[\gamma^\mu, \not{Q}]\Big]u(p_1), \tag{2.5}$$

where $Q^2 = (p_1 + p_2)^2$, p_1, p_2 are the proton and antiproton momenta, F_1^N and F_2^N are Dirac and Pauli form factors for the nucleon N. The electric and magnetic form factors written in terms of Dirac and Pauli form factors have the following form:

$$G_E^N(Q^2) = F_1^N(Q^2) + \tau F_2^N(Q^2), \tag{2.6}$$
$$G_M^N(Q^2) = F_1^N(Q^2) + F_2^N(Q^2). \tag{2.7}$$
$$\tag{2.8}$$

At $Q^2 = 0$ the electric form factor is normalized to the electric charge, while the magnetic form factor is normalized to the magnetic moment of the nucleon:

$$G_E^p(0) = 1 \qquad G_M^p(0) = \mu_p, \tag{2.9}$$
$$G_E^n(0) = 0 \qquad G_M^n(0) = \mu_n. \tag{2.10}$$

2.2.1 The model

The parameterization of the nucleon form factors [7] based on the generalized vector meson dominance has been adopted. The Dirac and Pauli form factors are represented as combination of isoscalar and isovector contributions:

$$F^p_{1,2}(Q^2) = F^s_{1,2}(Q^2) + F^v_{1,2}(Q^2), \tag{2.11}$$
$$F^n_{1,2}(Q^2) = F^s_{1,2}(Q^2) - F^v_{1,2}(Q^2), \tag{2.12}$$

where $F^s_{1,2}$ and $F^v_{1,2}$ refer to isospin zero and isospin one contributions respectively. The following parameterization of the isoscalar and isovector parts has been used:

$$F^s_1(Q^2) = \frac{1}{2}\frac{\sum_{n=0}^{4} c^1_n BW_{\omega_n}(Q^2)}{\sum_{n=0}^{4} c^1_n}, \tag{2.13}$$

$$F^v_1(Q^2) = \frac{1}{2}\frac{\sum_{n=0}^{4} c^2_n BW_{\rho_n}(Q^2)}{\sum_{n=0}^{4} c^2_n}, \tag{2.14}$$

$$F^s_2(Q^2) = -\frac{1}{2}b\frac{\sum_{n=0}^{4} c^3_n BW_{\omega_n}(Q^2)}{\sum_{n=0}^{4} c^3_n}, \tag{2.15}$$

$$F^v_2(Q^2) = \frac{1}{2}a\frac{\sum_{n=0}^{4} c^4_n BW_{\rho_n}(Q^2)}{\sum_{n=0}^{4} c^4_n}, \tag{2.16}$$

where $c^i_0 = 1$ for $i = 1, 2, 3, 4$, $a = \mu_p - \mu_n - 1$ and $b = -\mu_p - \mu_n + 1$, where μ_p and μ_n are magnetic moments of proton and neutron. In the model of the form factors the Zweig rule is applied and thus the ϕ contributions are neglected. The Breit-Wigner function has the following form:

$$BW_i(Q^2) = \frac{m_i^2}{m_i^2 - Q^2 - im_i\Gamma_i\theta(Q^2)}, \tag{2.17}$$

where $\theta(Q^2)$ is a step function, which sets the meson width to zero for the space-like region. Similarly, the complex coupling constants c^j_i can be rewritten using real parameters in the following way $c^j_i = c^{jR}_i + ic^{jI}_i\theta(Q^2)$, which ensures that for the space-like region the imaginary parts do not contribute to the cross section. Above the proton-anti-proton production threshold the constant meson widths is used. The high energy asymptotic behavior of the form factors predicted by the perturbative chromodynamics is imposed [23]

$$F_1 \sim \frac{1}{(Q^2)^2}, \quad F_2 \sim \frac{1}{(Q^2)^3}. \tag{2.18}$$

This allows to limit the number of independent complex parameters to be determined by experimental data to six. The asymptotic behavior, Eqs. 2.18,

is enforced by choosing

$$c_4^1 = -\frac{1}{m_{\omega_4}^2}\sum_{n=0}^{3} m_{\omega_n}^2 c_n^1, \tag{2.19}$$

$$c_4^2 = -\frac{1}{m_{\rho_4}^2}\sum_{n=0}^{3} m_{\rho_n}^2 c_n^2, \tag{2.20}$$

$$c_3^3 = \frac{\sum_{n=0}^{2} m_{\omega_n} c_n^3 (m_{\omega_n}^2 - m_{\omega_4}^2 + i(m_{\omega_4}\Gamma_{\omega_4} - m_{\omega_n}\Gamma_{\omega_n}))}{m_{\omega_3}^2 (m_{\omega_4}^2 - m_{\omega_3}^2 + i(m_{\omega_3}\Gamma_{\omega_3} - m_{\omega_4}\Gamma_{\omega_4}))},$$

$$c_4^3 = -\frac{1}{m_{\omega_4}^2}\sum_{n=0}^{3} m_{\omega_n}^2 c_n^3, \tag{2.21}$$

$$c_3^4 = \frac{\sum_{n=0}^{2} m_{\rho_n} c_n^4 (m_{\rho_n}^2 - m_{\rho_4}^2 + i(m_{\rho_4}\Gamma_{\rho_4} - m_{\rho_n}\Gamma_{\rho_n}))}{m_{\rho_3}^2 (m_{\rho_4}^2 - m_{\rho_3}^2 + i(m_{\rho_3}\Gamma_{\rho_3} - m_{\rho_4}\Gamma_{\rho_4}))},$$

$$c_4^4 = -\frac{1}{m_{\rho_4}^2}\sum_{n=0}^{3} m_{\rho_n}^2 c_n^2. \tag{2.22}$$

$$\tag{2.23}$$

The masses and widths of the meson resonances and nucleons have been fixed according to [24] with the exception of $\rho_{3,4}$ and $\omega_{3,4}$ for which masses and widths have not been measured. For these states the model of masses and widths has been adopted from [25, 26]. The model postulates the following relation between masses of the resonances, $m_{\rho(\omega)_n}^2 = m_{\rho(\omega)_0}^2(1+2n)$, and a linear relation between the masses and the widths of given resonance $\Gamma_{\rho(\omega)_n} = \gamma_{\rho(\omega)} m_{\rho(\omega)_n}$. $\gamma_{\rho(\omega)}$ are derived from the lowest laying mesons. Using this model one obtains the following values for masses and widths, which were not measured:

$$m_{\rho_3} = 2.12\ GeV, \qquad \Gamma_{\rho_3} = 0.3\ GeV, \tag{2.24}$$

$$m_{\rho_4} = 2.32647\ GeV, \qquad \Gamma_{\rho_4} = 0.4473\ GeV, \tag{2.25}$$

$$m_{\omega_3} = 2.0707\ GeV, \qquad \Gamma_{\omega_3} = 1.03535\ GeV \tag{2.26}$$

$$m_{\omega_4} = 2.32647\ GeV, \qquad \Gamma_{\omega_4} = 0.4473\ GeV. \tag{2.27}$$

The remaining coupling constants of nucleon-antinucleon to vector mesons have been fitted to the experimental data.

2.2.2 Determination of the model parameters

The model parameters have been fitted to the ratio of the proton electric and magnetic form factors in the space-like [27–31] and the time-like region [21, 32], the ratio of the neutron electric and magnetic form factors in the

space-like region [33,34], and the cross sections for the reactions $e^+e^- \to N\bar{N}$ [21,35–41], $p\bar{p} \to e^+e^-$ [32,42–46] and $e^-p \to e^-p$ [47]. The formulae for the cross section used in the fit have the following forms:

$$\sigma_{e^+e^-\to N\bar{N}} = \frac{2\pi\alpha^2\beta}{3s}\left(2|G_M^N(Q^2)|^2 + \frac{|G_E^N(Q^2)|^2}{\tau}\right), \tag{2.28}$$

where $N = p$, n, $\bar{N} = \bar{p}$, $\bar{n}$ and $\beta = \sqrt{1 - \frac{4M_N^2}{Q^2}}$.

$$\frac{d\sigma_{p\bar{p}} \to e^+e^-}{d\cos\theta^*} = \frac{\pi\alpha^2}{2\beta s}\left(|G_M^p(Q^2)|^2(1+\cos^2\theta^*) + \frac{|G_E^p(Q^2)|^2}{\tau}\sin^2\theta^*\right), \tag{2.29}$$

where θ^* is the angle between electron and antiproton.

$$\frac{d\sigma_{e^-p\to e^-p}}{d\Omega} = \frac{\alpha^2\cos^2(\theta/2)}{4E^2\sin^4(\theta/2)}\frac{E'}{E}\left(\frac{G_E^2(Q^2) + \tau G_M^2(Q^2)}{1+\tau} + 2\tau G_M^2\,\mathrm{tg}^2(\theta/2)\right), \tag{2.30}$$

where E and E' are the initial and the final electron energies, and θ is the scattering angle of the electron.

For the $e^-p \to e^-p$ cross section only one data set [47] has been used, which covers the wide range of energies and angles. Furthermore the experimental value of this cross section contain non-negligible contribution coming from the two-photon exchange. The theoretical prediction for this contribution involves the knowledge of the proton transition form factors. This issue is not addressed in this thesis. To take into account the missing corrections and to allow the electron-proton scattering cross section data to accommodate well into the model, the errors have been enlarged to 10% of the cross section in the fitting procedure.

The fit to all experimental data leads to unacceptable results, $\chi^2 = 214$ for 177 data points and 20 parameters. The reason is that the data measured by the experiment PS170 for the $p\bar{p} \to e^+e^-$ cross section and the data collected by the DM2 experiment for the $e + e^- \to p\bar{p}$ cross section are in conflict with the measurements performed by BABAR experiment. The model fit very well, when one excludes PS170 and DM2 data ($\chi^2 = 124$ for 150 data points) or BABAR data ($\chi^2 = 107$ for 133 data points). In this thesis I will only refer to the first fit, where PS170 and DM2 data were not included. The table 2.1 contains the values of the χ^2 for particular experiments. The values of the fitted parameters are presented in the table 2.2.

Fig. 2.1a shows the comparison of the experimental data with the model fit results for the cross section of the reaction $e^+e^- \to p\bar{p}$ as a function of the scattering energy $\sqrt{s}$. Individual measurements are represented by points

Experiment	nep	χ^2	Experiment	nep	χ^2
BaBar cs [21]	38	30	BaBar r [21]	6	0.6
$PS170_1$ cs [32]	8	109	PS170 r [32]	5	16
$PS170_2$ cs [42]	4	4	$PS170_3$ cs [43]	4	52
E760 cs [44]	3	0.5	$E835_1$ cs [45]	5	1
$E835_2$ cs [46]	2	0.03	DM2 cs [35, 36]	7	26
BES cs [37]	8	10	CLEO cs [38]	1	0.4
FENICE cs [39]	5	5	DM1 cs [40]	4	0.7
JLab 05 r [27]	10	16	JLab 02 r [28]	4	1
JLab 01 r [29]	13	10	JLab 10 r [30]	3	6
MAMI 01 r [31]	3	2	JLab 03 r [33]	3	6
BLAST 08 r [34]	4	6	FENICE cs [39]	4	0.6
			SLAC cs [47]	32	27

Table 2.1: The chi-squared values for particular experiments; nep- number of experimental points; cs - cross section; r- ratio of the electric and magnetic form factors.

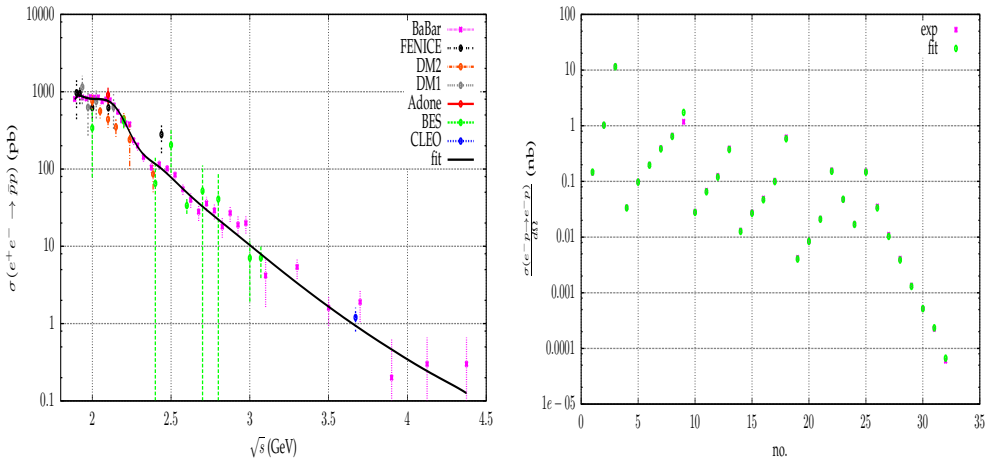

(a) (b)

Figure 2.1: The experimental data compared to the model fit results. (a) Cross section of the reaction $e^+e^- \to p\bar{p}$, (b) Cross section of the reaction $e^-p \to e^-p$.

with error bars, while the solid black line represents the results obtained from the fit. One can observe that all data fitted very well and that this model

c_1^{1R}	-0.45(1)	c_1^{1I}	-0.54(2)	c_2^{1R}	-0.27(1)	c_2^{1I}	0.18(1)
c_3^{1R}	0.42(2)	c_3^{1I}	0.37(2)	c_1^{2R}	-0.12(1)	c_1^{2I}	-3.06(2)
c_2^{2R}	0.16(1)	c_2^{2I}	2.53(1)	c_3^{2R}	-0.32(1)	c_3^{2I}	-0.17(1)
c_1^{3R}	-8.03(5)	c_1^{3I}	3.28(2)	c_2^{3R}	10.6(1)	c_2^{3I}	0.2(3)
c_1^{4R}	-0.845(1)	c_1^{4I}	0.364(1)	c_2^{4R}	0.427(1)	c_2^{4I}	-0.305(1)

Table 2.2: Parameters of the nucleons form factor obtain from the fit to experimental data. The errors, given in brackets are the parabolic errors calculated by procedure Minos of the MINUIT package [48].

cannot accommodate simultaneously BABAR and DM2 data sets. Fig. 2.1b shows the comparison of the experimental data with the model fit results for the cross section of the reaction $e^- p \to e^- p$, where on the horizontal axis the entry number is presented, which corresponds to the order of experimental points in Table III from [47]. Each experimental point was obtained for different scattering energy and it corresponds to different scattering angle and the value of the transferred momentum. In that case almost all experimental points (pink) are well described by theoretical model (green points). The exception is only one point (9th), where one can observe small shift from the measurement. On the plots from Fig. 2.2 the comparison of the experimental data with the model fit results for the cross section of the reaction $p\bar{p} \to e^+ e^-$ as a function of a square of beam energy s is presented. Individual measurements are represented by points with error bars, while the fitted model predictions are represented by black points. On this plots each point represents the cross section integrated in different range of polar angles. The plot 2.2a shows this comparison for the experiments E760 and E835, which were included in the fit. In that case all data fitted very well. The comparison of the theoretical model with the PS170 measurement, which was not included in the fit is shown on the plot from Fig. 2.2b. Here one can observe a big discrepancy between experimental points and model predictions, which is caused by the fact that these data are in contradiction with the BABAR measurement of the ratio of the proton electric and magnetic form factors in the time-like region. The plots from Fig. 2.3 show the ratio of the electric and magnetic form factors in the space-like (Fig.2.3a) an the time-like (Fig.2.3b) regions. In both cases the individual measurements are represented by points with error bars, while the solid black line represents the results obtained from the fit. For the space-like region all data are well described by the model, while for the time-like region one can observe that there is no possibility to fit BABAR and PS170 data simultaneously. The plots from Fig. 2.4 show

the comparison of the experimental data with the model fit results for the neutron-antineutron production cross section (Fig.2.4a) and ratio of the electric and magnetic neutron form factors in the space-like region (Fig.2.4b). On both plots, individual measurements are represented by points with error bars, while solid black line represents the results obtained from the fit. The neutron data are well described by the fitted model but one can notice that the current measurements do not give a strict constraints on the model parameters, in particular in the case of neutron-antineutron production cross section.

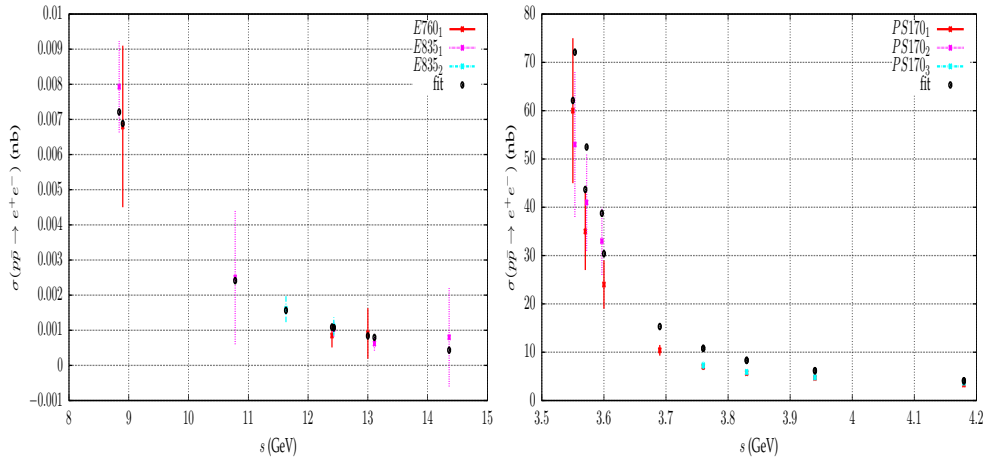

(a) (b)

Figure 2.2: The experimental data compared to the model fit results. Cross section of the reaction $p\bar{p} \to e^+e^-$.

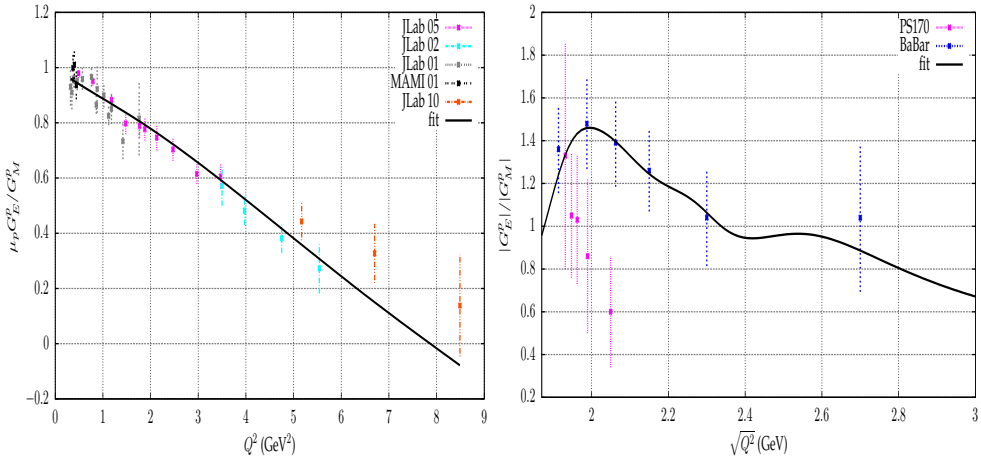

(a) (b)

Figure 2.3: The experimental data compared to the model fit results. Ratio of the electric and magnetic proton form factors in space-like (a) and time-like (b) regions.

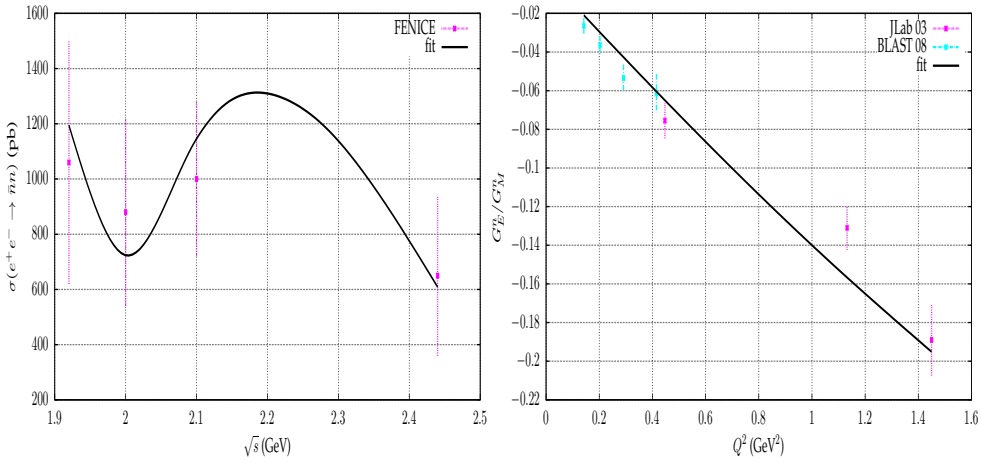

(a) (b)

Figure 2.4: The experimental data compared to the model fit results. Neutron-antineutron production cross section (a) and ratio of the electric and magnetic neutron form factors in space-like region (b).

2.3 Final state radiative corrections

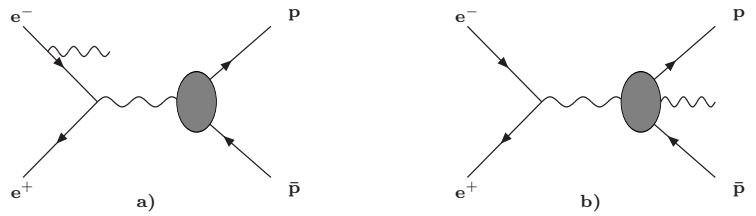

Figure 2.5: Representative diagrams for leading order amplitudes for the reaction $e^+e^- \to p\bar{p}\gamma$.

At the leading-order (LO) the amplitude for the reaction $e^+e^- \to p\bar{p}\gamma$ can be written in the following form:

$$\mathcal{M}_{LO} = \mathcal{M}_{1ISR} + \mathcal{M}_{1FSR}, \tag{2.31}$$

where $\mathcal{M}_{1ISR}$ is the amplitude with the emission of one photon from the initial state, presented in Fig. 2.5a, and $\mathcal{M}_{1FSR}$ is the amplitude with the emission of one photon from the final state, presented in Fig. 2.5b. The sum of this two contributions constitutes the Born amplitude for the radiative return process.

At the next-to-leading order (NLO) the amplitude consist of the contribution with two hard photons, virtual corrections and soft photon radiation. The amplitude for 2 hard photon emission can be written in the following form:

$$\mathcal{M}_{2\gamma} = \mathcal{M}_{2ISR} + \mathcal{M}_{2FSR} + \mathcal{M}_{1ISR,1FSR}, \tag{2.32}$$

where the individual contributions are represented by diagrams from Fig. 2.6. The virtual corrections are represented by the diagrams from Fig. 2.4 and soft photon contributions can be obtained from diagrams from Fig. 2.6 by imposing a condition that one of the photons have energy $E_\gamma < E_{\gamma,min}$. The virtual corrections at the NLO contribute only through the interference with the Born amplitude.

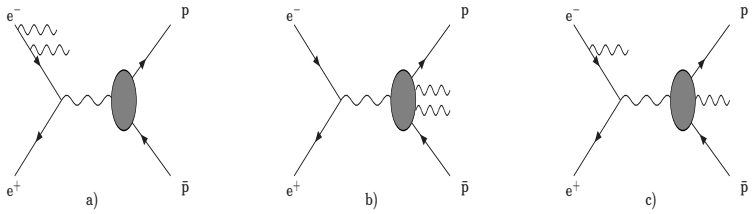

Figure 2.6: The next-to-leading order amplitudes with photons emissions for the reaction $e^+e^- \to p\bar{p}\gamma$ (permutations are omitted).

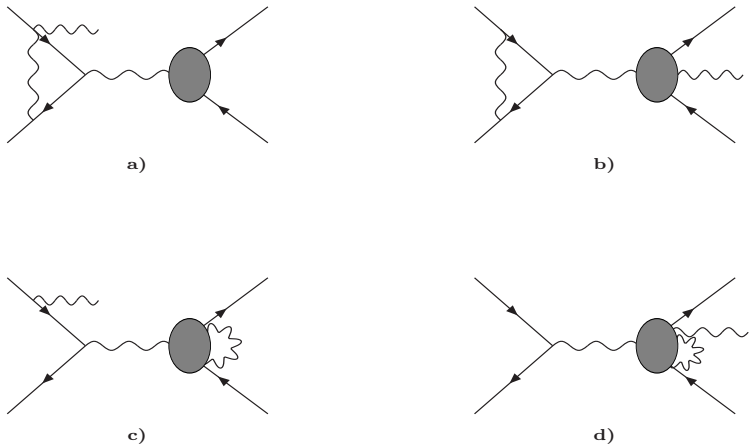

Figure 2.7: Representative classes of diagrams for virtual corrections at the NLO.

2.3.1 The implementation of the FSR corrections

The previous [49] version of the PHOKHARA (PHOKHARA 7.0) Monte Carlo event generator allows to simulate the reaction of $e^+e^- \to p\bar{p}\gamma$ at the next-to-leading order, where only the initial state radiative corrections were included. The amplitudes included in that version of the code are the emission of one photon from the initial state presented in Fig. 2.5a, emission of two photons from the initial state presented in Fig. 2.6a, and the virtual+soft corrections to the initial state represented by the diagram from Fig. 2.7a. The calculation of the ISR, even if it is not simple, is the straightforward application of the Feynman rules of the Quantum Electrodynamics (QED). The situation is more complicated, when one has to deal with the final state corrections, where a composite object as proton radiates photons. The real radiation from the proton (antiproton) in the simplest model can be treated

with a good approximation as the emission from the point-like objects. This was adopted in [7], where the proton form factors enter only the vertex with the coupling of the virtual photon to proton-antiproton pair. For the virtual final state corrections one cannot adapt the point-like corrections from the muon case [50]. Since an additional term in the hadronic current, proportional to the Pauli form factor, is present, the corrections are not the same. There is also no reason for the corrections proportional to F_1 and F_2 to be the same. Moreover, the model described by the interaction Lagrangian, which produces the hadronic current given in the Eq. 2.5 is non-renormalizable even for constant form factors, in case F_2 is present. To overcome these difficulties a general strategy to include only the corrections, which should appear in any model, was adopted. This is done by including the modified Coulomb factor in the following form:

$$C(Q^2) = f(\pi\alpha/\beta) - f(\pi\alpha) + 1, \tag{2.33}$$

where

$$f(x) = \frac{x}{1-\exp(-x)}, \qquad \beta = \sqrt{1-\frac{4m_p^2}{Q^2}}, \tag{2.34}$$

where Q^2 is invariant mass of the proton-antiproton pair. The $C(Q^2)$ at small proton velocities reproduces resummation of the leading radiative corrections and for $Q^2 \to \infty$ goes to one. The above Coulomb factor multiply zero, one and two photon emission parts. In a Coulomb factor C_F

$$C_F(Q^2) = f(\pi\alpha/\beta). \tag{2.35}$$

Second universal correction comes from soft virtual+real emission and reads:

$$\Delta_{FSR} = \frac{2\alpha}{\pi}\left[\frac{1+\beta^2}{2\beta}\log\frac{Q^2(1+\beta^2)}{4m_p^2} - 1\right]\log 2w, \tag{2.36}$$

where $w = E_{\gamma,min}/\sqrt{s}$ is a separation parameter between the soft and the hard part of the photon phase space. Including the Δ_{FSR} is indispensable to cancel the infrared divergences, which come from the integration of the photon emission with energy $E_\gamma > E_{\gamma,min}$. The form of this correction ensures also the independence of the total cross section on the separation parameter w. The virtual correction to the initial state have the following form [51]:

$$\Delta_{ISR} = \frac{2\alpha}{\pi}\left[\left(\log\left(\frac{s}{m_e^2}\right) - 1\right)\log 2w + \frac{3}{4}\log\left(\frac{s}{m_e^2}\right) - 1 + \pi^2\right]. \tag{2.37}$$

Interferences of virtual corrections with LO amplitudes, which are included in the current version of the PHOKHARA Monte Carlo generator for

the reaction $e^+e^- \to p\bar{p}\gamma$ [7], are presented in Fig. 2.8. The newly added part consist of the interference of the initial state virtual corrections with the LO FSR (Fig. 2.7b) and the interference of the final state virtual corrections with the LO ISR (Fig. 2.7c). The charge-odd combinations of the amplitudes, which could lead to the asymmetries have not been included in this work. For the photon radiation, the amplitudes included in the current version of the code contain full LO FSR with the ISR$\times$ FSR interference and NLO diagrams with emission of one photon from the initial state and one photon from the final state (Fig. 2.6c). The size of the contributions from the diagrams with the emission of two photons from the final state is expected to be negligible. For muons the corrections were calculated in [52] and the results show that they are at the per mille level. The effect of a similar size, or smaller, should be observed for the $p\bar{p}\gamma$ cross section.

To calculate the amplitudes for the real radiation from the final states, the helicity amplitude formalism developed in [53, 54] has been used, where the Dirac γ matrices are used in the Weyl representation. The calculation of the LO and NLO amplitudes is described in the Appendix A.

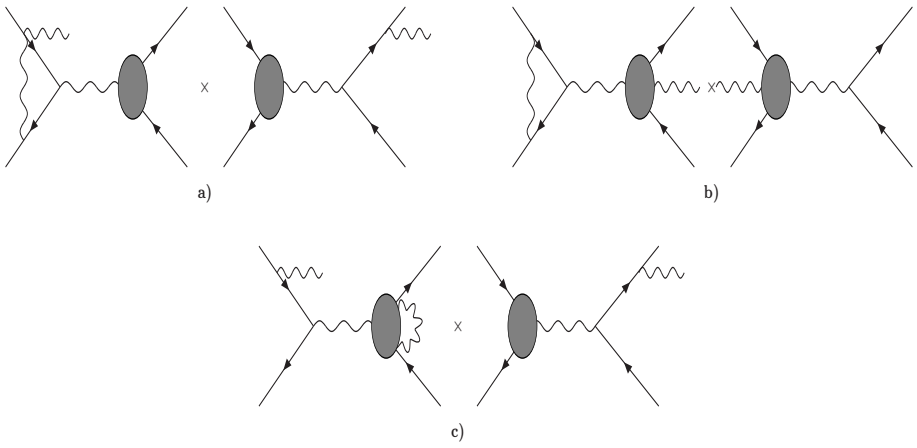

Figure 2.8: Interferences of virtual corrections with LO amplitudes, which were taken into account at NLO.

2.4 Monte Carlo simulations

The plot from Fig. 2.9a shows the relative difference between the ISR and the FSR cross section at the NLO. The plot from Fig. 2.9b shows the relative difference between cross section with complete FSR corrections and the cross section with FSR corrections, where only Coulomb factor C_F is included.

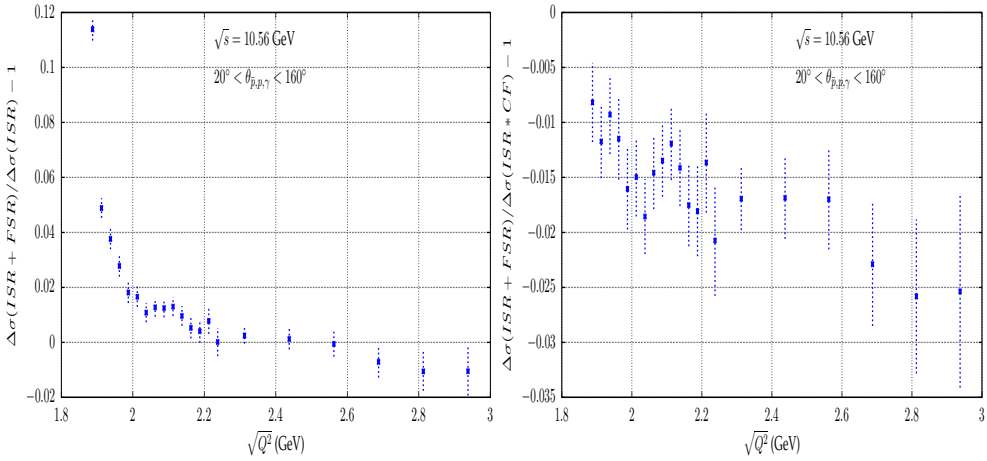

(a) (b)

Figure 2.9: Relative difference between Q^2 distributions calculated at NLO with and without FSR radiative corrections (a) and between the implemented FSR corrections and FSR corrections, where only Coulomb factor is included (b).

The event selection has been chosen to be close to the one used by BABAR. As one can observe the dominant contribution of the FSR comes from the Coulomb factor and can achieve up to 12% in the region close to the threshold for production of proton-antiproton pair. The typical size of the remaining FSR corrections beyond the Coulomb factor is of the order of 1%. The same differences for the event selection close to the one used by BES are presented on the plots from Fig. 2.10. The influence of the Coulomb factor is even bigger than in the case of the BABAR and its size can achieve up to 16% for low proton-antiproton invariant masses. The size of the FSR corrections, which are not included in the Coulomb factor are up to 1%.

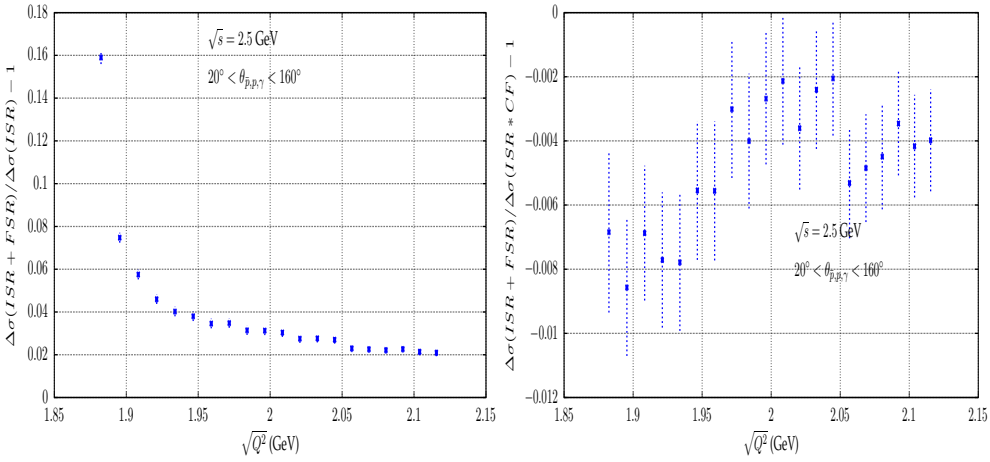

(a) (b)

Figure 2.10: Relative difference between Q^2 distributions calculated at NLO with and without FSR radiative corrections (a) and between the implemented FSR corrections and FSR corrections where only Coulomb factor is included (b).

2.5 Conclusions

The model of the nucleon form factors, developed in [7], quite well describes most of the experimental data. Yet there is still room for improvements. Since the PS170 and DM2 data are in conflict with the BABAR data it is quite unlikely that any model can accommodate all of them at the same time. In the light of this discrepancy it will be highly desirable to confirm BABAR data by an independent measurement with a similar precision.

The effect of the final state radiative corrections on the proton-antiproton cross section, except the Coulomb factor is small for typical experimental cuts and it is of the order of 1%. The measurable difference between ISR NLO cross section and the cross section with the final state radiative corrections comes from the Coulomb factor, which is big close to the threshold for production of proton-antiproton pair.

Chapter 3

Production of states with even charge conjugation in electron - positron annihilation

3.1 Motivation

The formation of resonances with even charge conjugation ($C = +1$) in electron-positron annihilation have not been observed so far. The production of these states is only possible through the neutral current ($J^{CP} = 1^{++}$) or through higher order electromagnetic reaction ($J^{CP} = 1^{++}$ and $J^{CP} = 2^{++}$). Both possibilities are strongly suppressed comparing to the ordinary annihilation through one photon ($J^{CP} = 1^{--}$ state). The production of these states through these mechanisms for charmonium resonances (χ_{c_J} for $J = 1, 2$) in the frame of non-relativistic quarkonium model has been suggested long time ago in [55, 56]. Because of the small resonant enhancement of the cross section for production of these states there were no attempts to verify the predictions. Now the situation has changed and the observation of these resonances seems to be possible in experiment like BES-III. The proposed reaction to observe the resonant signal is $e^+e^- \to \chi_{c_J} \to \gamma J/\psi$, with the subsequent decay of J/ψ into pair of muons [8,9]. In the case of this reaction an important role plays the interference with the non-reducible background, which comes from the radiative return reaction $e^+e^- \to \gamma J/\psi(\to \mu^+\mu^-)$. This gives rise to the interesting interference pattern and makes possible the observation of χ_{c_i} states through the interference with the background. The proposed reaction could serve as a tool for a determination of the electronic widths of $\chi_{c_{1,2}}$ states, which due to their smallness, have not been measured yet.

The layout of this Chapter is the following. In Section 3.2 the calculations of the amplitudes for a coupling of $\chi_{c_{1,2}}$ states to two photons and a neutral current is presented. In Section 3.3 it was demonstrated that the model for calculation of electronic widths in terms of the short distance approximation presented in [56] has to be extended to include at least binding energy corrections. In that Section the model for electronic widths, which combine short and long distance results was also presented. Section 3.4 contains the amplitudes for the reaction $e^+e^- \to \gamma J/\psi(\to \mu^+\mu^-)$, which can be used to extract electronic widths of $\chi_{c_{1,2}}$. The results for the cross section of this reaction obtained using the Monte Carlo simulations are presented in Section 3.5. Section 3.6 contains conclusions.

3.2 Amplitudes for couplings χ_{c_J} states to two photons and to the neutral current

The amplitude describing the annihilation of free fermion and antifermion into two photons can be written in the following way [56]:

$$\mathcal{A}_f = \bar{v}(\bar{f},\bar{s})\mathcal{O}u(f,s), \tag{3.1}$$

where f, $\bar{f}$ and s, $\bar{s}$ are momenta and spins of a fermion and an antifermion. The operator $\mathcal{O}$ a LO has the following form:

$$\mathcal{O} = \frac{1}{i}\Big[(-ie\not{\epsilon}_2)\frac{i}{\not{f}-\not{p}_1-m}(-ie\not{\epsilon}_1) + (-ie\not{\epsilon}_1)\frac{i}{\not{f}-\not{p}_2-m}(-ie\not{\epsilon}_2)\Big], \tag{3.2}$$

where p_1, p_2, ϵ_1, ϵ_2 are momenta and polarization vectors of photons and m is the fermion (antifermion) mass. In the non-relativistic approximation, the amplitude for fermion and antifermion in a bound state is given by a linear superposition of the amplitudes for free particles weighted by the bound state wavefunction $\psi_{s\bar{s}}(\mathbf{k})$. In the bound state rest frame the amplitude reads [56]:

$$\mathcal{A} = \sqrt{\frac{1}{m}}\int \frac{d\mathbf{k}}{(2\pi)^{3/2}}\psi_{s\bar{s}}(\mathbf{k})\bar{v}(\bar{f},\bar{s})\mathcal{O}u(f,s), \tag{3.3}$$

where the following relations hold:

$$f-\bar{f} = 2k = (0,2\mathbf{k}), \tag{3.4}$$

$$f+\bar{f} = P = (M,0), \tag{3.5}$$

$$\sum_{s\bar{s}}\int d\mathbf{k}|\psi_{s\bar{s}}(\mathbf{k})|^2 = 1. \tag{3.6}$$

M is the bound state mass. Converting the matrix element $\bar{v}(\bar{f},\bar{s})\mathcal{O}u(f,s)$ into a trace of γ matrices and considering the singlet and triplet states, one gets [56]:

$$\sum_{s\bar{s}} \quad \bar{v}(\bar{f},\bar{s})\mathcal{O}u(f,s)\,\langle\frac{1}{2},s;\frac{1}{2},\bar{s}|S,S_z\rangle = \frac{1}{\sqrt{E_{\bar{f}}+m}}\frac{1}{\sqrt{E_f+m}}Tr\Big[(m-\bar{f})\mathcal{O}(m+f)\frac{1+\gamma_0}{2\sqrt{2}}\Pi_{SS_Z}\Big], \quad (3.7)$$

with $\Pi_{00} = -\gamma_5$ and $\Pi_{1,S_Z} = -\not{\epsilon}^{(S_z)}$, where $\epsilon^{(S_z)}$ is the spin part of the wavefunction. Expanding Eq. 3.7 up to terms linear in k one gets:

$$\frac{1}{\sqrt{E_{\bar{f}}+m}}\frac{1}{\sqrt{E_f+m}}Tr\Big[(m-\bar{f})\mathcal{O}(m+f)\frac{1+\gamma_0}{2\sqrt{2}}\Pi_{SS_Z}\Big] = Tr\Big[\Big((M+\frac{1}{2}b)\mathcal{O}_0+\{\mathcal{O}_0,\not{k}\}+(M+\frac{1}{2}b)\mathbf{k}\cdot\mathcal{O}\Big)\frac{1+\gamma_0}{2\sqrt{2}}\Pi_{SS_Z}\Big], \quad (3.8)$$

where $b = 2m - M$ is a binding energy and:

$$\begin{aligned}\mathcal{O}_0 &\equiv \mathcal{O}|_{k=0} \\ &= \frac{-e^2}{[\frac{1}{2}(p_1-p_2)]^2-m^2+i\epsilon}[\not{\epsilon}_2\not{\epsilon}_1\not{p}_1 - \not{p}_1\not{\epsilon}_1\not{\epsilon}_2], \quad (3.9)\\ \mathcal{O}_\mu &\equiv \frac{\partial}{\partial k^\mu}\mathcal{O}|_{k=0} \\ &= \frac{-e^2}{[\frac{1}{2}(p_1-p_2)]^2-m^2+i\epsilon}[p_1\cdot p_2\epsilon_{1_\mu}\not{\epsilon}_2 - p_{1_\mu}\epsilon_1\cdot\epsilon_2\not{p}_1 + \not{\epsilon}_2\epsilon\cdot p_2 \\ &\quad -\not{\epsilon}_1 p_1\cdot\epsilon_2]. \quad (3.10)\end{aligned}$$

The terms proportional to the binding energy in Eq. 3.8 break the gauge invariance and thus should not be taken into account. For P-waves, which describe χ_{c_J} states, only terms linear in k contribute. From the orbital part one gets:

$$\sqrt{\frac{1}{m}}\int\frac{d\mathbf{k}}{(2\pi)^{3/2}}k_\mu\psi_{s\bar{s}}(\mathbf{k}) = -a\epsilon_\mu^{(m)}, \quad (3.11)$$

with $a \equiv \sqrt{\frac{1}{m}}\sqrt{\frac{3}{4\pi}}\phi'(0)$, where $\phi'(0)$ is the derivative of the radial wavefunction at the origin and $\epsilon_\mu^{(m)}$ is the orbital part of the wavefunction. Collecting all these results together one obtains the following expression for the ampli-

tude for annihilation of ${}^3P_J$ states into two photons:

$$A^{^3P_J} = \frac{a}{2\sqrt{2}} Tr\Big[\not\epsilon^{(S_Z)}\epsilon_\mu^{(m)}\mathcal{O}^\mu(M+\not P) + 2\mathcal{O}_0\epsilon_\mu^{(m)}\epsilon^{\mu^{(S_Z)}} + \mathcal{O}_0\frac{\not P}{M}\{\not\epsilon^{(S_Z)},\not\epsilon^{(m)}\}$$
$$\langle 1,1,S_Z,m|J,J_Z\rangle\Big]. \tag{3.12}$$

The following relations hold [56]:

$$\begin{aligned}
\epsilon_\mu^{(S_Z)}\epsilon_\nu^{(m)}\,\langle 1,1,S_Z,m|0,0\rangle &= \sqrt{\frac{1}{3}}\Big(g_{\mu\nu}-\frac{P_\mu P_\nu}{M^2}\Big),\\
\epsilon_\mu^{(S_Z)}\epsilon_\nu^{(m)}\,\langle 1,1,S_Z,m|1,0\rangle &= -\frac{i}{\sqrt{2}M}\epsilon_{\alpha\beta\mu\nu}P^\alpha\epsilon^\beta,\\
\epsilon_\mu^{(S_Z)}\epsilon_\nu^{(m)}\,\langle 1,1,S_Z,m|2,0\rangle &= \epsilon_{\mu\nu},
\end{aligned} \tag{3.13}$$

where ϵ^μ and $\epsilon^{\mu\nu}$ are polarization vector and tensor of the bound states. Inserting relations 3.13 into formula 3.12 one obtains the amplitudes for coupling of two virtual photons to χ_{c_J} states:

$$A_0^{\alpha\beta}(p_1,p_2)\epsilon_\alpha^1\epsilon_\beta^2 = \sqrt{\frac{1}{6}}c\frac{2}{M_{\chi_{c_0}}}\{[(\epsilon_1\epsilon_2)(p_1p_2)-(\epsilon_1p_2)(\epsilon_2p_1)][M_{\chi_{c_0}}^2+(p_1p_2)]$$
$$+(\epsilon_1p_2)(\epsilon_2p_2)p_1^2+(\epsilon_1p_1)(\epsilon_2p_1)p_2^2-(\epsilon_1\epsilon_2)p_1^2p_2^2-(\epsilon_1p_1)(\epsilon_2p_2)p_1p_2\}, \tag{3.14}$$

$$\begin{aligned}
A_1^{\alpha\beta}(p_1,p_2,\epsilon)\epsilon_\alpha^1\epsilon_\beta^2 &= ic\{p_1^2(\epsilon,\epsilon_1,\epsilon_2,p_2)+p_2^2(\epsilon,\epsilon_2,\epsilon_1,p_1)\\
&\quad +\epsilon_1p_1(\epsilon,\epsilon_2,p_1,p_2)+\epsilon_2p_2(\epsilon,\epsilon_1,p_2,p_1)\},
\end{aligned} \tag{3.15}$$

$$\begin{aligned}
A_2^{\alpha\beta}(p_1,p_2,\epsilon)\epsilon_\alpha^1\epsilon_\beta^2 &= \sqrt{2}cM_{\chi_{c_2}}\{(p_1p_2)\epsilon_\mu^1\epsilon_\nu^2+p_{1\mu}p_{2\nu}(\epsilon_1\epsilon_2)\\
&\quad - p_{1\mu}\epsilon_\nu^2(\epsilon_1p_2))-p_{2\mu}\epsilon_\nu^1(\epsilon_2p_1))\}\epsilon^{\mu\nu},
\end{aligned} \tag{3.16}$$

where

$$\begin{aligned}
c &\equiv c((p_1+p_2)^2,p_1^2,p_2^2,m)\\
&= \frac{16\pi\alpha a}{\sqrt{m}}\frac{1}{((p_1-p_2)^2/4-m^2+i\epsilon)^2},
\end{aligned} \tag{3.17}$$

From a number of independent Lorentz structures, which describe the interaction of χ_{c_i} states with two photons [56,57], only part of them contribute in this specific model. For χ_{c_0}, there are two independent amplitudes but only one of them contributes, for χ_{c_1} there are 3 independent amplitudes and only one amplitude contributes and for χ_{c_2} from five allowed amplitudes only one enters the model described in this Section.

For a coupling of the fermion-antifermion pair to the neutral current the operator $\mathcal{O}$ has the following form:

$$\mathcal{O} = \frac{-ig}{2\cos\theta_W} \not{\varepsilon}_{Z^0}(g_V + g_A\gamma_5), \tag{3.18}$$

where ε_{Z^0} is a polarization vector of the Z^0 boson, g is the electroweak coupling constant, θ_W is the weak mixing angle and $g_V = t_3 - 2Q\sin^2(\theta_W)$, $g_A = -t_3$ are axial and vector coupling constants, where t_3 and Q are third component of isospin and the charge of given fermion. For charm quark $t_3 = \frac{1}{2}$ and $Q = \frac{2}{3}$. Inserting the operator $\mathcal{O}$ into the formula from Eq. 3.3 with the use of equation 3.7 for a state with $S = 1$ and $S_z = 0$ and conserving only terms proportional to k one gets the amplitude for coupling of the χ_{c_1} to the neutral current. After performing trace and making use of the relation 3.13 one gets the following expression:

$$A_{(\chi_{c_1}-Z^0)} = \frac{2agg_AM^2_{\chi_{c_1}}}{\sqrt{2}(M_{\chi_{c_1}}/2+m)\cos\theta_W}\varepsilon^{\mu}_{Z^0}\varepsilon_{\chi_{c_1}\mu}\left(1+2\frac{m}{M_{\chi_{c_1}}}\right), \tag{3.19}$$

where $\varepsilon_{\chi_{c_1}\mu}$ is the polarization vector of χ_{c_1} and $M_{\chi_{c_1}}$ is its mass. As one can observe only the axial part of neutral current contribute to the amplitude describing the coupling of $\chi_{c_1} - Z^0$. The amplitude for coupling of χ_{c_2} states to Z^0 boson is zero due to the conservation of angular momentum.

3.3 Electronic widths of χ_{c_1} and χ_{c_2}

3.3.1 Short distance approximation and binding energy corrections

The contribution to the decay of the χ_{c_J} into e^+e^- pair in the short distance approximation, where couplings of χ_{c_i} to other charmonium states are neglected, is depicted in the diagram from Fig. 3.1. The amplitude can be

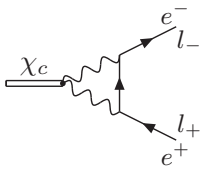

Figure 3.1: Diagram for decay widths $\Gamma(\chi_{c_{0,1,2}} \to e^+e^-)$ in short distance approximation.

written in the following form:

$$A(\chi_{cJ} \to e^+e^-) = ie^2 \int \frac{dp_1}{(2\pi)^4} \bar{v}(l_+)\gamma_\nu \not{h}\gamma_\mu u(l_-) \frac{1}{h^2}\frac{1}{p_1^2}\frac{1}{p_2^2} A_J^{\mu\nu}(p_1, p_2, \epsilon), \tag{3.20}$$

where $h = l_- - p_1$, $l_\pm$ is the momentum of electron (positron) and $A_J^{\mu\nu}$ is the amplitude, which describes the coupling of the χ_{cJ} state to two photons. Inserting Eqs. 3.14, 3.15 and 3.16 into formula from Eq. 3.20 and neglecting the electron mass the following expressions are obtained:

$$A(\chi_{c_0} \to e^+e^-) = 0, \tag{3.21}$$

$$A(\chi_{c_1} \to e^+e^-) = -2ie^2\bar{v}(l_+)\gamma_5\Big\{\int \frac{d^4p_1}{(2\pi)^4}\frac{c}{h^2p_1^2p_2^2}\Big(\not{\epsilon}[p_1^2p_2^2 + \frac{1}{2}h^2(p_1^2+p_2^2)] - \epsilon\cdot h\not{h}(p_1^2+p_2^2)\Big)\Big\}u(l_-), \tag{3.22}$$

$$A(\chi_{c_2} \to e^+e^-) = -ie^2\sqrt{2}M\bar{v}(l_+)\epsilon^{\mu\nu}\int \frac{d^4p_1}{(2\pi)^4}\frac{c}{h^2p_1^2p_2^2}\Big\{(l_+ - l_-)_\mu\gamma_\nu h^2 + 2\not{h}h_\mu h_\nu\Big\}u(l_-). \tag{3.23}$$

Here and in the following calculations $M = M_{\chi_{c_1}}$ for loop integrals involved in calculation of the amplitude $A(\chi_{c_1} \to e^+e^-)$ and $M = M_{\chi_{c_2}}$ for loop integrals involved in calculation of the amplitude $A(\chi_{c_2} \to e^+e^-)$.

Changing the integration variable from $p_1 \to h$ and inserting the expres-

sion from Eq. 3.17 for the function c one obtains:

$$A(\chi_{c_1} \to e^+e^-) = \frac{-32ie^2\pi\alpha a}{\sqrt{m}}\bar{v}(l_+)\gamma_5\Big\{\int\frac{d^4h}{(2\pi)^4}\frac{1}{h^2p_1^2p_2^2[(h-l_l)^2-m^2]^2}$$
$$\Big(\not{\epsilon}[p_1^2p_2^2+\frac{1}{2}h^2(p_1^2+p_2^2)]-\epsilon\cdot h\not{h}(p_1^2+p_2^2)\Big)\Big\}u(l_-), \quad (3.24)$$

$$A(\chi_{c_2} \to e^+e^-) = \frac{-16ie^2\pi\alpha a\sqrt{2}M}{\sqrt{m}}\bar{v}(l_+)\epsilon^{\mu\nu}\int\frac{d^4h}{(2\pi)^4} \quad (3.25)$$
$$\frac{1}{h^2p_1^2p_2^2[(h-l_l)^2-m^2]^2}\Big\{(l_+-l_-)_\mu\gamma_\nu h^2+2\not{h}h_\mu h_\nu\Big\}u(l_-),$$

where $l_l=\frac{l_--l_+}{2}$, $p_1=l_--h$ and $p_2=l_++h$. The amplitudes $A(\chi_{c_i}\to e^+e^-)$, $i=1,\,2$ can be written in the following way:

$$A(\chi_{c_1} \to e^+e^-) = \frac{-32ie^2\pi\alpha a}{\sqrt{m}}\bar{v}(l_+)\gamma_5\Big(\not{\epsilon}I_1+\frac{1}{2}I_2-\epsilon_\mu\gamma_\nu I_3^{\mu\nu}\Big)u(l_-), \quad (3.26)$$

$$A(\chi_{c_2} \to e^+e^-) = \frac{-16ie^2\pi\alpha a\sqrt{2}M}{\sqrt{m}}\bar{v}(l_+)\epsilon^{\mu\nu}\Big((l_+-l_-)_\mu\gamma_\nu I_4+2\gamma_\alpha I_{5\mu\nu}^{\alpha}\Big). \quad (3.27)$$

The following notation for the loop integrals is adopted:

$$I_1 = \int d^4h\frac{1}{h^2[(h-l_l)^2-m^2]^2}, \quad (3.28)$$

$$I_2 = \int d^4h\frac{p_1^2+p_2^2}{p_1^2p_2^2[(h-l_l)^2-m^2]^2}, \quad (3.29)$$

$$I_3^{\mu\nu} = \int d^4h\frac{h^\mu h^\nu(p_1^2+p_2^2)}{h^2p_1^2p_2^2[(h-l_l)^2-m^2]^2}, \quad (3.30)$$

$$I_4 = \int d^4h\frac{1}{p_1^2p_2^2[(h-l_l)^2-m^2]^2}, \quad (3.31)$$

$$I_5^{\mu\nu\alpha} = \int d^4h\frac{h^\mu h^\nu h^\alpha}{h^2p_1^2p_2^2[(h-l_l)^2-m^2]^2}. \quad (3.32)$$

The procedure for calculation of these integrals and their analytic expressions are presented in Appendix B.

The amplitudes for $\chi_{c_J}\to e^+e^-$ can be cast in the following simple form:

$$A(\chi_{c_1} \to e^+e^-) = g_1\bar{v}(l_+)\gamma_5\not{\epsilon}u(l_-), \quad (3.33)$$

$$A(\chi_{c_2} \to e^+e^-) = \frac{g_2}{M^2}\bar{v}(l_+)\gamma^\mu u(l_-)\epsilon_{\mu\nu}l^\nu, \quad (3.34)$$

where $g_{1,2}$ are the effective couplings, which come from loop integrals. In the short distance approximation the exact result for $g_{1,2}$ has the following form:

$$\begin{aligned} g_1 &= \frac{16\alpha^2 a}{\sqrt{m}M^2}\Bigg[\log\left(\frac{x}{1+x}\right)(1-x) \\ &\quad -\left(\log\left(\frac{x}{1-x}\right)+i\pi\right)(1+x)\Bigg], \end{aligned} \tag{3.35}$$

$$\begin{aligned} g_2 &= \frac{32\sqrt{2}\alpha^2 a}{3\sqrt{m}M^2}\Bigg[\left(\frac{1+x}{2}+\frac{8}{(1+x)^2}\right)\log(1-x) \\ &+\frac{3}{2}(1+x)\log(1+x)-2\left(1+x+\frac{2}{(1+x)^2}\right)\log(x) \\ &-\frac{8}{(1+x)^2}\log(2)-1-\frac{i\pi}{2}\left(1+x+\frac{8}{(1+x)^2}\right)\Bigg], \end{aligned} \tag{3.36}$$

where $x=\frac{4m^2}{M^2}$, $M=M_{\chi_{c_1}}$ for g_1 and $M=M_{\chi_{c_2}}$ for g_2. In the limit $b\to 0$ one recovers the leading order terms presented in [56] (up to factor 2 in the case of g_2 due to a misprint in [56]):

$$g_1 = -\frac{\alpha^2\sqrt{2}}{M_{\chi_{c_1}}^{5/2}}32a\log\frac{2b_1}{M_{\chi_{c_1}}}, \tag{3.37}$$

$$g_2 = \frac{\alpha^2}{M_{\chi_{c_2}}^{5/2}}64a\Big[\log\frac{2b_2}{M_{\chi_{c_2}}}+\frac{1}{3}(i\pi+\log 2-1)\Big], \tag{3.38}$$

where binding energies $b_i=2m-M_{\chi_{c_i}}$, The electronic widths are given by:

$$\Gamma(\chi_{c_1}\to e^+e^-)=\frac{1}{3}\frac{|g_1|^2}{4\pi}M_{\chi_{c_1}}, \tag{3.39}$$

$$\Gamma(\chi_{c_2}\to e^+e^-)=\frac{1}{5}\frac{|g_2|^2}{8\pi}M_{\chi_{c_2}}. \tag{3.40}$$

The values of the electronic widths depend on two parameters m - the effective charm quark mass related to the binding energy and a, which is proportional to the derivative of the χ_{c_J} radial wavefunction at the origin. Table 3.1 contains the comparison of the leading order approximation and the exact

	$\Gamma(\chi_{c_1} \to e^+e^-)$	$\Gamma(\chi_{c_2} \to e^+e^-)$
	$b = 0.5\ GeV$	
Leading term	0.0226 eV	0.0243 eV
exact result	0.0317 eV	0.0159 eV
	$b = -0.5\ GeV$	
Leading term	0.164 eV	0.0512 eV
exact result	0.141 eV	0.0731 eV

Table 3.1: Electronic widths for $b = -0.5\ GeV$ and $b = 0.5\ GeV$

results for χ_{c_1} and χ_{c_2} electronic widths calculated for two different values of the binding energy ($b = \pm 0.5$ GeV). The value $|\phi'(0)|^2 = 0.1\ GeV^5$ was assumed. As one can observe the electronic widths depend strongly on the value of b and the binding energy corrections are significant. They can reach up to 50% of the leading order terms. The sign of these corrections is positive for χ_{c_1}, while for χ_{c_2} it is negative. The electron mass corrections, which could be included in this calculation are negligible [58].

3.3.2 Short and long distance combined contributions

The model from the previous section, which describe coupling of the χ_{c_J} to two-photons exhibits the appropriate leading logarithmic behavior. However, as have been shown in the previous section, the other terms, which arise from the binding energy corrections are comparable in size. Other terms, not included in the model from the previous section, could also be of the same order or even bigger. For this reason the model from the previous section has been extended to describe appropriately the coupling of the χ_{c_J} to $\gamma\gamma$, $\gamma J/\psi$ and $\gamma\psi'$. The diagrams describing the decay $\chi_{c_J} \to \gamma\gamma$ in this model are presented in Fig. 3.2, while for the decay of $\chi_{c_J} \to \gamma J/\psi$ and $\psi' \to \chi_{c_J}\gamma$ are presented in Fig. 3.3. According to Landau-Yang theorem [59] the χ_{c_1} does not decay to two real photons. The adopted model assumes that the form of the χ_{c_i}-J/ψ-γ and χ_{c_i}-ψ'-γ amplitudes is identical to the χ_{c_i}-γ-γ amplitudes. Only the couplings are different. There is not enough experimental information, which allow to test this assumption in detail. For the non-zero amplitudes this leads to the following expressions [9]:

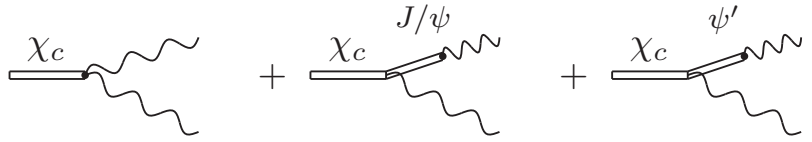

$$c_\gamma = \frac{4e^2}{\sqrt{m}}(a + \frac{f a_J}{M^2_{J/\psi}} + \frac{f' a_{\psi'}}{M^2_{\psi'}}) \frac{1}{(M^2_\chi/2 + b^2/4 + b M_\chi/2)^2}$$

Figure 3.2: Diagrams contributing to the decay widths $\Gamma(\chi_{c_{0,1,2}} \to \gamma\gamma)$.

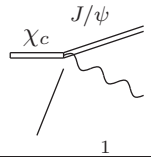

$$c_{J/\psi} = \frac{4e a_J}{\sqrt{m}} \frac{1}{(M^2_\chi/2 + b^2/4 + b M_\chi/2 - M^2_{J/\psi}/2)^2}$$

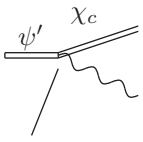

$$c_{\psi'} = \frac{4e a_{\psi'}}{\sqrt{m}} \frac{1}{(M^2_\chi/4 + m^2 - M^2_{\psi'}/2)^2}$$

Figure 3.3: Diagrams contributing to the decay widths $\Gamma(\chi_{c_{0,1,2}} \to \gamma J/\psi)$ and $\psi' \to \chi_{c_{0,1,2}}\gamma)$.

$$A^{\alpha\beta}_{1\gamma J/\psi}(p_1, p_2, \epsilon)\epsilon^1_\alpha \epsilon^2_\beta \Big|_{p_1^2=0,\ p_2^2=M^2_{J/\psi}} = ic^1_{J/\psi}\Big\{p_2^2(\epsilon, \epsilon_2, \epsilon_1, p_1) + \epsilon_1 p_1(\epsilon, \epsilon_2, p_1, p_2) + \epsilon_2 p_2(\epsilon, \epsilon_1, p_2, p_1)\Big\}, \tag{3.41}$$

$$A^{\alpha\beta}_{1\gamma\psi'}(p_1, p_2, \epsilon)\epsilon^1_\alpha \epsilon^2_\beta \Big|_{p_1^2=0,\ p_2^2=M^2_{\psi'}} = ic^1_{\psi'}\Big\{p_2^2(\epsilon, \epsilon_2, \epsilon_1, p_1) + \epsilon_1 p_1(\epsilon, \epsilon_2, p_1, p_2) + \epsilon_2 p_2(\epsilon, \epsilon_1, p_2, p_1)\Big\}, \tag{3.42}$$

$$A^{\alpha\beta}_{2\gamma\gamma}(p_1, p_2, \epsilon)\epsilon^1_\alpha \epsilon^2_\beta \Big|_{p_1^2=p_2^2=0} = \sqrt{2}c^2_\gamma M_{\chi_{c_2}}\Big\{(p_1 p_2)\epsilon^1_\mu \epsilon^2_\nu + p_{1\mu} p_{2\nu}(\epsilon_1 \epsilon_2) - p_{1\mu}\epsilon^2_\nu(\epsilon_1 p_2)) - p_{2\mu}\epsilon^1_\nu(\epsilon_2 p_1))\Big\}\epsilon^{\mu\nu}, \tag{3.43}$$

$$A^{\alpha\beta}_{2\gamma J/\psi}(p_1,p_2,\epsilon)\epsilon^1_\alpha\epsilon^2_\beta\Big|_{p_1^2=0,\ p_2^2=M^2_{J/\psi}} = \sqrt{2}c^2_{J/\psi}M_{\chi_{c_2}}\Big\{(p_1p_2)\epsilon^1_\mu\epsilon^2_\nu + p_{1\mu}p_{2\nu}(\epsilon_1\epsilon_2) - p_{1\mu}\epsilon^2_\nu(\epsilon_1p_2)) - p_{2\mu}\epsilon^1_\nu(\epsilon_2p_1))\Big\}\epsilon^{\mu\nu}, \quad (3.44)$$

$$A^{\alpha\beta}_{2\gamma\psi'}(p_1,p_2,\epsilon)\epsilon^1_\alpha\epsilon^2_\beta\Big|_{p_1^2=0,\ p_2^2=M^2_{\psi'}} = \sqrt{2}c^2_{\psi'}M_{\chi_{c_2}}\Big\{(p_1p_2)\epsilon^1_\mu\epsilon^2_\nu + p_{1\mu}p_{2\nu}(\epsilon_1\epsilon_2) - p_{1\mu}\epsilon^2_\nu(\epsilon_1p_2)) - p_{2\mu}\epsilon^1_\nu(\epsilon_2p_1))\Big\}\epsilon^{\mu\nu}. \quad (3.45)$$

In the case of the amplitudes $A_{i\gamma\gamma}$, p_1 and p_2 are the momenta of photons, and ϵ_1 and ϵ_2 are their polarization vectors. In the case of the amplitudes $A_{i\gamma J/\psi(\psi')}$, p_1 is the photon momentum, ϵ_1 is its polarization vector, p_2 is the $J/\psi(\psi')$ momentum and ϵ_2 its polarization vector. The function c_γ is the $\chi_{c_i}-\gamma-\gamma$ form factor, whereas $c_{J/\psi(\psi')}$ is the $\chi_{c_i}-\gamma-J/\psi(\psi')$ form factor. The modified $\chi_{c_i}-\gamma\gamma$ form factor, which takes into account γ-J/ψ and γ-ψ' mixings has the following form:

$$c^i_\gamma \equiv (1+\frac{f\cdot a_J}{aM^2_{J/\psi}}+\frac{f'\cdot a_{\psi'}}{aM^2_{\psi'}})c(M^2_{\chi_{c_i}},0,0,m) = \frac{16\pi\alpha}{\sqrt{m}}(a+\frac{fa_J}{M^2_{\psi'}}+\frac{f'\cdot a_{\psi'}}{M^2_{\psi'}})\frac{1}{\Big(M^2_{\chi_{c_i}}/2+b_i^2/4+b_iM_{\chi_{c_i}}/2\Big)^2}. \quad (3.46)$$

The constants f and f' have been extracted from the electronic widths of J/ψ and ψ' calculated according to the diagram from Fig. 3.4. This constants have the following form:

$$f = \sqrt{\frac{3\Gamma_{J/\psi\to e^+e^-}M^3_{J/\psi}}{4\pi\alpha^2}}, \quad (3.47)$$

$$f' = \sqrt{\frac{3\Gamma_{\psi'\to e^+e^-}M^3_{\psi'}}{4\pi\alpha^2}}. \quad (3.48)$$

The $\chi_{c_i}-\gamma-J/\psi$ and $\chi_{c_i}-\gamma-\psi'$ form factors have the following forms:

$$c^i_{J/\psi} \equiv \frac{a_J}{ae}c(M^2_{\chi_{c_i}},0,M^2_{J/\psi},m) = \frac{4ea_J}{\sqrt{m}}\frac{1}{\Big(M^2_{\chi_{c_i}}/2+b_i^2/4+b_iM_{\chi_{c_i}}/2-M^2_{J/\psi}/2\Big)^2}. \quad (3.49)$$

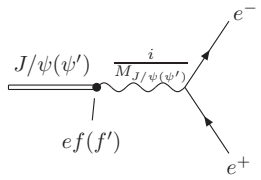

Figure 3.4: Diagram contributing to the decay width $\Gamma(J/\psi(\psi') \to e^+e^-)$.

$$c^i_{\psi'} \equiv \frac{a_{\psi'}}{ae} c(M^2_{\chi_{c_i}}, 0, M^2_{\psi'}, m) = \frac{4ea_{\psi'}}{\sqrt{m}} \frac{1}{\left(M^2_{\chi_{c_i}}/2 + b_i^2/4 + b_i M_{\chi_{c_i}}/2 - M^2_{\psi'}/2\right)^2}. \tag{3.50}$$

The couplings a_J and $a_{\psi'}$ are parameters, which can be related to the overlap integral of the radial wavefunctions calculated in the framework of potential models [60], but in this model they are treated as free parameters. The free parameters a, a_J, $a_{\psi'}$ and the effective charm quark mass m have been fitted to the experimental data. The observables used in the fit in the frame of described model have the following form [9]:

$$\Gamma(\chi_{c_1} \to J/\Psi\gamma) = \frac{1}{96\pi}|c^1_{J/\psi}|^2 M^2_{J/\Psi} M^3_{\chi_{c_1}}(1+x_1)(1-x_1)^3, \tag{3.51}$$

$$\Gamma(\chi_{c_2} \to \gamma\gamma) = \frac{1}{160\pi}|c^2_{\gamma}|^2 M^5_{\chi_{c_2}}, \tag{3.52}$$

$$\Gamma(\chi_{c_2} \to J/\Psi\gamma) = \frac{1}{80\pi}|c^2_{J/\psi}|^2 M^5_{\chi_{c_2}}(1-x_2)^3(1+x_2/2+x_2^2/6), \tag{3.53}$$

$$\Gamma(\psi' \to \chi_{c_1}\gamma) = \frac{1}{96\pi\bar{x}_1}|c^1_{\psi'}|^2 M^5_{\Psi'}(1+\bar{x}_1)(1-\bar{x}_1)^3, \tag{3.54}$$

$$\Gamma(\psi' \to \chi_{c_2}\gamma) = \frac{1}{288\pi\bar{x}_2}|c^1_{\psi'}|^2 M^5_{\Psi'}(1-\bar{x}_2)^3(1+3\bar{x}_2+6\bar{x}_2^2), \tag{3.55}$$

where $x_i = M^2_{J/\psi}/M^2_{\chi_{c_i}}$ and $\bar{x}_i = M^2_{\chi_{c_i}} M^2_{\psi'}$.

The extracted parameters of the model and experimental and theoretical values of the fitted decay widths are presented in the Table 3.2. The fit of 4 parameters to 5 experimental points gives $\chi^2 = 0.16$. One can obtain another minimum of the χ^2 with a similar numerical value, where the parameter $a_{\psi'}$ is positive. That solution was not considered since according to the potential models predictions [60] the $a_{\psi'}$ should be negative.

Within the described model the electronic widths of χ_{c_J} states are sums of 3 contributions presented in Fig. 3.5. The part from Fig. 3.5a has been

a[GeV$^{5/2}$]	$\lvert\phi'(0)\rvert^2$ [GeV^5]	m [GeV]	a_J	$a_{\psi'}$
0.0786	0.04	1.69	0.15	-0.07

widths [MeV]	χ_{c1}	χ_{c2}
$\Gamma(\chi \to \gamma\gamma)_{th}$	-	$5.288 \cdot 10^{-4}$
$\Gamma(\chi \to J/\psi\gamma)_{th}$	$2.803 \cdot 10^{-1}$	$3.778 \cdot 10^{-1}$
$\Gamma(\psi' \to \chi\gamma)_{th}$	$2.856 \cdot 10^{-2}$	$2.705 \cdot 10^{-2}$
$\Gamma(\chi \to \gamma\gamma)_{exp}$	-	$5.3(3) \cdot 10^{-4}$
$\Gamma(\chi \to J/\psi\gamma)_{exp}$	$2.8(2) \cdot 10^{-1}$	$3.7(3) \cdot 10^{-1}$
$\Gamma(\psi' \to \chi\gamma)_{exp}$	$2.8(1) \cdot 10^{-2}$	$2.7(1) \cdot 10^{-2}$

Table 3.2: Parameters obtained in the fit (see text for details) and theoretical (*th*), and experimental (*exp*) [61] values of $\Gamma(\chi_{c_{1,2}} \to \gamma\gamma, \gamma J/\psi)$ and $\Gamma(\psi' \to \gamma\chi_{c_{1,2}})$.

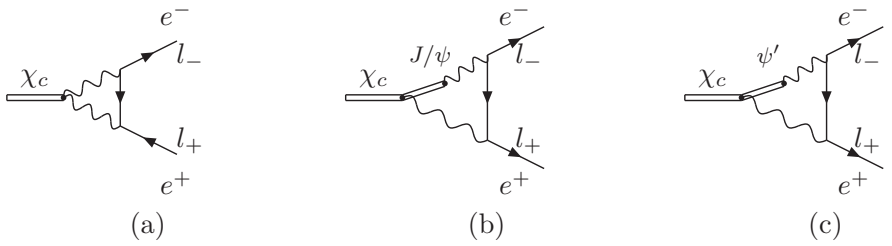

Figure 3.5: Diagrams for decay widths $\Gamma(\chi_{c_{0,1,2}} \to e^+e^-)$.

calculated in Section 3.3.1. The remaining two parts from Figs. 3.5b and 3.5c and the crossed diagrams have exactly the same structure, so it is sufficient to calculate only one of them. The difference between contributions from Fig. 3.5b and Fig. 3.5c appears only in the structure of imaginary parts of the scalar integrals, which enters the amplitudes since $M_{J\psi} < M_{\chi_{c_i}} < M_{\psi'}$, for $i = 1, 2$. The amplitudes coming from diagrams 3.5b and Fig. 3.5c, which contribute to the electronic widths of χ_{c_J} are given by the following loop

integrals:

$$\begin{aligned}\bar{A}(\chi_{c_1}\to e^+e^-) &= \frac{-32ie^2\pi\alpha a}{\sqrt{m}}\bar{v}(l_+)\gamma_5\Big\{\int\frac{d^4h}{(2\pi)^4}\\ &\frac{1}{h^2p_1^2p_2^2[p_2^2-M_x^2][(h-l_l)^2-m^2]^2}\Big(\\ &\not{\epsilon}[p_1^2p_2^2+\frac{1}{2}h^2(p_1^2+p_2^2)]-\epsilon\cdot h\not{h}(p_1^2+p_2^2)\Big)\Big\}u(l_-), \quad (3.56)\\ \bar{A}(\chi_{c_2}\to e^+e^-) &= \frac{-16ie^2\pi\alpha a\sqrt{2}M}{\sqrt{m}}\bar{v}(l_+)\epsilon^{\mu\nu}\int\frac{d^4h}{(2\pi)^4}\\ &\frac{1}{h^2p_1^2p_2^2[p_2^2-M_x^2][(h-l_l)^2-m^2]^2}\\ &\Big\{(l_+-l_-)_\mu\gamma_\nu h^2+2\not{h}h_\mu h_\nu\Big\}u(l_-), \quad (3.57)\end{aligned}$$

where $a_x = a_J$ and $M_x = M_{J/\psi}$ for J/ψ contribution and $f^x = f'$, $a_x = a_{\psi'}$ and $M_x = M_{\psi'}$ for ψ'. Crossing $e^- \leftrightarrow e^+$ in amplitude from Fig. 3.5a or 3.5b produces additional factor 2, which will be included in calculation of the electronic widths. The integrals from Eqs. 3.56 and 3.57 can be split into two contributions by making use of the following relation:

$$\frac{1}{p_2^2(p_2^2-M_x^2)} = -\frac{1}{M_x^2}\Big(\frac{1}{p_2^2}-\frac{1}{p_2^2-M_x^2}\Big). \quad (3.58)$$

Inserting this expression into Eq. 3.56 and 3.57 results in the following expressions:

$$\begin{aligned}\bar{A}(\chi_{c_1}\to e^+e^-) &= -\frac{1}{M_x}\Bigg(A(e^+e^-\to\chi_{c_1})\\ &+\frac{32ie^2\pi\alpha a}{\sqrt{m}}\bar{v}(l_+)\gamma_5\Big(\not{\epsilon}\bar{I}_1+\frac{1}{2}\bar{I}_2-\epsilon_\mu\gamma_\nu\bar{I}_3^{\mu\nu}\Big)u(l_-)\Bigg), \quad (3.59)\\ \bar{A}(\chi_{c_2}\to e^+e^-) &= -\frac{1}{M_x}\Bigg(A(e^+e^-\to\chi_{c_2})\\ &+\frac{16ie^2\pi\alpha a\sqrt{2}M}{\sqrt{m}}\bar{v}(l_+)\epsilon^{\mu\nu}\Big((l_+-l_-)_\mu\gamma_\nu\bar{I}_4+2\gamma^\alpha\bar{I}_{5\mu\nu\alpha}\Big)\Bigg). \quad (3.60)\end{aligned}$$

The first term in the bracket inserted into Eq. 3.56 and 3.57 produces the combination of the integrals (B.1-B.5). For the second term one obtains the

following integrals to be calculated:

$$\bar{I}_1 = \int d^4h \frac{p_2^2}{h^2[p_2^2 - M_x^2][(h-l_l)^2 - m^2]^2}, \tag{3.61}$$

$$\bar{I}_2 = \int d^4h \frac{p_1^2 + p_2^2}{p_1^2[p_2^2 - M_x^2][(h-l_l)^2 - m^2]^2}, \tag{3.62}$$

$$\bar{I}_3^{\mu\nu} = \int d^4h \frac{h^\mu h^\nu (p_1^2 + p_2^2)}{h^2 p_1^2[p_2^2 - M_x^2][(h-l_l)^2 - m^2]^2}, \tag{3.63}$$

$$\bar{I}_4 = \int d^4h \frac{1}{p_1^2[p_2^2 - M_x^2][(h-l_l)^2 - m^2]^2}, \tag{3.64}$$

$$\bar{I}_5^{\mu\nu\alpha} = \int d^4h \frac{h^\mu h^\nu h^\alpha}{h^2 p_1^2[p_2^2 - M_x^2][(h-l_l)^2 - m^2]^2}. \tag{3.65}$$

The procedure for calculation of these integrals and analytic expressions for them are presented in Appendix B.

The amplitudes describing decay of the $\chi_{c_{1,2}}$ into e^+e^- pair are given by Eqs. 3.33 and 3.34 with functions $g_{1,2}$ coming from the loop integrals. Combining the short and the long distance one gets:

$$g_{1,2} = g_{1,2_{\gamma\gamma}} + g_{1,2_{J/\psi\gamma}} + g_{1,2_{\psi'\gamma}}, \tag{3.66}$$

where $g_{1,2_{\gamma\gamma}}$ are given by the functions $g_{1,2}$ from Eqs. 3.35 and 3.36, and $g_{1,2_{J/\psi\gamma}}$ ($g_{1,2_{\psi'\gamma}}$) are given by the following formulae:

$$\begin{aligned} g_{1_{J/\psi\gamma}} = \frac{8\alpha^2 a_J f}{\sqrt{4\pi\alpha m} M^2 M_J^2} \Bigg[& \left(\log\left(\frac{x}{1-x}\right) + i\pi\right)\left(1 + x - \frac{y}{2}\right) \\ & + F_0(x,y) - \frac{1}{4}(3 + x + y) F_1(x,y) \\ & - \frac{y(4+y)}{2(2+2x-y)^2} F_2(x,y) + \frac{y(1+y-x)}{2(2+2x-y)} F_3(x,y) \\ & - \frac{y}{2} F_4(x,y) + \frac{y}{2}(3-x) F_5(x,y) \Bigg], \end{aligned} \tag{3.67}$$

$$
\begin{aligned}
g_{2_{J/\psi\gamma}} \quad &= \frac{16\sqrt{2}\alpha^2 a_J f}{3\sqrt{4\pi\alpha m}M^2 M_J^2}\Bigg[2 - \log(2)\left(3 - \frac{16}{(1+x)^2}\right) \\
&+ \log(x)\left(1 - y + 2x + \frac{8}{(1+x)^2}\right) \\
&+ \log(1-x)\left(\frac{1}{2} + y - 2x - \frac{16}{(1+x)^2}\right) \\
&- \frac{3y}{8}\log\left(\frac{y}{4}\right) + \log\left(1 - \frac{y}{4}\right)\left(-\frac{3}{2} + \frac{3y}{8}\right) \\
&+ i\pi\left(1 - \frac{11y}{8} + 2x + \frac{8}{(1+x)^2}\right) \\
&- F_0(x,y) - \left(\frac{1}{2} + y - \frac{x}{4}\right)F_1(x,y) \\
&+ \frac{-55 - 123xy + 126x + 93x^2 - 94y + 38y^2}{16(2+2x-y)^2}F_2(x,y) \\
&+ \frac{87 - 5xy - 2y + 2y^2 + 2x + 3x^2}{2(2+2x-y)}F_3(x,y) \\
&- \frac{3y}{4}F_4(x,y) - \frac{3y}{4}(1+x)F_5(x,y)\Bigg],
\end{aligned}
\tag{3.68}
$$

where $M = M_{\chi_{c_1}}$ in g_1; $M = M_{\chi_{c_2}}$ in g_2; $M_J \equiv M_{J/\psi}$ in both; $x \equiv 4m^2/M^2$,

$y \equiv 4M_{J/\psi}^2/M^2$. The functions $A(x,y)$ and F_i have the following form:

$$
\begin{aligned}
A(x,y) &= \operatorname{arc\,tg}\left(\frac{1-y+x}{2r}\right) - \operatorname{arc\,tg}\left(\frac{-1-y+x}{2r}\right), \\
F_0(x,y) &= \frac{1+y-x}{4}\log(x/y) - rA(x,y), \\
F_1(x,y) &= \log(x/y) + \frac{1+y-x}{r}A(x,y), \\
F_2(x,y) &= 2\log(2) - x\log(x) + y/2\log(y/2) \\
&-(1-x)\left(\log(1-x) - i\pi\right) \\
&+(2-y/2)\left(\log(2-y/2) - i\pi\right) \\
&+\frac{-1-x+y}{2}\log(x) + \frac{-1+x-y}{2}\log(y) \\
&-2rA(x,y), \\
F_3(x,y) &= -\frac{3}{2}\log(x) + \log(1-x) - i\pi \\
&+\frac{1}{2}\log(y) - \frac{1-x+y}{2r}A(x,y), \\
F_4(x,y) &= \log(1-2/y)\log(y/2) - Li_2(2/y) \\
&+Li_2\left(\frac{1-y/2}{1+x-y/2}\right) - Li_2\left(\frac{-y/2}{1+x-y/2}\right) \\
&-Li_2\left(\frac{1-y/2}{(1-x)/2+ir_1}\right) - Li_2\left(\frac{1-y/2}{(1-x)/2-ir_1}\right) \\
&+Li_2\left(\frac{-y/2}{(1-x)/2+ir_1}\right) + Li_2\left(\frac{-y/2}{(1-x)/2-ir_1}\right), \\
F_5(x,y) &= -\frac{1}{1+x-y/2}\log\left(\frac{1+x}{x}\right) \\
&+\frac{-r_1+i(1+y-x)/2}{(1-x+2ir_1)r_1}\log\left(\frac{(1-x+y)/2+ir_1}{(-1-x+y)/2+ir_1}\right) \\
&-\frac{r_1+i(1+y-x)/2}{(1-x-2ir_1)r_1}\log\left(\frac{(1-x+y)/2-ir_1}{(-1-x+y)/2-ir_1}\right)
\end{aligned}
\tag{3.69}
$$

with

$$r = \sqrt{x-(1-y+x)^2/4}, \tag{3.70}$$

and

$$r_1 = \sqrt{x-(1+y-x)^2/4}. \tag{3.71}$$

As the $M_{\psi'} > M_{\chi_{c_i}}$ an additional imaginary part appear and to obtain $g_{1,2_{\psi'\gamma}}$ from $g_{1,2_{J/\psi\gamma}}$ one need to set $M_J = M'_\psi$, $y = 4M^2_{\psi'}/M^2$ and the following

changes need to be done:

$$\begin{aligned} r_1 &= i\sqrt{x-(1+y-x)^2/4}, && (3.72)\\ \log(2-y/2) &\to \log(y/2-2)+i\pi, && (3.73)\\ \log(1-y/4) &\to \log(y/4-1)+i\pi. && (3.74) \end{aligned}$$

$$A(x,y) = \frac{r}{2\tilde{r}}\left\{\log\left[\frac{(1-y+x)/2-\tilde{r}}{(1-y+x)/2+\tilde{r}}\right]-\log\left[\frac{(-1-y+x)/2-\tilde{r}}{(-1-y+x)/2+\tilde{r}}\right]\right\}, \quad (3.75)$$

where $\tilde{r}=\sqrt{(1-y+x)^2/4-x}$.

Table 3.3 presents the results obtained for the electronic widths of χ_{c_1} and χ_{c_2} containing the sum of short and long distance results calculated according to the formulas from Eqs. 3.39 and 3.40. In the case of χ_{c_1} the additional contribution from the neutral current has been taken into account (see Section 3.2). The amplitude for coupling of χ_{c_1} to the neutral current has the following form:

$$\mathcal{M}(\chi_{c_1}\to Z^0\to e^+e^-) = J^{\mu}_{e^+e^-}D_{Z^0\mu\nu}(k)A^{\nu}_{(\chi_{c_1}-Z^0)} \quad (3.76)$$

with $A^{\nu}_{(\chi_{c_1}-Z^0)}$ given by the formula from Eq. 3.19 and

$$\begin{aligned} J^{\mu}_{e^+e^-} &= \frac{ig}{4\cos\theta_W}\gamma^{\mu}\Big(1-4\sin^2\theta_W-\gamma_5\Big), && (3.77)\\ D_{Z^0\mu\nu} &= \frac{-g_{\mu\nu}+\frac{k_\mu k_\nu}{M_Z^2}}{k^2-M_Z^2}, && (3.78) \end{aligned}$$

where M_Z is the mass of boson Z^0, g is electroweak coupling constant and θ_W is electroweak mixing angle. The electronic decay width of χ_{c_1} with including the neutral current contribution has the following form:

$$\begin{aligned} \Gamma(\chi_{c_1}\to e^+e^-) &= \frac{M_{\chi_{c_1}}}{3\pi}\left[\frac{|g_1|^2}{4}\right. && (3.79)\\ &+\frac{aG_F}{\sqrt{2m}Q^2}Re(g1)\\ &\left.+\frac{a^2G_F^2}{mQ^4}\left(1-4\sin^2\theta_W+8\sin^4\theta_W\right)\right], \end{aligned}$$

where G_F is the Fermi constant. In Table 3.3 the column denoted by QED represents the coherent sum of all contributions represented in Fig. 3.5. The

,

	QED	$\gamma\gamma$	$J/\psi\gamma$	$\psi'\gamma$	QED+Z^0
$\Gamma_{(\chi_{c_1}\to e^+e^-)}$ [eV]	0.43	0.10	0.008	0.094	0.41
$\Gamma_{(\chi_{c_2}\to e^+e^-)}$ [eV]	4.25	0.042	1.41	0.45	-

Table 3.3: Electronic widths for χ_{c_1} and χ_{c_2}.

individual contributions are presented in columns denoted by $\gamma\gamma$, $J/\psi\gamma$ and $\psi'\gamma$. The sum of electromagnetic and neutral current contributions for χ_{c_1} given in the last column is QED+Z^0. As one can observe the sum of the individual contributions is much smaller than the full result (QED). The neutral current does not affect a lot the value of χ_{c_1} electronic width. It can reach up a few percent of QED predictions. This result depends on the value of phase and module of g_1. For both states the values of electronic widths are sufficiently large to be observed in BES-III scan experiment [62]. In comparison with other models [58,62,63] the obtained values of electronic widths are much bigger. The verification of these predictions can be done at the BES-III experiment.

3.4 The amplitudes for the reaction $e^+e^- \to \chi_{c_J} \to \gamma J/\psi(\to \mu^+\mu^-)$

The signal of the χ_{c_1} and χ_{c_2} can be observed in the reaction $e^+e^- \to \chi_{c_J} \to \gamma J/\psi(\to \mu^+\mu^-)$, which allows to extract the electronic widths of this states. The Feynman diagrams, which were taken into account for this reaction are depicted in Fig. 3.6. The circles represents the couplings $g_{1,2}$ of the χ_{c_i} states to e^+e^- calculated in Section 3.3.2 according to the diagrams from Fig. 3.5.

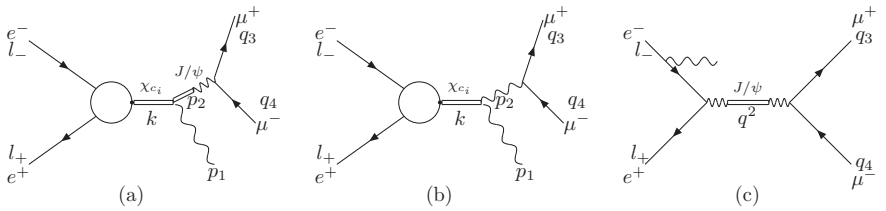

Figure 3.6: Diagrams for the cross section of the reaction $e^+e^- \to \chi_{c_J} \to \gamma J/\psi(\to \mu^+\mu^-)$.

First two diagrams presented in Figs. 3.6a and 3.6b are production of χ_{c_J} with its subsequential decay into $J/\psi\gamma$ and two photons respectively. The diagram, with the subsequential decay of χ_{c_i} into $\psi'\gamma$, which has the same analytic structure as diagram from Fig. 3.6a was also taken into account. The diagram from Fig. 3.6c represents non-reducible background to the signal reaction and also has to be taken into account. This amplitude has been already calculated in [25, 64].

The amplitudes for the signal reaction with decay of $\chi_{c_J} \to J/\psi\gamma$ within the adopted model have the following form:

$$\begin{aligned}
\mathcal{M}_1 &= \Big\{ g_1 \bar{v}(l_+)\gamma_5\gamma^\mu u(l_-) \\
&+ \frac{2aG_F M^2_{\chi_{c_1}}}{f_1 f_2} \bar{v}(l_+) \Big((1 + 2m/M_{\chi_{c_1}})\gamma_5\gamma^\mu \\
&+ (1 - 4\sin^2\theta_W + 2m/M_{\chi_{c_1}} \\
&- 8m/M_{\chi_{c_1}} sin^2\theta_W)\gamma^\mu \Big) u(l_-) \Big\} \\
&\Pi^{\chi_{c1}}_{\mu\nu}(k)\ A_1^{\nu\beta}\ \Pi^{J/\psi}_{\beta\delta}(p_2)\ e\ \bar{u}(q_3)\gamma^\delta v(q_4),
\end{aligned} \tag{3.80}$$

$$\begin{aligned}
\mathcal{M}_2 &= g_2 \bar{v}(l_+)\gamma^\mu u(l_-)(l^\nu_+ - l^\nu_-)/M_{\chi_{c_2}} \\
&\Pi^{\chi_{c2}}_{\mu\nu\alpha\beta}(k)\ A_2^{\alpha\beta\gamma}\ \Pi^{J/\psi}_{\gamma\delta}(p_2)\ e\ \bar{u}(q_3)\gamma^\delta v(q_4),
\end{aligned} \tag{3.81}$$

where $f_2 = (M_{\chi_{c_1}}/2 + m)M_{\chi_{c_1}} 2\sqrt{2}$, $f_1 = \sqrt{m}Q^2$. For χ_{c_1} the amplitude for $e^+e^- \to Z^0 \to \chi_{c_1}$ from Eq. 3.76 has been used to calculate the neutral current contribution to the signal reaction. The amplitudes $A_i^{\nu\beta}$ can be found in Appendix B of [56],

$$A_1^{\nu\beta} = -i\frac{1}{2}c(I_1^{1\nu\beta} + I_2^{1\nu\beta}), \tag{3.82}$$

$$A_2^{\alpha\beta\gamma} = -c\sqrt{2}M_{\chi_{c_2}} I_2^{2\alpha\beta\gamma}, \tag{3.83}$$

and coincide with Eq.(3.15) and Eq.(3.16). The $c \equiv c^i_{J/\psi}$ is given by the formula from Eq. 3.50. Here the contributions I_1^1, I_2^1 and I_2^2 are given by:

$$I_1^{1\nu\beta} = \epsilon^{\bar{\mu}\bar{\nu}\beta\nu} F^1_{\bar{\mu}\bar{\nu}} p^2_{\bar{\gamma}} p^{2\bar{\gamma}} - \epsilon^{\bar{\mu}\bar{\nu}\bar{\alpha}\nu} F^1_{\bar{\mu}\bar{\nu}} p^2_{\bar{\alpha}} p^{2\beta}, \tag{3.84}$$

$$I_2^{1\nu\beta} = 0, \tag{3.85}$$

$$I_2^{2\alpha\beta\gamma} = F^{1\alpha\delta}\left(g^{\beta\gamma} p^2_\delta - g^\gamma_\delta p^{2\beta}\right), \tag{3.86}$$

where

$$F^1_{\mu\nu} = \epsilon^1_\mu p^1_\nu - \epsilon^1_\nu p^1_\mu. \tag{3.87}$$

The $\Pi^{J/\psi}_{\beta\delta}(p)$ has the following form:

$$\Pi^{J/\psi}_{\beta\delta}(p) = \sqrt{\frac{3\Gamma_{J/\psi\to e^+e^-}}{\alpha\sqrt{p_2^2}}}\frac{g_{\beta\delta} - p_\beta p_\delta/M^2_{J/\psi}}{p_2^2 - M^2_{J/\psi} + iM_{J/\psi}\Gamma_{J/\psi}}, \tag{3.88}$$

where p is momentum of J/ψ and the factor $\sqrt{\frac{3\Gamma_{J/\psi\to e^+e^-}}{\alpha\sqrt{p_2^2}}}$ is the coupling of J/ψ to two muons. The propagators of χ_{c_1} has the following form:

$$\Pi^{\chi_{c1}}_{\mu\nu}(k) = \frac{g_{\mu\nu} - k_\beta k_\delta/M^2_{\chi_{c1}}}{k^2 - M^2_{\chi_{c_1}} + i\Gamma_{\chi_{c_1}}M_{\chi_{c_1}}}, \tag{3.89}$$

where k is the four-momentum of the χ_{c1}. $M_{\chi_{c_1}}$ and $\Gamma_{\chi_{c_1}}$ are its mass and its decay width respectively. The χ_{c_2} propagators $\Pi^{\chi_{c2}}$ has the following form:

$$\Pi^{\chi_{c2}}_{\mu\nu\alpha\beta}(k) = \frac{B_{\mu\nu\alpha\beta}}{k^2 - M^2_{\chi_{c_2}} + i\Gamma_{\chi_{c_2}}M_{\chi_{c_2}}}, \tag{3.90}$$

where k is the four-momentum of the χ_{c_2}, $M_{\chi_{c_2}}$ and $\Gamma_{\chi_{c_2}}$ are its mass and its decay width respectively. The tensor $B_{\mu\nu\alpha\beta}$ has the following form:

$$B_{\mu\nu\alpha\beta} = \frac{1}{2}(P_{\mu\alpha}P_{\nu\beta} + P_{\mu\beta}P_{\nu\alpha}) - \frac{1}{3}P_{\mu\nu}P_{\alpha\beta}), \tag{3.91}$$

where $P_{\mu\nu} = -g_{\mu\nu} + k_\mu k_\nu/M_{\chi_{c_2}}$.

In the Monte Carlo generator PHOKHARA, the peak in the phase space, which comes from J/ψ has been absorbed using standard change of variables as it was done previously in implementation of narrow resonances [25].

3.5 Monte Carlo simulations

The plots from Figs. 3.7 and 3.8 show the cross section of the reaction $e^+e^- \to \mu^+\mu^-\gamma$, with (ISR+QED signal) and without (ISR background) including the amplitude for the $\chi_{c_{1,2}}$ production. Additionally the influence of the neutral current is presented for χ_{c_1} (ISR+QED signal+Z^0). The $\chi_{c_{1,2}}$ production cross sections without including the interference with the background, denoted as $\chi_{c_{1,2}}$ signal are also shown on the plots from Fig. 3.7 and 3.8. For χ_{c_1} on a separate plot, because of the smallness of the cross section. The event selections involve angular cuts on photon and muons. The range of the polar

angles are $20^o < \theta_{\mu^\pm,\gamma} < 160^o$. The range of the invariant mass of the muons was limited to to the interval $[M_{J/\psi} - 3\Gamma_{J/\psi},\ M_{J/\psi} + 3\Gamma_{J/\psi}]$. For this event selections the contributions from the diagram from Fig. 3.6b and 3.6a, where J/ψ is substituted by ψ' are negligible. Since neutral current contribution is tiny, the additional diagram similar to the one presented in Fig. 3.6c with γ substituted with Z^0, which contribute to the background is also very small but nevertheless has been included in the simulations. The plots for the cross section of the reaction $e^+e^- \to \mu^+\mu^-\gamma$ with the same event selections except including angular cuts on photons are presented in Figs. 3.9 and 3.10, where the $\chi_{c_{1,2}}$ production cross sections was not shown separately. A beam spread distributed according the Gaussian function with 1 MeV per beam was assumed.

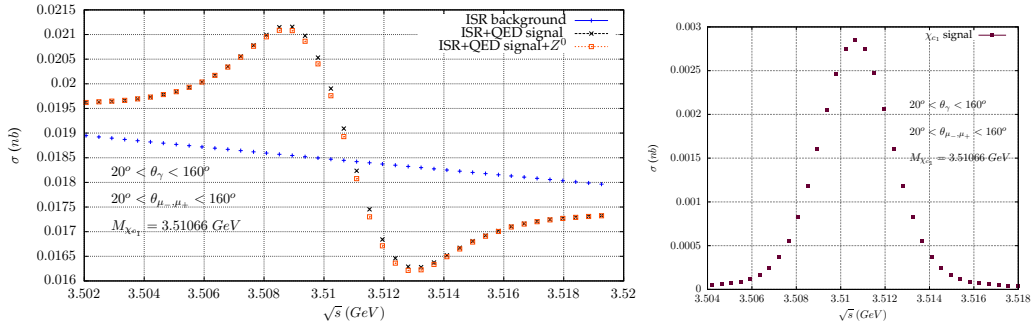

(a) (b)

Figure 3.7: The cross section $e^+e^- \to \mu^+\mu^-\gamma$.

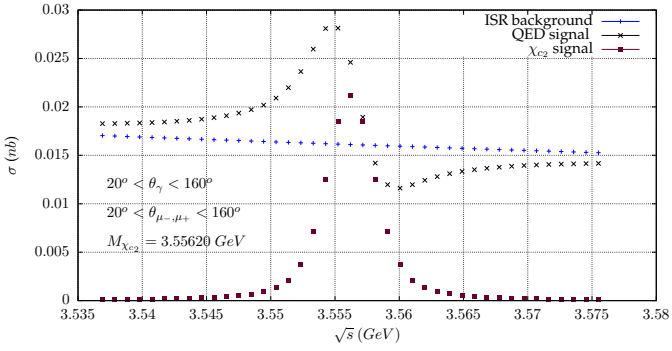

Figure 3.8: The cross section $e^+e^- \to \mu^+\mu^-\gamma$.

A signal up to 13% for χ_{c_1} and up to 75% for χ_{c_2} of the radiative return background can be observed in the case of event selections, where one impose

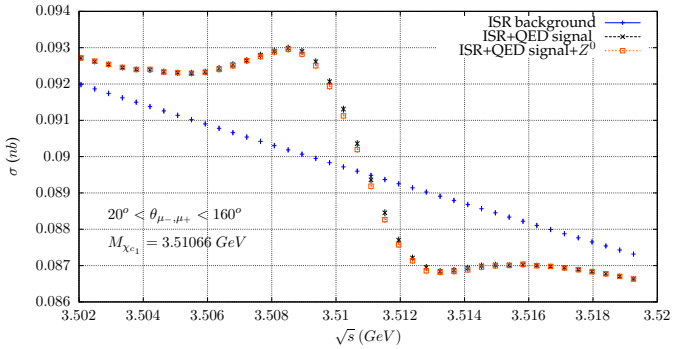

Figure 3.9: The cross section $e^+e^- \to \mu^+\mu^-\gamma$.

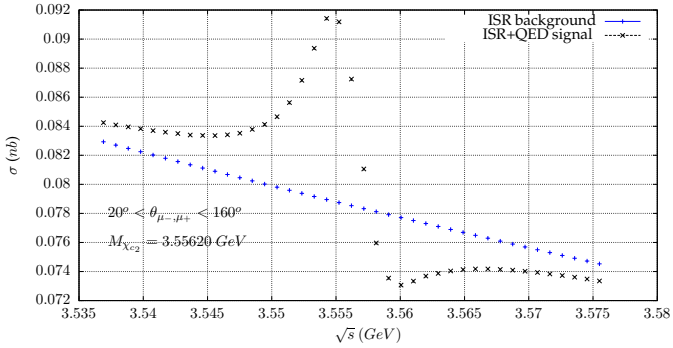

Figure 3.10: The cross section $e^+e^- \to \mu^+\mu^-\gamma$.

angular cuts on photon. Without including this cuts the cross section is bigger but the relative difference between signal and background is smaller. For these event selections the signal can reach up to 3% for χ_{c_1} and up to 16% for χ_{c_2}. As one can observe for the beam energy equal to the mass of χ_{c_J} resonances, the signal cross section is close to zero for χ_{c_1}, while for χ_{c_2} it can reach only up to 50 % of total signal. This could be also inferred from the size of $\chi_{c_{1,2}}$ production cross sections. The interference effects between the signal and the radiative return background plays crucial role for both χ_{c_1} and χ_{c_2}. The main contribution to the $\chi_{c_{1,2}}$ production come from the interference between signal and radiative return background amplitudes. In both cases the interference enhance cross section below and above the threshold of the production of χ_{c_1} and χ_{c_2} states. To verify the predictions of the model one needs to perform energy scan in the vicinity of χ_{c_1} (χ_{c_2}) mass. The size of the signal is in the range of the sensitivity of the BES-III collaboration.

3.6 Conclusions

In the framework of the adopted model the production of the χ_{c_1} and χ_{c_2} resonances in the electron-positron annihilation through two-virtual photons can be measured by BES-III collaboration in the reaction $e^+e^- \to \chi_{c_J} \to \gamma J/\psi(\to \mu^+\mu^-)$. The scan experiment in the vicinity of χ_{c_1} (χ_{c_2}) should be able to measure the cross section and extract the electronic widths of these states if the model is correct. The important part of the signal is the interference between the production amplitude and the radiative return background amplitude, which lead to a measurable effect.

Chapter 4

Modeling the interactions of photons with pseudoscalar and vector mesons and its application to the reaction $e^+e^- \to P\gamma(\gamma)$

4.1 Motivation

The modeling of the interactions of photons and pseudoscalar mesons is necessary to describe correctly many experimental data, which could be predicted from the interaction Lagrangians.

One of the outcome of this modeling are pseudoscalar transition form factors. These form factors in the space-like region are necessary for a precise determination of the hadronic light-by-light contribution to the anomalous magnetic moment of the muon. The modeling of these form factors in the space-like region using Lagrangian formalism was described in [65]. This model is extended to cover also the time-like region. It describes correctly many other experimental data in the time-like region [10, 11]. It can be then used to make predictions for the cross section of the reaction $e^+e^- \to P(\gamma)$, where $P = \pi^0$, η, η'. The Lagrangian approach for modeling of the interaction of photons with vector and pseudoscalar mesons [11] presented here might be compared with the similar approach, which is based on the hidden local symmetry effective Lagrangian [66–68]. This comparison could enable to study the model dependence of the obtained results.

In Section 4.2 the modeling of the pseudoscalar two-photon transition

form factors using Lagrangian formalism is presented and comparison of the theoretical model with experimental data is widely discussed. In Section 4.3 the application of the form factor model to the reaction $e^+e^- \to P\gamma(\gamma)$ is presented. Section 4.4 contains the result of the Monte Carlo simulations for this reaction. Section 4.5 contains conclusions.

4.2 The transition form factors

4.2.1 The model

The developed phenomenological model of the transition form factors for pseudoscalar mesons presented here is based on the chiral effective theory with resonances [69–71]. The model described in this section is the minimal possible way of an extension of the model presented in [65], which allows to describe correctly all possible experimental data in the space-like and the time-like regions. The SU(3) isospin symmetry, which was assumed in [65], is explicitly broken by coupling constants. The number of vector meson octets essential to accommodate data in the time-like region is three, while in the case of the form factors in the space-like region two vector meson octets were sufficient. The $\eta - \eta'$ mixing scheme was adopted from [72,73] with the values of mixing parameters fitted to the new available experimental data.

Below, the Lagrangians necessary to model the pseudoscalar form factors are given. The Wess-Zumino Lagrangian [74, 75] for interaction of pseudoscalar mesons with two-photons has the following form:

$$\begin{aligned}\mathcal{L}_{\gamma\gamma P} &= \frac{-e^2 N_c}{24\pi^2 f_\pi}\epsilon^{\mu\nu\alpha\beta}\partial_\mu B_\nu \partial_\alpha B_\beta \Big[\pi^0 + \eta(\frac{5}{3}C_q - \frac{\sqrt{2}}{3}C_s) \\ &+ \eta'(\frac{5}{3}C'_q + \frac{\sqrt{2}}{3}C'_s)\Big] . \end{aligned} \tag{4.1}$$

The η-η' mixing parameters C_q, C'_q, C_s, C'_s are given by the following formulae [72]

$$C_q = \frac{f_\pi}{\sqrt{3}\cos(\theta_8 - \theta_0)}\Big(\frac{1}{f_8}\cos\theta_0 - \frac{1}{f_0}\sqrt{2}\sin\theta_8\Big), \tag{4.2}$$

$$C_s = \frac{f_\pi}{\sqrt{3}\cos(\theta_8 - \theta_0)}\Big(\frac{1}{f_8}\sqrt{2}\cos\theta_0 + \frac{1}{f_0}\sin\theta_8\Big), \tag{4.3}$$

$$C'_q = \frac{f_\pi}{\sqrt{3}\cos(\theta_8 - \theta_0)}\Big(\frac{1}{f_0}\sqrt{2}\cos\theta_8 + \frac{1}{f_8}\sin\theta_0\Big), \tag{4.4}$$

$$C'_s = \frac{f_\pi}{\sqrt{3}\cos(\theta_8 - \theta_0)}\Big(\frac{1}{f_0}\cos\theta_8 - \frac{1}{f_8}\sqrt{2}\sin\theta_0\Big). \tag{4.5}$$

The γV mixing is described in terms of the following Lagrangian:

$$\mathcal{L}_{\gamma V} = -e\sum_{i=1}^{3} f_{V_i}\partial_\mu B_\nu\Big(\tilde{\rho}_i^{\mu\nu} + \frac{1}{3}F_{\omega_i}\tilde{\omega}_i^{\mu\nu} - \frac{\sqrt{2}}{3}F_{\phi_i}\tilde{\phi}_i^{\mu\nu}\Big), \tag{4.6}$$

where $\tilde{V}_{\mu\nu} \equiv \partial_\mu V_\nu - \partial_\nu V_\mu$, f_{V_i} is a dimensionless coupling for the vector representation of the spin-1 fields in a given octet. The isospin symmetry is broken here by introducing the coupling constants F_{ω_i} and F_{ϕ_i}, which are different from 1 for first octet. For higher octets the SU(3) symmetry is kept unbroken and $F_{\omega_i} = F_{\phi_i} = 1$ for $i = 2, 3$.

The Lagrangians that describe vector-photon-pseudoscalar and two vector mesons interaction with a pseudoscalar come from the extension of the Lagrangians from [71], which were adopted in [65]. In terms of the physical fields they read

$$\mathcal{L}_{V\gamma\pi^0} = -\sum_{i=1}^{n}\frac{4\sqrt{2}eh_{V_i}}{3f_\pi}\epsilon_{\mu\nu\alpha\beta}\partial^\alpha B^\beta\Big(\rho_i^\mu + 3H_{\omega_i}\omega_i^\mu - \frac{3}{\sqrt{2}}A_i^{\pi_0}\phi_i^\mu\Big)\partial^\nu\pi^0\,, \tag{4.7}$$

$$\begin{aligned}\mathcal{L}_{V\gamma\eta} &= -\sum_{i=1}^{n}\frac{4\sqrt{2}eh_{V_i}}{3f_\pi}\epsilon_{\mu\nu\alpha\beta}\partial^\alpha B^\beta\Big[(3\rho_i^\mu + \omega_i^\mu)C_q + 2\phi_i^\mu C_s \\ &\quad -(\frac{5}{\sqrt{2}}C_q - C_s)A_i^\eta\phi_i^\mu\Big]\partial^\nu\eta\,,\end{aligned} \tag{4.8}$$

$$\begin{aligned}\mathcal{L}_{V\gamma\eta'} &= -\sum_{i=1}^{n}\frac{4\sqrt{2}eh_{V_i}}{3f_\pi}\epsilon_{\mu\nu\alpha\beta}\partial^\alpha B^\beta\Big[(3\rho_i^\mu + \omega_i^\mu)C_q' - 2\phi_i^\mu C_s' \\ &\quad -(\frac{5}{\sqrt{2}}C_q' + C_s')A_i^{\eta'}\phi_i^\mu\Big]\partial^\nu\eta'\,,\end{aligned} \tag{4.9}$$

$$\begin{aligned}\mathcal{L}_{VV\pi^0} &= -\sum_{i=1}^{n}\frac{4\sigma_{V_i}}{f_\pi}\epsilon_{\mu\nu\alpha\beta}\Big[\frac{1}{F_{\omega_i}}\pi^0\partial^\mu\omega_i^\nu\partial^\alpha\rho_i^\beta + \frac{3(F_{\omega_i}H_{\omega_i} - 1 - A_{\phi\omega,i}^{\pi^0})}{2F_{\omega_i}^2} \\ &\quad \pi^0\partial^\mu\omega_i^\nu\partial^\alpha\omega_i^\beta + \frac{3(A_i^{\pi_0} - A_{\phi\omega,i}^{\pi^0}/F_{\phi_i})}{4F_{\phi_i}}\pi^0\partial^\mu\phi_i^\nu\partial^\alpha\phi_i^\beta \\ &\quad -\frac{3A_{\phi\omega,i}^{\pi^0}}{\sqrt{2}F_{\omega_i}F_{\phi_i}}\pi^0\partial^\mu\phi_i^\nu\partial^\alpha\omega_i^\beta\Big],\end{aligned} \tag{4.10}$$

$$\mathcal{L}_{VV\eta} = -\sum_{i=1}^{n}\frac{4\sigma_{V_i}}{f_\pi}\epsilon_{\mu\nu\alpha\beta}\eta\Big[(\partial^\mu\rho_i^\nu\partial^\alpha\rho_i^\beta+\frac{1}{F_{\omega_i}}\partial^\mu\omega_i^\nu\partial^\alpha\omega_i^\beta)\frac{1}{2}C_q$$
$$-\frac{9A^\eta_{\phi\omega_i}}{F^2_{\omega_i}}\partial^\mu\omega_i^\nu\partial^\alpha\omega_i^\beta-\frac{1}{F_{\phi_i}}\partial^\mu\phi_i^\nu\partial^\alpha\phi_i^\beta\frac{1}{\sqrt{2}}C_s-\frac{9A^\eta_{\phi\omega,i}}{2F^2_{\phi_i}}\partial^\mu\phi_i^\nu\partial^\alpha\phi_i^\beta$$
$$+\frac{A_i^\eta}{6F_{\phi_i}}(\frac{15}{2}C_q-\frac{3}{\sqrt{2}}C_s)\partial^\mu\phi_i^\nu\partial^\alpha\phi_i^\beta-\frac{9\sqrt{2}A^\eta_{\phi\omega,i}}{F_{\omega_i}F_{\phi_i}}\partial^\mu\phi_i^\nu\partial^\alpha\omega_i^\beta\Big], \quad (4.11)$$

$$\mathcal{L}_{VV\eta'} = -\sum_{i=1}^{n}\frac{4\sigma_{V_i}}{f_\pi}\epsilon_{\mu\nu\alpha\beta}\eta'\Big[(\partial^\mu\rho_i^\nu\partial^\alpha\rho_i^\beta+\frac{1}{F_{\omega_i}}\partial^\mu\omega_i^\nu\partial^\alpha\omega_i^\beta)\frac{1}{2}C'_q$$
$$+\frac{1}{F_{\phi_i}}\partial^\mu\phi_i^\nu\partial^\alpha\phi_i^\beta\frac{1}{\sqrt{2}}C'_s+\frac{A_i^{\eta'}}{6F_{\phi_i}}(\frac{15}{2}C'_q+\frac{3}{\sqrt{2}}C'_s)\partial^\mu\phi_i^\nu\partial^\alpha\phi_i^\beta\Big], \quad (4.12)$$

where $n=3$, $H_{\omega_i}, F_{\phi_i}=1$ for $i=2,3$, $A^P_{\phi\omega,i}\neq 0$ only for $i=1$.

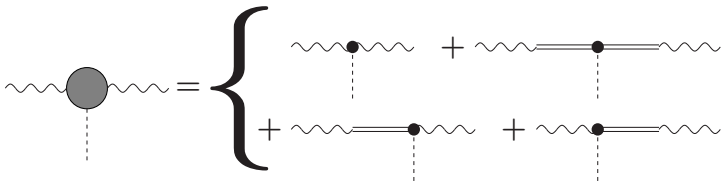

Figure 4.1: Feynman diagrams contributing to the pseudoscalar transition form factor. Double solid line represents vector meson and dashed line represents a pseudoscalar meson.

From the Lagrangians, Eqs.(4.1-4.12), one derives the $P-\gamma^*-\gamma^*$ coupling

$$\mathcal{M}[P\to\gamma^*(q_1)\,\gamma^*(q_2)]=e^2\epsilon_{\mu\nu\alpha\beta}q_1^\mu q_2^\alpha F_{\gamma^*\gamma^*P}(t_1,t_2). \quad (4.13)$$

The pseudoscalar transition form factor $F_{\gamma^*\gamma^*P}$ ($P=\pi^0,\ \eta,\ \eta'$) can be represented by the sum of the diagrams from Fig. 4.1. These diagrams represent the allowed $\gamma^*\gamma^*P$ transitions within the adopted model.

From the interaction Lagrangians and amplitude 4.13 one can extract the

following expressions for $F_{\gamma^*\gamma^*P}$ transition form factors:

$$
\begin{aligned}
F_{\gamma^*\gamma^*\pi^0}(t_1,t_2) &= -\frac{N_c}{12\pi^2 f_\pi} \\
&+\sum_{i=1}^{n}\frac{4\sqrt{2}h_{V_i}f_{V_i}}{3f_\pi}t_1\Big(D_{\rho_i}(t_1)+F_{\omega_i}H_{\omega_i}D_{\omega_i}(t_1)+A_i^{\pi^0}F_{\phi_i}D_{\phi_i}(t_1)\Big) \\
&+\sum_{i=1}^{n}\frac{4\sqrt{2}h_{V_i}f_{V_i}}{3f_\pi}t_2\Big(D_{\rho_i}(t_2)+F_{\omega_i}H_{\omega_i}D_{\omega_i}(t_2)+A_i^{\pi^0}F_{\phi_i}D_{\phi_i}(t_2)\Big) \\
&-\sum_{i=1}^{n}\frac{4\sigma_{V_i}f_{V_i}^2}{3f_\pi}t_1t_2\Bigg(D_{\rho_i}(t_2)D_{\omega_i}(t_1)+D_{\rho_i}(t_1)D_{\omega_i}(t_2) \\
&+(A_i^{\pi^0}F_{\phi_i}-A_{\phi\omega,i}^{\pi^0})D_{\phi_i}(t_1)D_{\phi_i}(t_2)+\Big(F_{\omega_i}H_{\omega_i}-1-A_{\phi\omega,i}^{\pi^0}\Big) \\
&D_{\omega_i}(t_1)D_{\omega_i}(t_2)+A_{\phi\omega,i}^{\pi^0}\Big(D_{\phi_i}(t_1)D_{\omega_i}(t_2)+D_{\phi_i}(t_1)D_{\omega_i}(t_2)\Big)\Bigg), \qquad (4.14)
\end{aligned}
$$

$$
\begin{aligned}
F_{\gamma^*\gamma^*\eta}(t_1,t_2) &= -\frac{N_c}{12\pi^2 f_\pi}\Big(\frac{5}{3}C_q-\frac{\sqrt{2}}{3}C_s\Big) \\
&+\sum_{i=1}^{n}\frac{4\sqrt{2}h_{V_i}f_{V_i}}{3f_\pi}t_1\Bigg(\Big(3C_qD_{\rho_i}(t_1)+\frac{1}{3}F_{\omega_i}C_qD_{\omega_i}(t_1) \\
&-\frac{2\sqrt{2}}{3}C_sF_{\phi_i}D_{\phi_i}(t_1)\Big)+\Big(\frac{5}{3}C_q-\frac{\sqrt{2}}{3}C_s\Big)A_i^{\eta}F_{\phi_i}D_{\phi_i}(t_1)\Bigg) \\
&+\sum_{i=1}^{n}\frac{4\sqrt{2}h_{V_i}f_{V_i}}{3f_\pi}t_2\Bigg(\Big(3C_qD_{\rho_i}(t_2)+\frac{1}{3}C_qF_{\omega_i}D_{\omega_i}(t_2) \\
&-\frac{2\sqrt{2}}{3}C_sF_{\phi_i}D_{\phi_i}(t_2)\Big)+\Big(\frac{5}{3}C_q-\frac{\sqrt{2}}{3}C_s\Big)A_i^{\eta}F_{\phi_i}D_{\phi_i}(t_2)\Bigg) \\
&-\sum_{i=1}^{n}\frac{8\sigma_{V_i}f_{V_i}^2}{f_\pi}t_1t_2\Bigg[\Big(\frac{1}{2}C_qD_{\rho_i}(t_1)D_{\rho_i}(t_2)+\frac{1}{18}F_{\omega_i}C_qD_{\omega_i}(t_1)D_{\omega_i}(t_2) \\
&-A_{\phi\omega,i}^{\eta}D_{\omega_i}(t_1)D_{\omega_i}(t_2)-\frac{\sqrt{2}}{9}C_sF_{\phi_i}D_{\phi_i}(t_1)D_{\phi_i}(t_2)\Big) \\
&+\frac{A_i^{\eta}F_{\phi_i}}{6}\Big(\frac{5}{3}C_q-\frac{\sqrt{2}}{3}C_s\Big)D_{\phi_i}(t_1)D_{\phi_i}(t_2)-A_{\phi\omega,i}^{\eta}D_{\phi_i}(t_1)D_{\phi_i}(t_2) \\
&+A_{\phi\omega,i}^{\eta}\Big(D_{\phi_i}(t_1)D_{\omega_i}(t_2)+D_{\phi_i}(t_1)D_{\omega_i}(t_2)\Big)\Bigg], \qquad (4.15)
\end{aligned}
$$

and

$$
\begin{aligned}
F_{\gamma^*\gamma^*\eta'}(t_1,t_2) &= -\frac{N_c}{12\pi^2 f_\pi}\Big(\frac{5}{3}C'_q+\frac{\sqrt{2}}{3}C'_s\Big) \\
&+\sum_{i=1}^{n}\frac{4\sqrt{2}h_{V_i}f_{V_i}}{3f_\pi}t_1\Bigg(\Big(3C'_qD_{\rho_i}(t_1)+\frac{1}{3}F_{\omega_i}C'_qD_{\omega_i}(t_1) \\
&+\frac{2\sqrt{2}}{3}C'_sF_{\phi_i}D_{\phi_i}(t_1)\Big)+\Big(\frac{5}{3}C'_q+\frac{\sqrt{2}}{3}C'_s\Big)A_i^{\eta'}F_{\phi_i}D_{\phi_i}(t_1)\Bigg) \\
&+\sum_{i=1}^{n}\frac{4\sqrt{2}h_{V_i}f_{V_i}}{3f_\pi}t_2\Bigg(\Big(3C'_qD_{\rho_i}(t_2)+\frac{1}{3}F_{\omega_i}C'_qD_{\omega_i}(t_2) \\
&+\frac{2\sqrt{2}}{3}C'_sF_{\phi_i}D_{\phi_i}(t_2)\Big)+\Big(\frac{5}{3}C'_q+\frac{\sqrt{2}}{3}C'_s\Big)A_i^{\eta'}F_{\phi_i}D_{\phi_i}(t_2)\Bigg) \\
&-\sum_{i=1}^{n}\frac{8\sigma_{V_i}f_{V_i}^2}{f_\pi}t_1t_2\Bigg[\Big(\frac{1}{2}C'_qD_{\rho_i}(t_1)D_{\rho_i}(t_2)+\frac{1}{18}F_{\omega_i}C'_qD_{\omega_i}(t_1)D_{\omega_i}(t_2) \\
&+\frac{\sqrt{2}}{9}C'_sF_{\phi_i}D_{\phi_i}(t_1)D_{\phi_i}(t_2)\Big)+\frac{A_i^{\eta'}F_{\phi_i}}{6}\Big(\frac{5}{3}C'_q+\frac{\sqrt{2}}{3}C'_s\Big)D_{\phi_i}(t_1)D_{\phi_i}(t_2)\Bigg],
\end{aligned}
\tag{4.16}
$$

where the vector meson propagators $D_{V_i}(Q^2)$ in the space-like region are defined by:

$$D_{V_i}(Q^2)=[Q^2-M_{V_i}^2]^{-1}. \tag{4.17}$$

The propagators $D_{V_i}(Q^2)$ in the time-like region have the following form:

$$D_{V_i}(Q^2)=[Q^2-M_{V_i}^2+i\sqrt{Q^2}\Gamma_{V_i}]^{-1}. \tag{4.18}$$

The M_{V_i} is a vector meson mass and Γ_{V_i} is vector meson width. The form factors fulfill the following high energy condition, which is predicted by perturbative Quantum Chromodynamics [23]:

$$\lim_{t_1\to\pm\infty}F_{\gamma^*\gamma^*P}(t_1,t_2)=0, \tag{4.19}$$

which holds for any value of t_2. That condition leads to the the following asymptotic relations between coupling constants:

$$-\frac{N_c}{4\pi^2}+4\sqrt{2}\sum_{i=1}^{n}h_{V_i}f_{V_i}(1+F_{\omega_i}H_{\omega_i}+A_i^{\pi^0}F_{\phi_i})=0, \tag{4.20}$$

$$\sqrt{2}h_{V_i}f_{V_i}-\sigma_{V_i}f_{V_i}^2=0, \qquad i=1,..,n \tag{4.21}$$

$$-\frac{N_c}{4\pi^2}(\frac{5}{3}C_q-\frac{\sqrt{2}}{3}C_s)+4\sqrt{2}\sum_{i=1}^{n}h_{V_i}f_{V_i}\Big[$$
$$(3C_q+\frac{1}{3}F_{\omega_i}C_q-\frac{2\sqrt{2}}{3}C_sF_{\phi_i})+(\frac{5}{3}C_q-\frac{\sqrt{2}}{3}C_s)A_i^{\eta}F_{\phi_i}\Big]=0\,, \quad (4.22)$$

$$-\frac{N_c}{4\pi^2}(\frac{5}{3}C'_q+\frac{\sqrt{2}}{3}C'_s)+4\sqrt{2}\sum_{i=1}^{n}h_{V_i}f_{V_i}\Big[$$
$$(3C'_q+\frac{1}{3}F_{\omega_i}C'_q+\frac{2\sqrt{2}}{3}C'_sF_{\phi_i})+(\frac{5}{3}C'_q+\frac{\sqrt{2}}{3}C'_s)A_i^{\eta'}F_{\phi_i}\Big]=0\,. \quad (4.23)$$

Six parameters has been chosen $\sigma_{V_i}f_{V_i}^2$ $(i=1,2,3)$, $h_{V_3}f_{V_3}$, A_2^{η} and $A_2^{\eta'}$ to be determined using the asymptotic relations. The remaining parameters have been fitted to the experimental data. The Lagrangian approach allows also to extract the amplitudes, which involve vector-pseudoscalar-photon couplings. The $V-P-\gamma^*$ amplitudes have the following form:

$$\mathcal{M}[V(P)\to P(V)(q_1)\,\gamma^*(q_2)]=e\epsilon_{\mu\nu\beta\alpha}q_1^{\nu}q_2^{\alpha}F_{VP\gamma^*}(t_1)\epsilon_V^{\mu}\epsilon_{\gamma}^{\beta},$$

where ϵ_V^{μ} and $\epsilon_{\gamma}^{\beta}$ are the polarization vectors of the vector meson and the photon, and $t_1=q_2^2$ and the form factor $F_{VP\gamma^*}(t_1)$ for the observables used in the fit have the following form:

$$F_{\rho\pi^0\gamma^*}(t_1)=\frac{4\sqrt{2}h_{V_1}}{3f_{\pi}}\Big\{1-t_1D_{\omega_1}(t_1)\Big\}\,, \quad (4.24)$$

$$\begin{aligned}F_{\omega\pi^0\gamma^*}(t_1) &= \frac{4\sqrt{2}h_{V_1}}{f_{\pi}}\Big\{H_{\omega_1}-\frac{t_1}{F_{\omega_1}}\Big[D_{\rho_1}(t_1)+\Big(H_{\omega_1}F_{\omega_1}-1-A_{\phi\omega,1}^{\pi^0}\Big)\\ &\quad D_{\omega_1}(t_1)+A_{\phi\omega,1}^{\pi^0}D_{\phi_1}(t_1)\Big]\Big\}\,, \quad (4.25)\end{aligned}$$

$$\begin{aligned}F_{\phi\pi^0\gamma^*}(t_1) &= \frac{-4h_{V_1}}{f_{\pi}}\Big\{A_1^{\pi^0}-\frac{A_{\phi\omega,1}^{\pi^0}}{F_{\phi_1}}t_1D_{\omega_1}(t_1)\\ &\quad -\Big(A_1^{\pi^0}-\frac{A_{\phi\omega,1}^{\pi^0}}{F_{\phi_1}}\Big)t_1D_{\phi_1}(t_1)\Big\}\,, \quad (4.26)\end{aligned}$$

$$F_{\rho\eta\gamma^*}(t_1)=\frac{4\sqrt{2}h_{V_1}C_q}{f_{\pi}}\Big\{1-t_1D_{\rho_1}(t_1)\Big\}, \quad (4.27)$$

$$F_{\omega\eta\gamma^*}(t_1) = \frac{4\sqrt{2}h_{V_1}}{3f_\pi}\Big\{C_q\Big(1-t_1D_{\omega_1}(t_1)\Big)+\frac{18A^\eta_{\phi\omega,1}t_1}{F_{\omega_1}} \Big(D_{\omega_1}(t_1)-D_{\phi_1}(t_1)\Big)\Big\}, \quad (4.28)$$

$$F_{\phi\eta\gamma^*}(t_1) = \frac{4\sqrt{2}h_{V_1}}{3f_\pi}\Bigg\{\Big[2C_s-\Big(\frac{5}{\sqrt{2}}C_q-C_s\Big)A_1^\eta\Big]\Big[1-t_1D_{\phi_1}(t_1)\Big] +\frac{9\sqrt{2}A^\eta_{\phi\omega,1}}{F_{\phi_1}}\Big[t_1D_{\omega_1}(t_1)-t_1D_{\phi_1}(t_1)\Big]\Bigg\}, \quad (4.29)$$

$$F_{\rho\eta'\gamma^*}(t_1) = \frac{4\sqrt{2}h_{V_1}C'_q}{f_\pi}\Big\{1-t_1D_{\rho_1}(t_1)\Big\}, \quad (4.30)$$

$$F_{\omega\eta'\gamma^*}(t_1) = \frac{4\sqrt{2}h_{V_1}C'_q}{3f_\pi}\Big\{1-t_1D_{\omega_1}(t_1)\Big\} \quad (4.31)$$

$$F_{\phi\eta'\gamma^*}(t_1) = \frac{4\sqrt{2}h_{V_1}}{3f_\pi}\Big[-2C'_s-\Big(\frac{5}{\sqrt{2}}C'_q+C'_s\Big)A_1^{\eta'}\Big]\Big[1-t_1D_{\phi_1}(t_1)\Big]. \quad (4.32)$$

4.2.2 The determination of the model parameters

The free parameters of the model were fitted to all available experimental data, which can be described in terms of the interaction Lagrangians from Eq.(4.1-4.12). The data in the space-like region consist of measurements of the transition form factors for π^0, η, η' performed by BELLE [76], CELLO [77], and CLEO [78] experiments and the measurements of the η, η' transition form factors done by BABAR [79]. The data in the time-like region include the following list of observables:

- $e^+e^- \to \pi^0(\eta,\eta')\gamma$ cross section measured by SND [80, 81], CMD2 [82] and BABAR [83] experiments.
- time-like form factor $F_{\gamma^*\gamma\pi^0}$ measured by A2 experiment in the decay $\pi^0 \to \gamma e^+e^-$ [84].
- time-like form factor $F_{\gamma^*\gamma\eta}$ measured by A2 experiment in the decay $\eta \to \gamma e^+e^-$ [85].

- time-like form factor $F_{\gamma^*\gamma\eta'}$ measured BES-III experiment by in the decay $\eta' \to \gamma e^+ e^-$ [86].
- time-like form factor $F_{\omega\pi^0\gamma^*}$ measured by A2 experiment in the decay $\omega \to \pi^0 e^+ e^-$ [85].
- time-like form factor $F_{\phi\pi^0\gamma^*}$ measured by KLOE-2 experiment in the decay $\phi \to \pi^0 e^+ e^-$ [87].
- time-like form factor $F_{\phi\eta\gamma^*}$ measured by KLOE-2 experiment in the decay $\phi \to \eta e^+ e^-$ [88].
- differential partial decay width of $\eta \to \pi^0\gamma\gamma$ measured by A2 experiment [89].
- two-body partial widths [90] of $P \to \gamma\gamma$ $V \to e^+e^-$ $(V = \rho, \omega, \phi)$, $V \to \pi^0\gamma$, $V \to \eta\gamma$, $\phi \to \eta'\gamma$, $\eta' \to \rho\gamma$ and $\eta' \to \omega\gamma$.

The formula for the $e^+e^- \to P\gamma$ cross section used in the fit, where P denotes π^0, η or η' has the following form

$$\begin{aligned}\sigma_{e^+e^-\to P\gamma}(s) = \quad & \frac{(4\pi\alpha)^3}{24\pi s}\Big(1-\frac{m_P^2}{s}\Big)\Big(\frac{s-m_P^2}{2\sqrt{s}}\Big)^2 \\ & \cdot|F_{\gamma\gamma^*P}(0,s)|^2\,, \end{aligned} \tag{4.33}$$

where m_P is the mass of a pseudoscalar and s is the Mandelstam variable. The differential decay width $\eta \to \pi^0\gamma\gamma$ within adopted model is given by the following formula:

$$\begin{aligned} d\Gamma\Big(\eta(q) \;\to\; & \pi^0(p)\gamma(k_1)\gamma(k_2)\Big) = \\ & \frac{1}{4m_\eta}|M|^2 dLips_3(q;p,k_1,k_2)\,, \end{aligned} \tag{4.34}$$

with the amplitude given by

$$\begin{aligned} M \;=\; & \sum_{i,V}\left(\frac{4\sqrt{2}eh_{V_i}}{3f_\pi}\right)^2 \epsilon_{\mu\nu\alpha\beta}q^\nu k_1^\alpha \epsilon^\beta(k_1) g^{\mu\delta} \\ & D_{V_i}((p+k_2)^2)\epsilon_{\delta\sigma\delta'\sigma'}p^\sigma k_2^{\delta'}\epsilon^{\sigma'}(k_2)B_{V_i} \\ & +\Big(k_1 \leftrightarrow k_2\Big)\,, \end{aligned} \tag{4.35}$$

where $B_{\phi_i} = -\frac{3}{\sqrt{2}}A_i^{\pi^0}[2C_s - (\frac{5}{\sqrt{2}}C_q - C_s)A_i^\eta]$, $B_{\rho_i} = 3C_q$, $B_{\omega_i} = 3H_{\omega_i}C_q$ and D_{V_i} is defined in Eq. (4.18).

The 2-body partial decay widths in the adopted model are expressed as

$$\Gamma(P \to \gamma\gamma) = \frac{m_P^3 \pi \alpha^2}{4} |F_{P\gamma^*\gamma^*}(0,0)|^2, \tag{4.36}$$

$$\Gamma(\rho \to e^+e^-) = \frac{4\pi\alpha^2 M_\rho f_{V_1}^2}{3}, \tag{4.37}$$

$$\Gamma(\omega \to e^+e^-) = \frac{4\pi\alpha^2 M_\omega f_{V_1}^2 F_{\omega_1}^2}{27}, \tag{4.38}$$

$$\Gamma(\phi \to e^+e^-) = \frac{8\pi\alpha^2 M_\phi f_{V_1}^2 F_{\phi_1}^2}{27}, \tag{4.39}$$

$$\Gamma(P \to V\gamma) = \frac{\alpha}{8} m_P^3 k_V^3 |F_{VP\gamma^*}(0)|^2, \tag{4.40}$$

$$\Gamma(V \to P\gamma) = \frac{\alpha}{24} M_V^3 k_P^3 |F_{VP\gamma^*}(0)|^2, \tag{4.41}$$

where $k_V = (1 - \frac{m_P^2}{M_V^2})$, $k_P = (1 - \frac{M_V^2}{m_P^2})$.

The model parameters have been fitted to the experimental data using the MINUIT package [48]. Two fits have been performed to extract the model parameters. In the first fit (fit1) the parameters θ_8, θ_0, f_8, f_0 and f_π, which describe the η- η' mixing and the $\pi^0 \to \gamma\gamma$ decay have been fixed to the following values:

$$\begin{aligned} f_\pi = \quad & 0.092388\ GeV, \quad f_0 = 0.11697\ GeV, \quad f_8 = 0.10623\ GeV, \\ & \theta_0 = -0.14471, \qquad\qquad \theta_0 = -0.36516. \end{aligned} \tag{4.42}$$

The values of this parameters differ slightly from the ones presented in [65]. Since the precision of the measurement of $P \to \gamma\gamma$ decay widths ($P = \pi^0$, η, η') were improved, the values of this parameters have been extracted from the new data [90]. In the second fit (fit2) all parameters of the model have been fitted to the experimental data. In Tables 4.1 and 4.2 the values of the χ^2 for all experiments are given for the fit1 and the fit2 respectively.

The data from the BABAR measurement of the pion transition form factor in the space-like region [91] has been excluded from both fits and similarly the NA60 data [92] for the measurement of the η transition form factor and the $F_{\omega\pi^0\gamma^*}$ form factor. All this measurements are in contradiction with other experimental data, what can be observed on the plots from Fig. 4.2, 4.6 and 4.8. The smallest tension is between the η transition form factor measurements of A2 [85] and NA60 [92] (see Figure 4.6) and in fact the data

Experiment	nep	χ^2,fit 1	Experiment	nep	χ^2,fit 1
space-like form-factors					
BELLE (π^0) [76]	15	9.96	CLEO98(η) [78]	19	15.8
CELLO91(π^0) [77]	5	0.34	BaBar(η') [79]	11	5.4
CLEO98(π^0) [78]	15	10.6	CELLO91(η') [77]	5	0.73
BaBar(η) [79]	11	7.34	CLEO98(η') [78]	29	25.1
CELLO91(η) [77]	4	0.16			
e^+e^- cross sections					
CMD2($\pi^0\gamma$) [82]	46	54.1	SND($\eta\gamma$) [80]	78	68.7
SND($\pi^0\gamma$) [81]	62	65.5	BaBar($\eta\gamma, \eta'\gamma$) [83]	2	0.18
CMD2 ($\eta\gamma$) [82]	42	25.4			
3-body decays					
A2($\pi^0 \to \gamma e^+e^-$) [84]	18	0.32	A2($\omega \to \pi^0 e^+e^-$) [85]	14	2.14
A2($\eta \to \gamma e^+e^-$) [85]	34	10.2	KLOE-2($\phi \to \pi^0 e^+e^-$) [87]	15	4.33
A2 ($\eta \to \pi^0\gamma\gamma$) [89]	7	26.6	KLOE-2($\phi \to \eta e^+e^-$) [88]	92	95.1
BES-III($\eta' \to \gamma e^+e^-$) [86]	8	2.39			
2-body decays					
$\Gamma(\pi^0 \to \gamma\gamma)$ [90]	1	0.36	$\Gamma(\rho \to \pi^0\gamma)$ [90]	1	1.17
$\Gamma(\eta \to \gamma\gamma)$ [90]	1	0.78	$\Gamma(\omega \to \pi^0\gamma)$ [90]	1	4.08
$\Gamma(\eta' \to \gamma\gamma)$ [90]	1	1.05	$\Gamma(\phi \to \pi^0\gamma)$ [90]	1	0.08
$\Gamma(\eta' \to \rho\gamma)$ [90]	1	3.0	$\Gamma(\rho \to \eta\gamma)$ [90]	1	3.32
$\Gamma(\eta' \to \omega\gamma)$ [90]	1	0.00	$\Gamma(\omega \to \eta\gamma)$ [90]	1	6.86
$\Gamma(\rho \to e^+e^-)$ [90]	1	0.23	$\Gamma(\phi \to \eta\gamma)$ [90]	1	1.63
$\Gamma(\omega \to e^+e^-)$ [90]	1	0.56	$\Gamma(\phi \to \eta'\gamma)$ [90]	1	0.01
$\Gamma(\phi \to e^+e^-)$ [90]	1	0.69			
Total				536	454

Table 4.1: The values of the χ^2 for the experiments used in the fits described in the text. 'nep' means number of experimental points. Number of free parameters in the fit is equal to 17.

are consistent within the experimental error bars. Yet, within the model, which is presented here, there is no way to fit simultaneously SND [80] data on $e^+e^- \to \eta\gamma$ cross section, the differential width ($\eta \to \pi^0\gamma\gamma$) measured by A2 [89] and the partial widths $V \to \eta\gamma$ [90] together with the NA60 measurements [92] of the η transition form factor in the time-like region.

In Table 4.3 the parameters obtained in fit1 and fit2 are presented. As one can observe the fit is much better, when one allows to change of the $\eta - \eta'$ mixing parameters, which is obvious since the number of degrees of freedom is in that case smaller. The fit2 is the way for a model dependent extraction of the $\eta - \eta'$ mixing parameters.

Experiment	nep	χ^2,fit 2	Experiment	nep	χ^2,fit 2
space-like form-factors					
BELLE (π^0) [76]	15	6.72	CLEO98(η) [78]	19	15.5
CELLO91(π^0) [77]	5	0.24	BaBar(η') [79]	11	3.70
CLEO98(π^0) [78]	15	6.82	CELLO91(η') [77]	5	0.56
BaBar(η) [79]	11	7.5	CLEO98(η') [78]	29	24.4
CELLO91(η) [77]	4	0.16			
e^+e^- cross sections					
CMD2($\pi^0\gamma$) [82]	46	54.1	SND($\eta\gamma$) [80]	78	59.8
SND($\pi^0\gamma$) [81]	62	54.2	BaBar($\eta\gamma, \eta'\gamma$) [83]	2	1.57
CMD2 ($\eta\gamma$) [82]	42	25.6			
3-body decays					
A2($\pi^0 \to \gamma e^+e^-$) [84]	18	0.34	A2($\omega \to \pi^0 e^+e^-$) [85]	14	2.12
A2($\eta \to \gamma e^+e^-$) [85]	34	11.1	KLOE-2($\phi \to \pi^0 e^+e^-$) [87]	15	4.33
A2 ($\eta \to \pi^0\gamma\gamma$) [89]	7	19.5	KLOE-2($\phi \to \eta e^+e^-$) [88]	92	95.1
BES-III($\eta' \to \gamma e^+e^-$) [86]	8	2.13			
2-body decays					
$\Gamma(\pi^0 \to \gamma\gamma)$ [90]	1	0.1	$\Gamma(\rho \to \pi^0\gamma)$ [90]	1	0.42
$\Gamma(\eta \to \gamma\gamma)$ [90]	1	2.73	$\Gamma(\omega \to \pi^0\gamma)$ [90]	1	1.56
$\Gamma(\eta' \to \gamma\gamma)$ [90]	1	0.44	$\Gamma(\phi \to \pi^0\gamma)$ [90]	1	0.06
$\Gamma(\eta' \to \rho\gamma)$ [90]	1	0.77	$\Gamma(\rho \to \eta\gamma)$ [90]	1	6.8
$\Gamma(\eta' \to \omega\gamma)$ [90]	1	0.54	$\Gamma(\omega \to \eta\gamma)$ [90]	1	3.04
$\Gamma(\rho \to e^+e^-)$ [90]	1	0.05	$\Gamma(\phi \to \eta\gamma)$ [90]	1	1.17
$\Gamma(\omega \to e^+e^-)$ [90]	1	0.73	$\Gamma(\phi \to \eta'\gamma)$ [90]	1	0.00
$\Gamma(\phi \to e^+e^-)$ [90]	1	0.46			
Total				536	415

Table 4.2: The values of the χ^2 for the experiments used in the fits described in the text. 'nep' means number of experimental points. Number of free parameters in the fit is equal to 22.

The comparison of the data with the fit results are presented on the following plots:

- In Fig. 4.2 the pseudoscalar transition form factors in the space-like region are presented. The old fit refers to the two-octet model described in [65], which was consistent only with the space-like data. The asymptotic values of the form factors are marked by the horizontal lines on the right side of the plots. The 'fit' value refers to the value for the current model and B-L to the Brodsky-Lepage high energy limit predicted by perturbative QCD. This limit is given by $2f_\pi$ for pion form factor, $2f_\eta = 2f_\pi/(\frac{5}{3}C_q - \frac{\sqrt{2}}{3}C_s)$ for η form factor and $2f_{\eta'} = 2f_\pi/(\frac{5}{3}C'_q + \frac{\sqrt{2}}{3}C'_s)$

Parameter	fit 1	fit 2
h_{V_1}	0.0335(2)	0.0377(8)
f_{V_1}	0.2022(8)	0.2020(8)
$f_{V_2}h_{V_2}$	-0.0013(2)	-0.0010(4)
h_{V_2}	0.00184(5)	0.0002(1)
h_{V_3}	-0.485(7)	-0.30(4)
H_{ω_1}	1.160(11)	1.02(3)
F_{ω_1}	0.881(8)	0.88(1)
F_{ϕ_1}	0.783(5)	0.783(5)
$A_1^{\pi^0}$	-0.094(1)	-0.083(2)
$A_2^{\pi^0}$	-12.04(16)	-15(6)
$A_3^{\pi^0}$	0.08(3)	-0.16(7)
A_1^{η}	-0.041(4)	-0.30(4)
A_3^{η}	0.23(6)	-0.06(8)
$A_1^{\eta'}$	-0.039(7)	-0.21(5)
$A_3^{\eta'}$	-0.27(3)	-0.56(6)
$A_{\phi\omega,1}^{\pi^0}$	-0.23(4)	-0.21(4)
$A_{\phi\omega,1}^{\eta}$	-0.031(8)	-0.028(7)
f_π	0.09239(fixed)	0.09266(8)
f_0	0.117(fixed)	0.095(2)
f_8	0.11(fixed)	0.17(1)
θ_0	-0.14(fixed)	-0.54(12)
θ_8	-0.365(fixed)	-0.446(17)

Table 4.3: The model parameters obtained in the fits. The errors, given in brackets, are the parabolic errors calculated by procedure Minos of the MINUIT package [48]

for the η' form factor.

- In Figures 4.3 and 4.4 the cross sections $\sigma(e^+e^- \to P\gamma)$ for $P = \pi^0$, η are presented.
- In Figures 4.5, 4.6 and 4.7 the π^0, η and η' transition form factors in the time-like region are presented.
- In Figure 4.8 the form factor $\omega\pi^0\gamma$ in the time-like region is presented.
- In Figures 4.9 and 4.10 the form factor $\phi\pi^0\gamma$ $\phi\eta\gamma$ in the time-like region are presented.

- In Figure 4.11 the differential partial width of the decay $\eta \to \pi^0\gamma\gamma$ is presented.

The plots with the comparison of the experimental data with the model fit results are shown only for fit2. The results obtained for fit1 are very similar and do not introduce new insight into this subject.

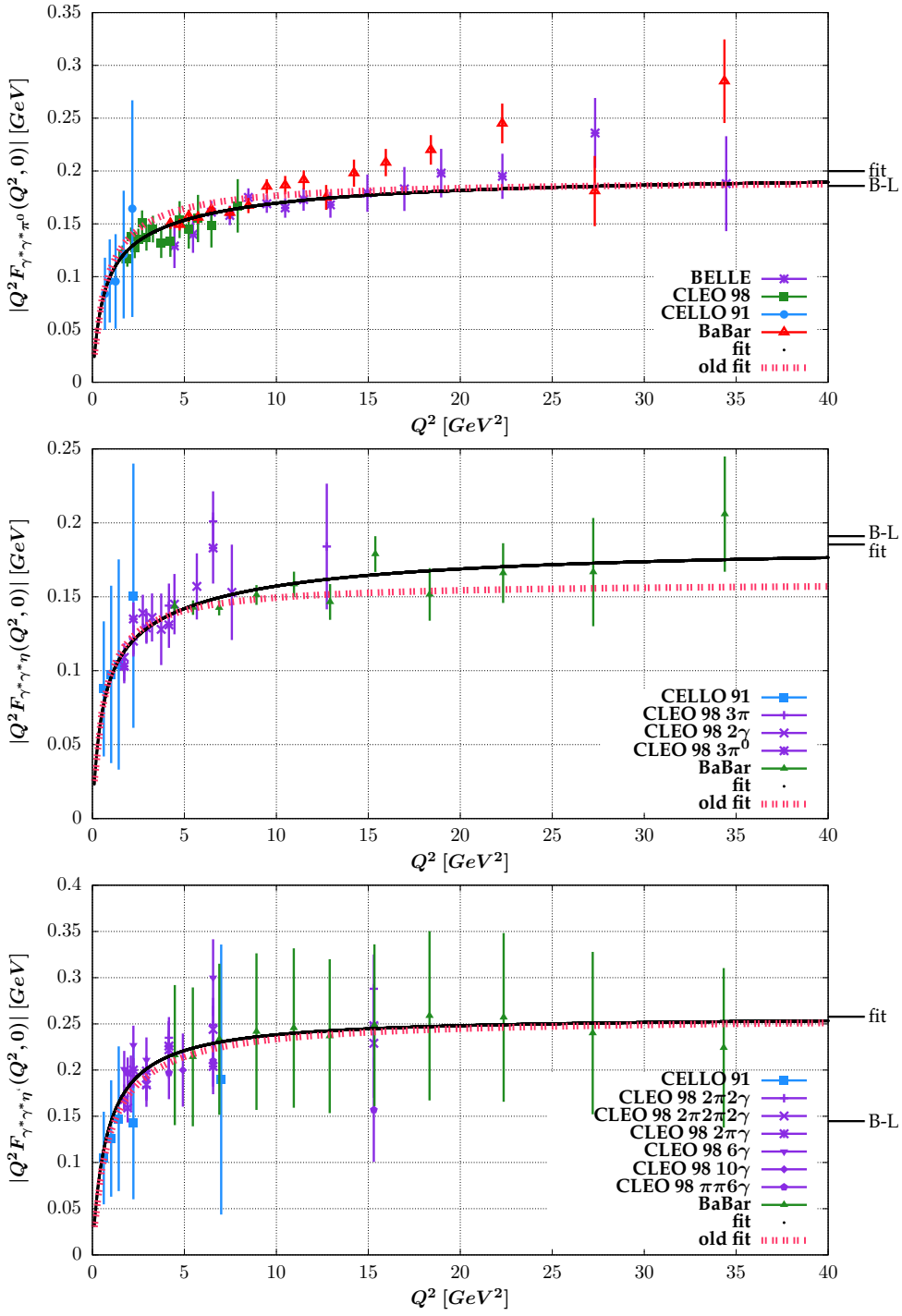

Figure 4.2: The transition form factors $\gamma^*\gamma P$ in the space-like region compared to the data [76–78, 83, 91].

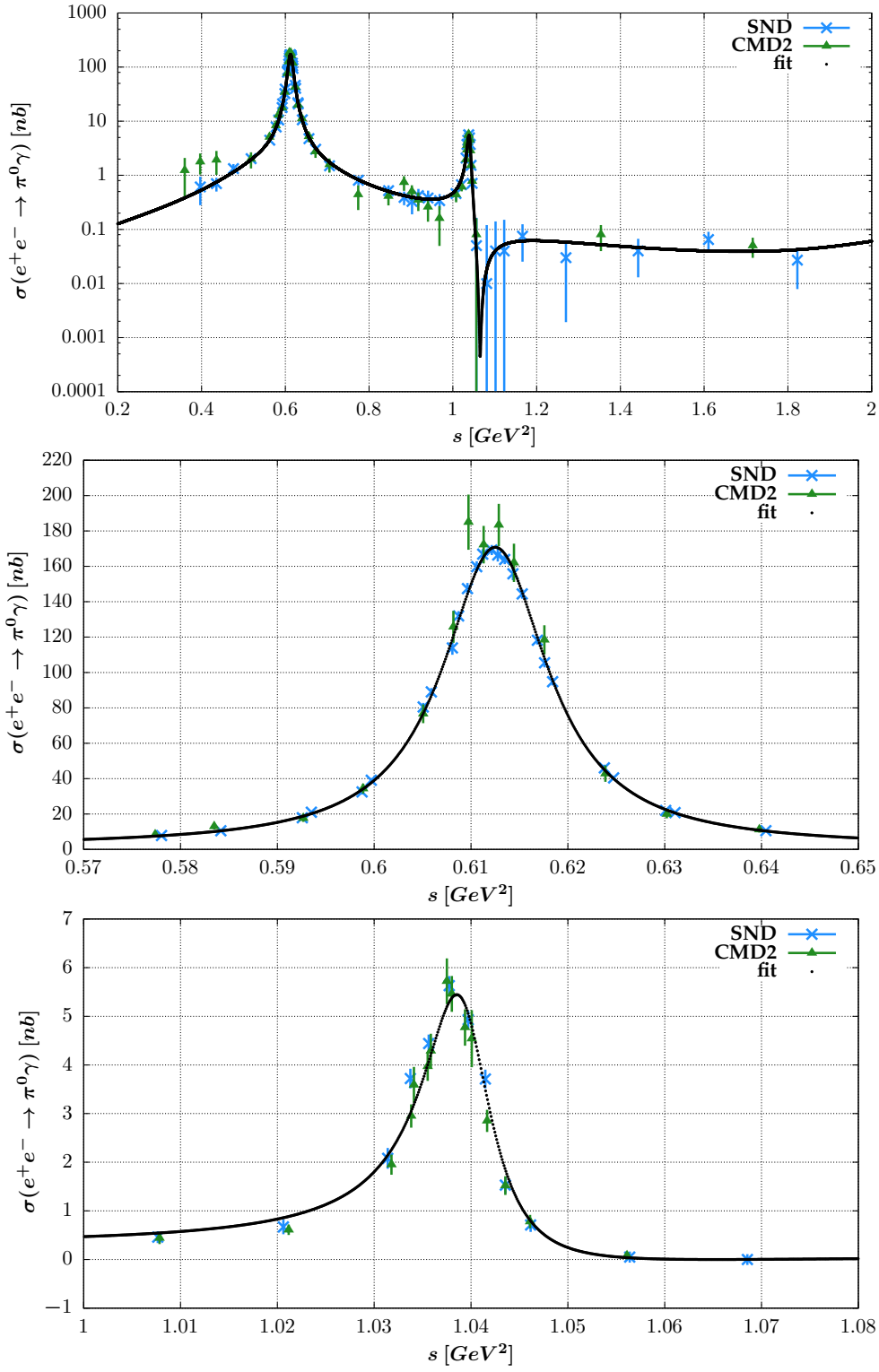

Figure 4.3: The experimental data for $\sigma(e^+e^- \to \pi^0\gamma)$ compared to the model predictions [81, 82].

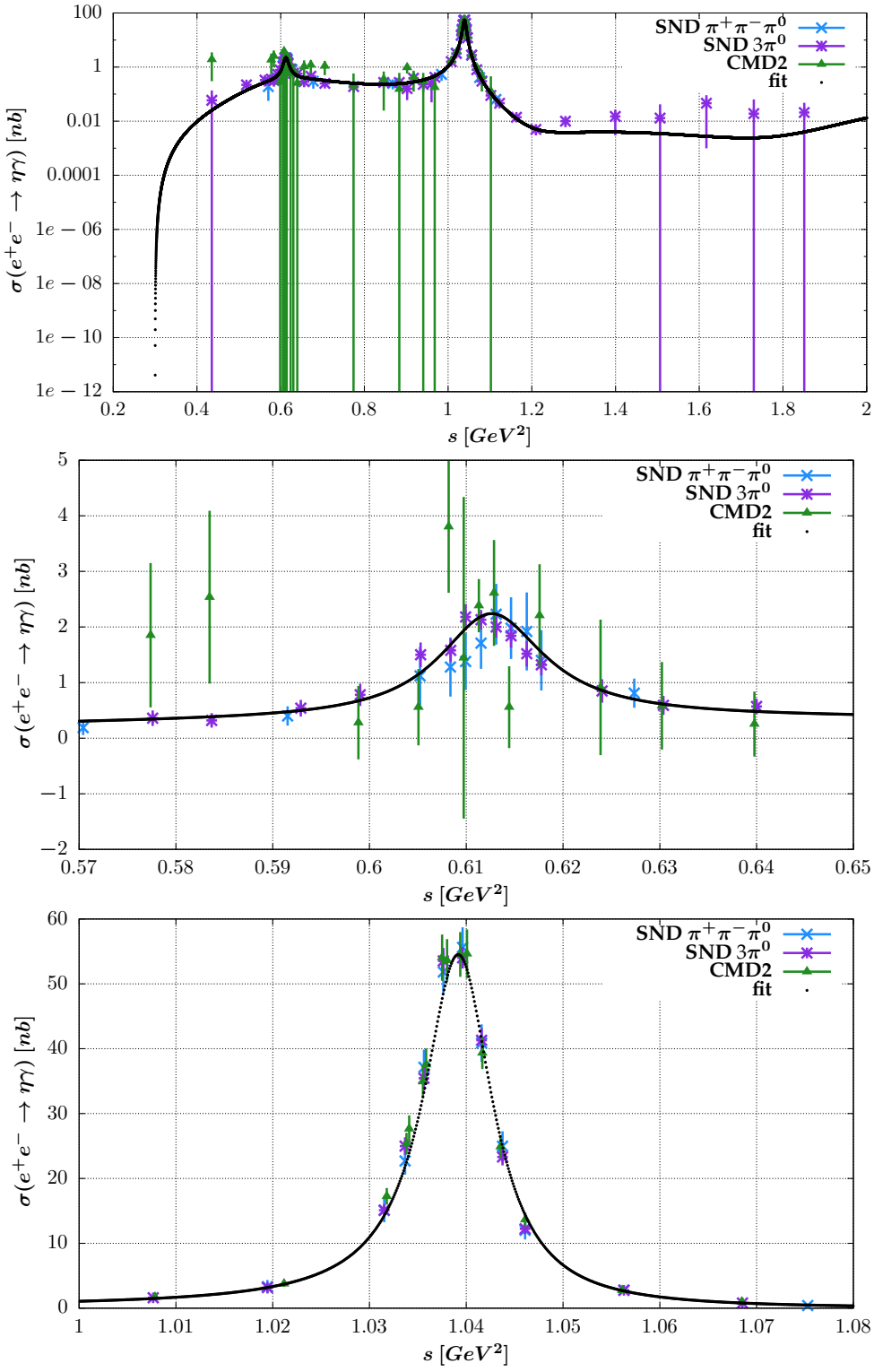

Figure 4.4: The experimental data for $\sigma(e^+e^- \to \eta\gamma)$ compared to the model predictions [80, 82].

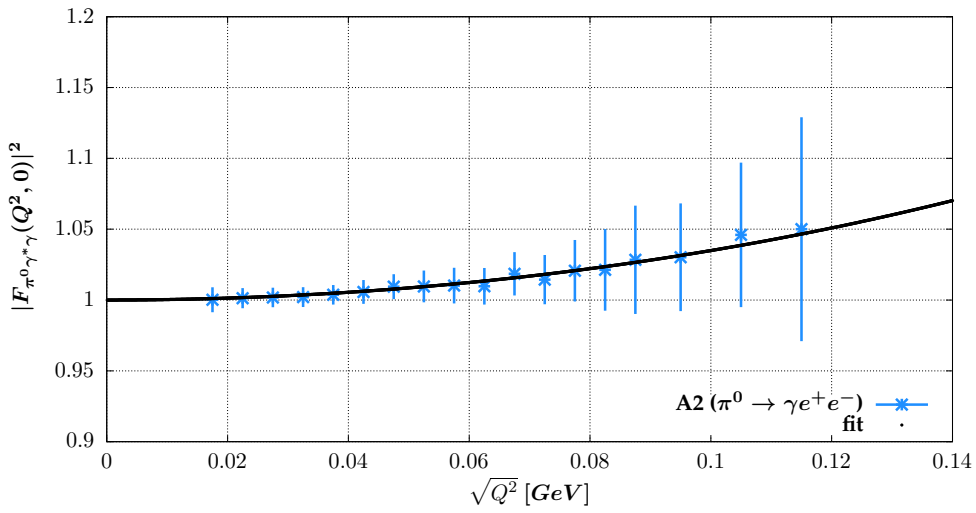

Figure 4.5: The transition form factor $\gamma^*\gamma\pi^0$ in the time-like region compared to the data [84].

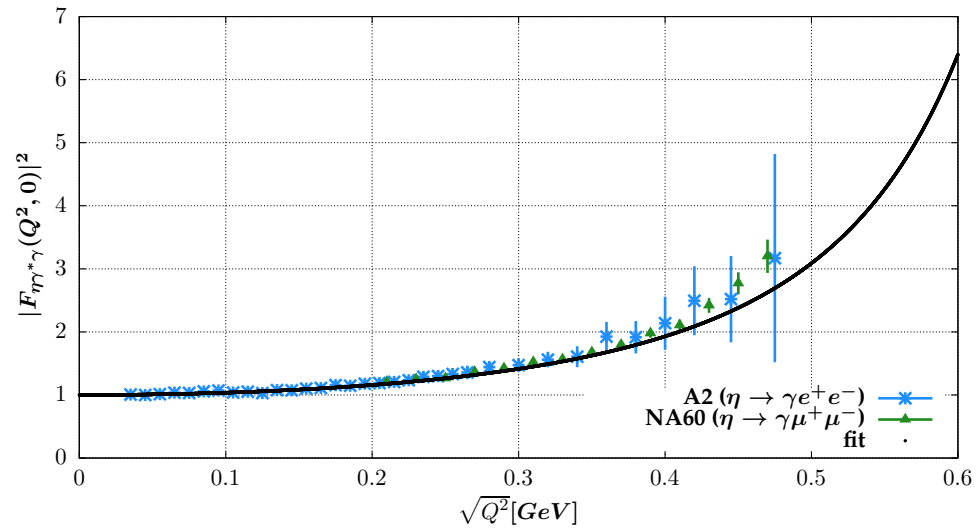

Figure 4.6: The transition form factor $\gamma^*\gamma\eta$ in the time-like region compared to the data [85].

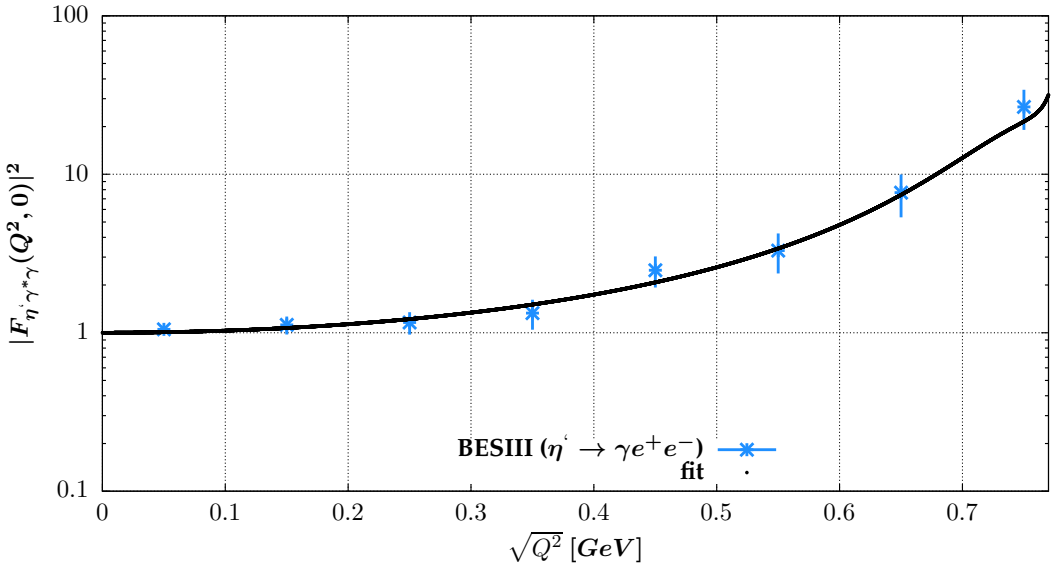

Figure 4.7: The transition form factor $\gamma^*\gamma\eta'$ in the time-like region compared to the data [86].

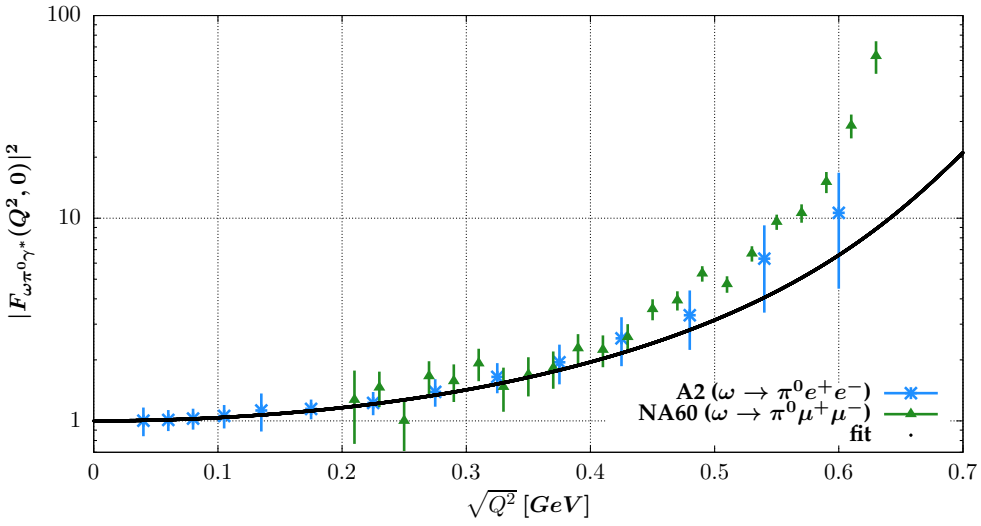

Figure 4.8: The form factor $\omega\pi^0\gamma$ in the time-like region compared to the data [85].

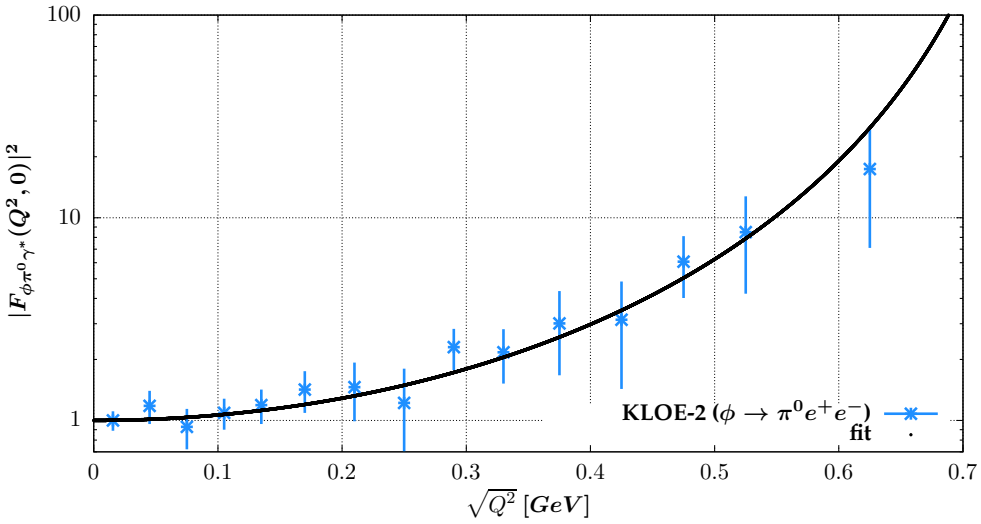

Figure 4.9: The form factor $\phi\pi^0\gamma$ in the time-like region compared to the data [87].

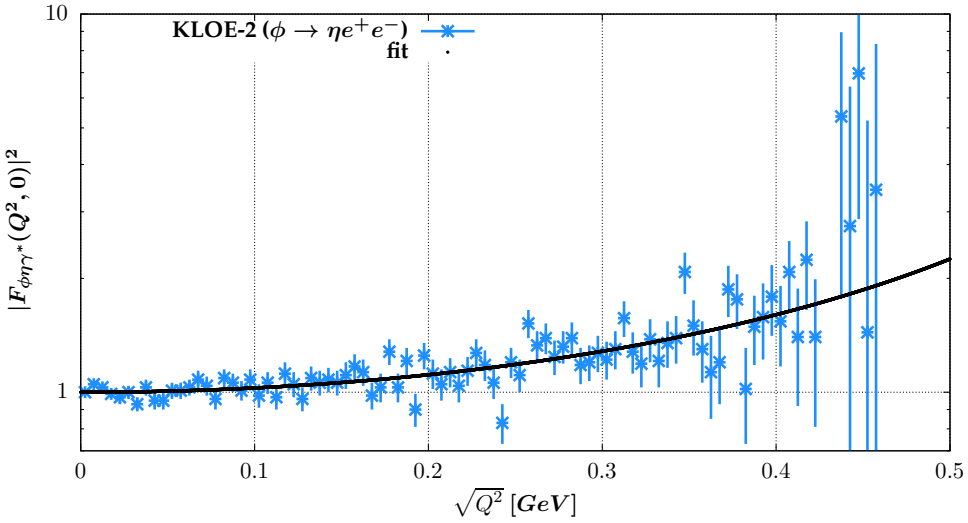

Figure 4.10: The form factor $\phi\eta\gamma$ in the time-like region compared to the data [88].

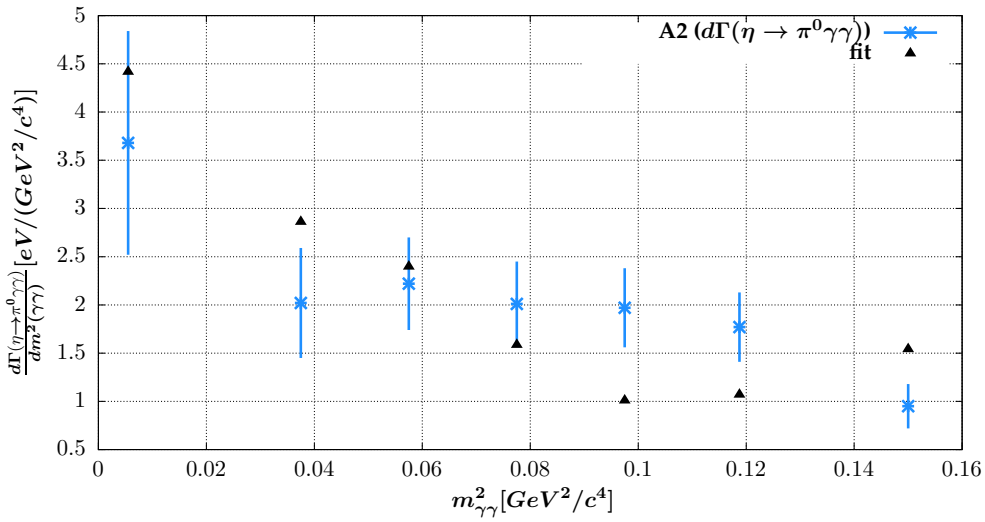

Figure 4.11: The differential partial width of the decay $\eta \to \pi^0\gamma\gamma$ compared to the data [89].

4.3 The modeling and the simulation of the reaction $e^+e^- \to P\gamma(\gamma)$

4.3.1 Amplitudes describing the reaction $e^+e^- \to P\gamma(\gamma)$

The new model of the pseudoscalar transition form factors, presented in the previous section, has been used in PHOKHARA (PHOKHARA 9.3) Monte Carlo generator to make predictions for the cross section $e^+e^- \to P\gamma(\gamma)$, $P = \pi^0$, η, η'. This reaction can be simulated in the scan mode, where the invariant mass of the $P\gamma$ is fixed at the leading order (LO) and the radiative return mode, where invariant mass of the final particles depends on the energy of photon(s) emitted from the initial states. Fig. 4.12 shows the diagrams taken into account in the calculations. The scan mode can be simulated at the next-to-leading order (NLO), while the radiative return mode at the LO only. The diagram from Fig. 4.12a is the LO amplitude for the scan mode. The diagram from Fig. 4.12b represents the virtual contributions at the NLO and the diagram from Fig. 4.12c is the NLO (LO) amplitude for the initial state radiation in the scan (radiative return) mode. The photon phase space was divided into soft and hard part. The soft part was added analytically to the virtual part.

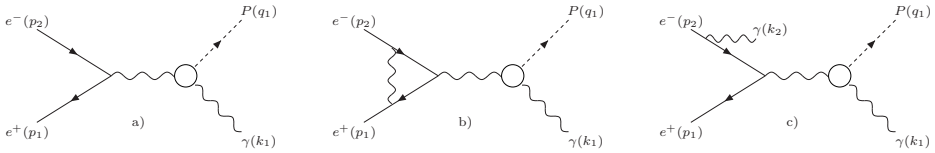

Figure 4.12: Diagrams for the reaction $e^+e^- \to P\gamma(\gamma)$. The blob indicates that the $\gamma^*\gamma P$ coupling is modeled testing the form factor.

The next-to-leading order (NLO) cross section for the scan mode is given by the following formula:

$$\sigma_{NLO} = \sigma_{1\gamma}(1 + \Delta_{soft,virt,1ph}) + \sigma_{2\gamma}, \tag{4.43}$$

where $\sigma_{1\gamma}$ is implemented in terms of leptonic ($L_{\mu\nu}$) and hadronic ($H_{\mu\nu}$) tensors. It is given by the following formula [51]:

$$\sigma_{1\gamma} = \frac{1}{2s} L^0_{\mu\nu} H^{\mu\nu} d\Phi_2(s, q_1, k_1), \tag{4.44}$$

where s is the Mandelstam variable and $d\Phi_2(s, q_1, k_1)$ is the two particle phase

space. The leptonic and hadronic tensors have the following form:

$$L^0_{\mu\nu} = 16\pi\alpha\Big(p_{1\mu}p_{2\nu} - g_{\mu\nu}\frac{s}{2} + p_{1\nu}p_{2\mu}\Big), \tag{4.45}$$

$$H_{\mu\nu} = 16\pi^2\alpha^2|F_{\gamma^*\gamma P}(s,0)|^2\Big(g_{\mu\nu}(k_1.q_1)^2 + k_{1\mu}k_{1\nu}m_P^2 - k_{1\mu}q_{1\nu}k_1.q_1 - k_{1\nu}q_{1\mu}k_1.q_1\Big), \tag{4.46}$$

where m_P is the mass of the pseudoscalar meson of momentum q_1 and p_1, p_2, k_1 are momenta of positron, electron and photon respectively. The soft and virtual corrections have the following form [51]

$$\Delta_{soft,virt,1ph} = \frac{2\alpha}{\pi}\Big(\log(2w)(\log(s/m_e^2) - 1) + 3\log(s/m_e^2) - 1 + \zeta_2\Big), \tag{4.47}$$

where $w = E_\gamma^{max}/\sqrt{s}$ is the soft photon cutoff, $s = (p_1 + p_2)^2$, E_γ^{max} is the maximal energy of the soft photon in the e^+e^- CMS frame. The cross section $\sigma_{2\gamma}$ written in terms of the invariant amplitude $\mathcal{M}$ is given by the following formula:

$$\sigma_{2\gamma} = \frac{1}{2s}\Big|\mathcal{M}\Big(e^+(p_1)e^-(p_2) \to \pi^0(q_1)\gamma(k_1)\gamma(k_2)\Big)\Big|^2 d\Phi_3(s, k_2, q_1, k_1), \tag{4.48}$$

where $d\Phi_3(s, q_1, k_1, k_2)$ is the infinitesimal element of the 3-body phase space. For the square of the amplitude with two photons in the final state it is convenient to write it in terms of leptonic and hadronic currents:

$$\Big|\mathcal{M}(e^+(p_1)e^-(p_2) \to \pi^0(q_1)\gamma(k_1)\gamma(k_2))\Big|^2 = L^\nu(k_1)H_\nu(k_2) + (k_1 \leftrightarrow k_2), \tag{4.49}$$

with

$$H_\nu(k_2) = e^2\epsilon_{\mu\nu\alpha\beta}q_1^\mu k_2^\alpha \epsilon_2^\beta F_{\gamma^*\gamma^* P}\Big((q_1 + k_2)^2, 0\Big) \tag{4.50}$$

and

$$L^\nu(k_1) = \frac{ie^2}{2p_2 \cdot k_1}\bar{v}(p_1)\gamma^\nu\Big(2\epsilon_1 p_1 - k_1\epsilon_1\Big)u(p_2) + \frac{ie^2}{2p_1 \cdot k_1}\bar{v}(p_1)\Big(\epsilon_1 k_1 - 2\epsilon_1 p_1\Big)\gamma^\nu u(p_2), \tag{4.51}$$

where $\epsilon_i, i = 1, 2$ are polarization vectors of the photons with the four momenta k_i.

4.3.2 The generation of the 3-body phase space

The 3-body phase space ($P\gamma\gamma$) can be written in the following form:

$$d\Phi_3(s, q_1, k_1, k_2) = \frac{1}{2\pi} dQ^2 d\Phi_2(s; Q, k_1)\Phi_2(Q; q_1, k_2). \tag{4.52}$$

The general form of the 2-body phase space is the following:

$$d\Phi_2(P_1, P_2, P_3) = \frac{1}{32\pi^2} \frac{\sqrt{\lambda(P_1^2, P_2^2, P_3^2)}}{P_1^2} d\cos(\theta_3) d\phi_3, \tag{4.53}$$

where θ_3 and ϕ_3 are polar and azimuthal angles of particle with momentum P_3 and

$$\lambda(x, y, z) = x^2 + y^2 + z^2 - 2xy - 2yz - 2zx. \tag{4.54}$$

For generation of the photons momenta the following procedure was used:

1. In the first step the 2-channel Monte Carlo is used to generate $Q_1^2 = (k_1+q_1)^2$ or $Q_2^2 = (k_2+q_1)^2$ with equal probability. For the generated invariant once again a multi-channel Monte Carlo is used to absorb peaks from the phase space regions into changes of variables. The function, which approximate the behavior in the Q_i^2 has the following form:

$$\begin{aligned} F_{approx} &= \Big(f_s(s - Q_i^2) + f_\omega\Big((Q_i^2 - M_\omega^2)^2 + M_\omega^2\Gamma_\omega^2\Big) \\ &\quad + f_\phi\Big((Q_i^2 - M_\phi^2)^2 + M_\phi^2\Gamma_\omega^2\Big) + f_f Q_i^2 \Big)^{-1}. \end{aligned} \tag{4.55}$$

   The following channels have been used:

   - The channel to absorb the soft photon emission peak with the following change of the variable:

$$y = f_s \log(s - Q_i^2). \tag{4.56}$$

   - Two channels to absorb ϕ and ω narrow resonances peaks with the following change of the variable:

$$y = f_V M_V \Gamma_V \operatorname{arc\,tg}\left(\frac{Q_i^2 - M_V^2}{M_V\Gamma_V}\right), \tag{4.57}$$

     where $V = \omega,\, \phi$.

   - channel with Q_i^2 generated linearly,

where f_i, for $i = s, \omega, \phi, f$, are constants, which values has been chosen to increase the efficiency of the Monte Carlo.

2. When Q_1^2 is generated the polar angle of the photon with momentum k_2 is generated in centre-of-mass system (CMS) of electron-positron, otherwise (when Q_2^2 is generated) the photon with momentum k_1 is generated in this frame of reference. For the photon generated in CMS frame of initial particles the following change of the variables [93] is used:
$$\cos\theta_i = \frac{1}{\beta}\,\mathrm{tgh}(\beta t_1), \tag{4.58}$$
where $\beta = \sqrt{1 - 4m_e^2/s}$. This change of the variables allows to absorb the peaks in the phase space, which comes from the photons collinear to electron and positron.

3. The polar angle of the second photon is generated flat in the rest frame of Q_i.

4. Azimuthal angles of both photons are generated flat. The cross section do not have any narrow peaks in domain of azimuthal angles.

5. The momentum of one of the photon is calculated in the CMS of initial particles.

6. The momentum of second photon is calculated in the rest frame of Q_i. Then the boost from $\vec{Q} = 0$ frame to CMS is performed.

4.4 Monte Carlo simulations

The newly developed model of two-photon transition form factors for pseudoscalar mesons, which is consistent with the data in the time-like region, allows to obtain reasonable predictions for the cross section of the reaction $e^+e^- \to P\gamma(\gamma)$ and to investigate the impact of the radiative corrections.

In the plots from Fig. 4.13 and 4.14 the leading order and the next-to-leading order cross sections are presented for two versions of the form factors model (fit1 and fit2). The cross sections were obtained for the event selection close to the one used in BES-III experiment:

- At least one photon has to be observed with the energy $E_\gamma > 0.5$ GeV.
- Observed photon and pseudoscalar meson are within the range of polar angles $20^o < \theta_{P,\gamma} < 160^o$.

As one can observe the radiative corrections are large. The reason is that the form factors fall rapidly with the increasing value of the scattering energy. In the leading order amplitude the form factor is always calculated at the invariant s, while in the case of the next-to-leading order amplitude, which involve two photons, the form factors calculated at $Q_1^2 = (q_1 + k_1)^2$ and $Q_2^2 = (q_1 + k_2)^2$ enter the amplitude. The big difference between the LO and NLO cross section is caused by the form factors calculated at values of $Q_{1,2}^2$ much smaller than s, which is a result of the hard photon emission.

The differences between versions of the form factors models from fit1 and fit2 are small up to energy 2 GeV, where the behavior of the form factors is well constrained by the experimental data. Above this energy, where no experimental measurements exist, the two versions of the form factors model differ a bit more. The difference is mostly observed in the size of the ϕ_3 meson resonance peak. The data from experimental measurements in the energy range above 2 GeV could verify the model predictions and allow to constraint better the high energy behavior of the two-photon-pseudoscalar form factors.

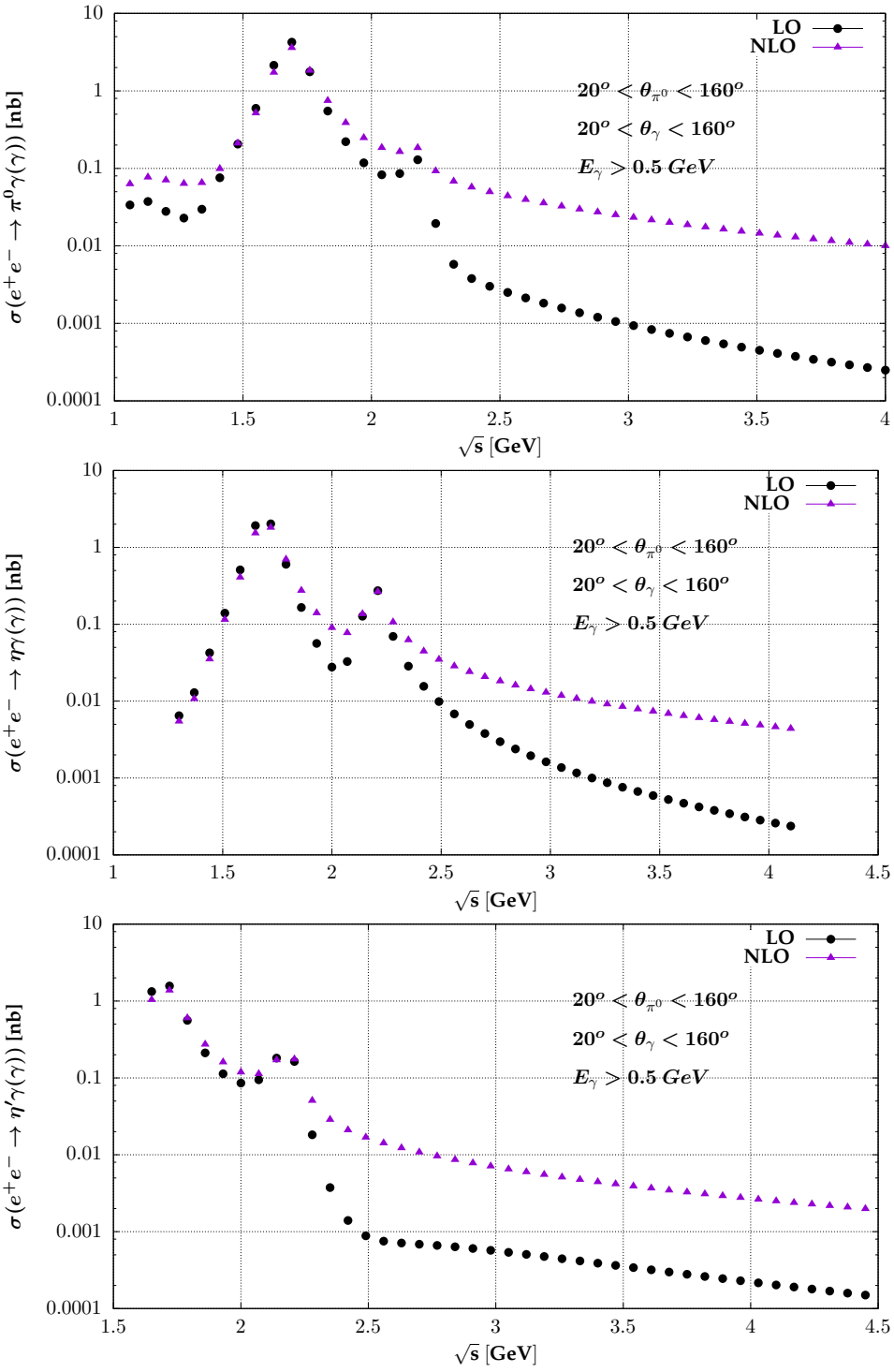

Figure 4.13: Comparison between LO and NLO cross sections for the reaction $e^+e^- \to P\gamma(\gamma)$. The comparison obtained for the form factors with the parameters from fit1.

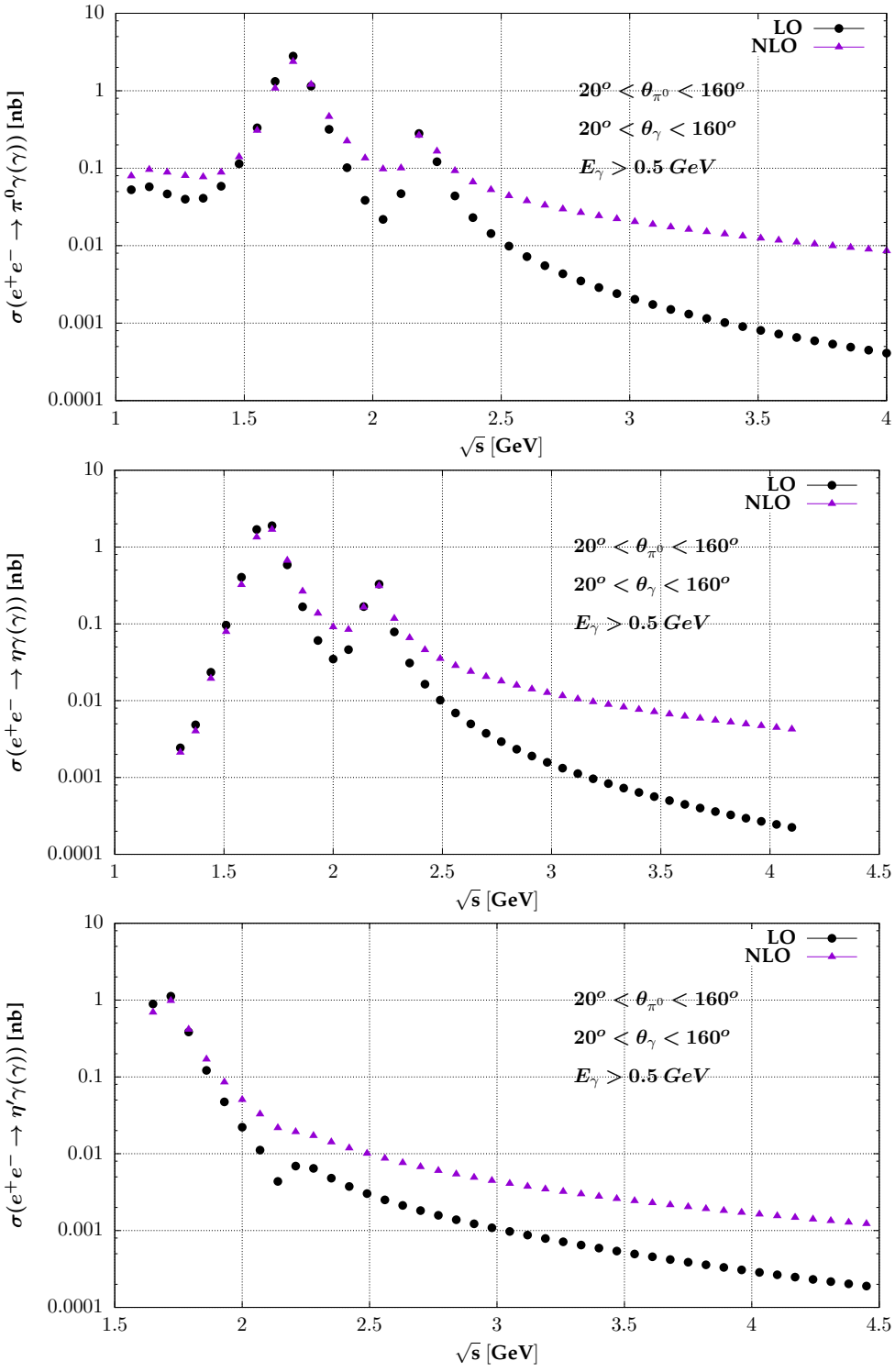

Figure 4.14: Comparison between LO and NLO cross sections for the reaction $e^+e^- \to P\gamma(\gamma)$. The comparison obtained for the form factors with the parameters from fit2.

4.5 Conclusions

The newly developed model of the two-photon transition form factors for pseudoscalar mesons is consistent with most of the experimental data in the time-like and the space-like region. The excluded data sets are in evident conflict with the rest of the measurements, which can be observed by a direct comparison. The behavior of the pseudoscalar form factors in the time-like region could be verified by a scan measurements of the cross section of the reaction $e^+e^- \to P\gamma$. The radiative corrections for this reaction and event selections close to the one used by BES-III experiment are large and have to be taken into account in the future measurements. The results were obtained using the upgraded version of PHOKHARA (PHOKHARA 9.3).

Chapter 5

Next-to-leading order radiative corrections to the reaction $e^+e^- \to \pi^+\pi^-\gamma$

5.1 Motivation

The observed discrepancy between the Standard Model predictions and the experimental value of the anomalous magnetic moment of the muon is dominated by the hadronic contributions. The leading order hadronic vacuum polarization (HVP) contribution constitute alongside of the hadronic light-by-light (HLbL) part the dominant source of this discrepancy [3,4]. The channel, which gives the biggest contribution to the HVP part and its uncertainty is the pion pair production. The measurements of the $e^+e^- \to \pi^+\pi^-$ cross sections have been performed by BABAR [94], KLOE [95] and BES-III [96] experiments via the radiative return method and SND [97] and CMD-2 [98–100] experiments using the scan method. There is a discrepancy between KLOE and BABAR measurements of the invariant mass distributions of $\pi^+\pi^-$ cross section [95], which is about a few percent on the peak of the ρ resonance. It even increases at higher energies. Both measurements are in good agreement with the BES-III data [96] and data collected by the SND and CMD-2 via scan method [95] but their experimental errors are not competitive with the KLOE and BABAR errors. The KLOE and BABAR collaborations used the approximate NLO $e^+e^- \to \pi^+\pi^-\gamma$ cross section predictions of the Monte Carlo event generator PHOKHARA. To investigate the possible impact of the missing radiative corrections on the pion pair production cross sections, the complete NLO radiative corrections have been calculated [12] as the discrepancy between KLOE and BABAR might have originated partly from

the missing radiative corrections. The possible influence of the missing NLO radiative corrections in the $e^+e^- \to \mu^+\mu^-\gamma$ cross section, which is also important for the precise determination of the pion pair production rate has been investigated in [52]. The results for the muon pair show that the effect of the NLO corrections is very small for typical experimental events selections and that it cannot explain the BABAR and KLOE discrepancy.

In Section 5.2 the discussion of the NLO contributions to the $e^+e^- \to \pi^+\pi^-\gamma$ cross section is performed. Section 5.2.1, 5.2.2 and Section 5.2.3 contain presentation of the methods used to calculate particular classes of the diagrams: pentabox contributions (Section 5.2.1), virtual final state radiative corrections (Section 5.2.2), hard and soft photon emissions (Section 5.2.3). In Section 5.3 the effect of the missing radiative corrections is discussed for BABAR, KLOE and BES events selections. Section 5.4 contains conclusions.

5.2 The pions pair production at the NLO in the radiative return

The full NLO cross section for the pion pair production via radiative return can be written in the following form:

$$\begin{aligned}\sigma_{NLO}(e^+e^- \to \pi^+\pi^- + \text{photons}) = \sigma(e^+e^- \to \pi^+\pi^- + \gamma) \\ + \quad \sigma(e^+e^- \to \pi^+\pi^- + \gamma\gamma),\end{aligned} \tag{5.1}$$

where the cross section $\sigma(e^+e^- \to \pi^+\pi^- + \gamma)$ includes:

- A contribution from the leading order amplitudes presented in Fig. 5.1.
- A contribution from the amplitudes with one hard and one soft photon, which are represented by the diagrams from Fig. 5.2, where the energy of one of the photon fulfills the condition $E_\gamma < E_{min}$.
- A contribution from the virtual corrections diagrams presented in Fig. 5.3, which at the NLO enter the $\sigma(e^+e^- \to \pi^+\pi^-\gamma)$ cross section only through the interference with the leading order amplitudes.

The cross section $\sigma(e^+e^- \to \pi^+\pi^- + \gamma\gamma)$ is calculated using the diagrams from Fig. 5.2, where energies of both photons fulfill the condition $E_\gamma > E_{min}$. Including the contribution from the two hard photons makes the σ_{NLO} cross section independent of the energy cutoff E_{min}. The infrared divergences, which arise from the virtual corrections, are canceled by their counterparts from soft photon emission diagrams making the sum soft+virtual infrared finite.

Figure 5.1: The classes of the diagrams at the leading order for the reaction $e^+e^- \to \pi^+\pi^-\gamma$. The blob indicates that the $\gamma - \pi^+ - \pi^-$ coupling is modeled testing the form factor.

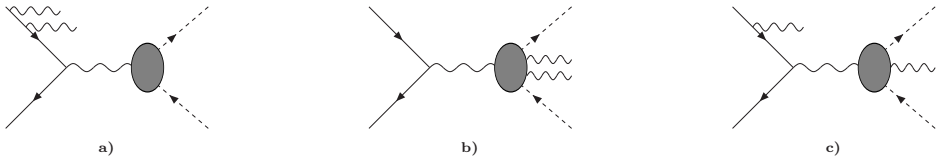

Figure 5.2: The classes of the diagrams with emission of two photons for the reaction $e^+e^- \to \pi^+\pi^-\gamma$.The blob indicates that the $\gamma - \pi^+ - \pi^-$ coupling is modeled testing the form factor.

The version 7.0 of the Monte Carlo event generator PHOKHARA [101], which was used by KLOE and BABAR in their analysis, includes the following NLO amplitudes:

- The amplitude with an emission of two photons from the initial state represented by the diagram from Fig. 5.2a.
- The part of amplitude with an emission of one photon from the initial state and one photon from the final state represented by the diagram from Fig. 5.2c, which cancel the infrared divergence from diagrams presented in Fig. 5.3b and 5.3c.
- Virtual corrections to the initial state with the initial state radiation represented by the diagram from Fig. 5.3a.
- Virtual corrections to the initial state with the final state radiation represented by the diagram from Fig. 5.3b.
- Virtual corrections to the final state with the initial state radiation represented by the diagram from Fig. 5.3c.

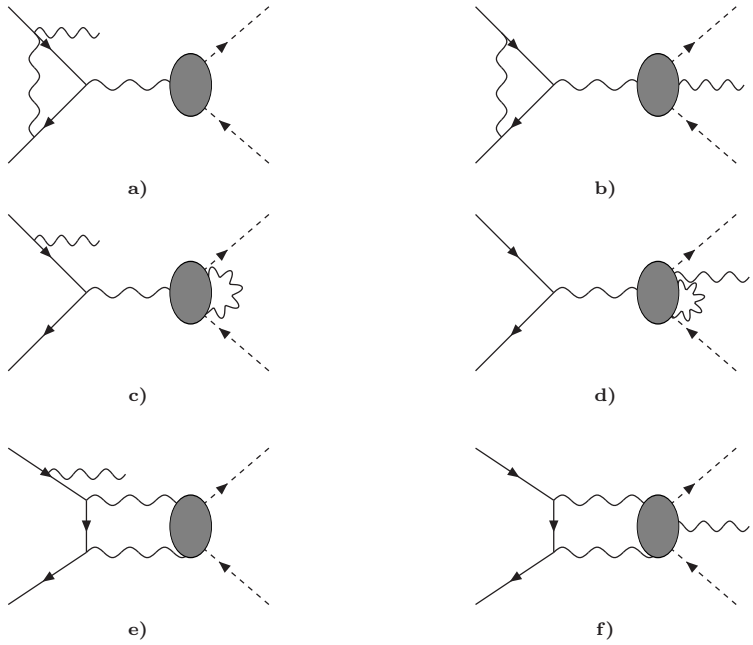

Figure 5.3: The classes of the diagrams at the next-leading-order for the reaction $e^+e^- \to \pi^+\pi^-\gamma$. The blob indicates that the $\gamma - \pi^+ - \pi^-$ coupling is modeled testing the form factor.

For each class of the virtual corrections the corresponding infrared divergent diagrams with soft photon emissions have been included.

The missing NLO radiative corrections to the reaction $e^+e^- \to \pi^+\pi^-\gamma$ include the following classes of diagrams:

- Pentabox and box diagrams with the initial state radiation presented in Fig. 5.3e.
- Pentabox and box diagrams with the final state radiation presented in Fig. 5.3f.
- Virtual corrections to the final state with the final state radiation represented by the diagram from Fig. 5.3d.
- The amplitude with emission of two photons from the final state represented by the diagram from Fig. 5.2b.
- The part of the amplitude represented by the diagram from Fig. 5.2c, which was not included in the previous version of the code.

The indispensable soft photon contributions to cancel infrared divergences from the virtual parts presented in Fig. 5.3e, 5.3f and 5.3b contain:

- The interference of the diagram from Fig. 5.2a, where one of the photons is soft with the diagram from Fig. 5.2c, where photon emitted from the final state is soft. That contribution cancels the infrared divergences, which arise from the interference of the pentabox ISR diagram (Fig. 5.3e) with the leading order amplitude with the ISR photon (Fig. 5.1a).

- The sum of the contribution, which comes from the interference of the diagram from Fig. 5.2a, where one of the photons is soft with diagram from Fig. 5.2b, where one of the photons is soft and the interference of the diagram from Fig. 5.2c, where the photon emitted from the initial state is soft with the diagram from Fig. 5.2c, where the photon emitted from the final state is soft. That contribution cancels the sum of infrared divergences, which arise from the interference of the pentabox ISR diagram (Fig. 5.3e) with leading order amplitude with the FSR photon (Fig. 5.1b) and the interference of the pentabox FSR diagram from Fig. 5.3f with the leading order amplitude with the ISR photon (Fig. 5.1a).

- The interference of the diagram from Fig. 5.2b, where one of the photons is soft with diagram from Fig. 5.2c, where the photon emitted from the initial state is soft. That contribution cancels the infrared divergences, which arise from the interference of the pentabox FSR diagram (Fig. 5.3f) with the leading order amplitude with the FSR photon (Fig. 5.1b).

- The square of the module of the diagram from Fig. 5.2b, where one of the photons is soft, which cancel infrared divergence arising from the interference of the diagram from Fig. 5.3d with the leading order FSR amplitude.

- The interference of the diagram from Fig. 5.2b, where one of the photons is soft with diagram from Fig. 5.2c, where the photon emitted from the final state is soft. This contribution cancel the infrared divergences, which arise from the interference of the diagram from Fig. 5.3d with the leading order amplitude with the ISR photon.

The cancelation of the infrared divergences between virtual and soft corrections has been checked numerically by comparing coefficients multiplying the $\frac{1}{\epsilon_{IR}}$ poles.

5.2.1 The pentabox contributions

In the framework of Scalar Quantum Electrodynamics (sQED) the virtual corrections of the pentabox-type include the pentagon, the box and the triangle diagrams. The triangle topology is a consequence of the two-photon coupling to the scalar-antiscalar pair, which introduces an additional diagram. All of the pentabox-type diagrams can be grouped into four gauge invariant subclasses:

- The subclass, which includes pentagon and box diagrams with the initial state radiation, presented in Fig. 5.4. The diagrams, which can be obtained by crossing the scalar and antiscalar lines are separately gauge invariant and also have been taken into account in the calculations.
- The subclass, which includes box and triangle diagrams with the two-photon-two-scalar vertex and photon emitted from the initial states, presented in Fig. 5.5.
- The subclass, which includes pentagon and box diagrams with the final state radiation, presented in Fig. 5.6. The diagrams, which can be obtained by crossing the scalar and antiscalar lines are separately gauge invariant and also have been taken into account in the calculations.
- The subclass, which includes triangle diagrams with the two-photon-two scalar vertex and photon emitted from the final states, presented in Fig. 5.7.

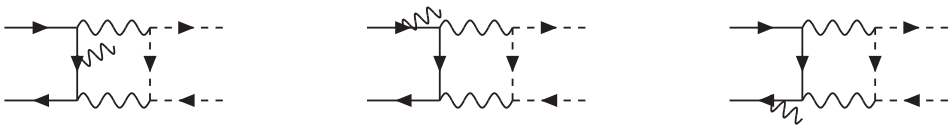

Figure 5.4: The gauge invariant class of scalar QED pentabox and box diagrams with the initial state radiation. Cross diagrams are not shown.

In the version 7.0 of the PHOKHARA Monte Carlo event generator [101] the real radiation from pion (antipion) was modeled as the radiation from the point-like particles and the amplitudes were calculated in the framework of sQED with the pion form factor included only in the vertex with coupling of the pion-antipion to the virtual photon. In the case of pentabox diagrams the similar factorization of the pion form factor is used. The modeling of the

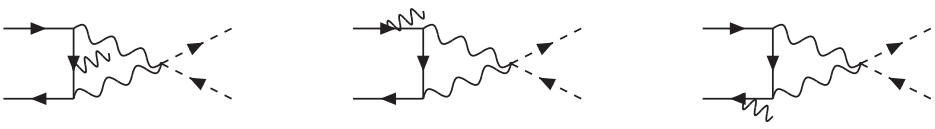

Figure 5.5: The gauge invariant class of scalar QED box and triangle diagrams with the initial state radiation.

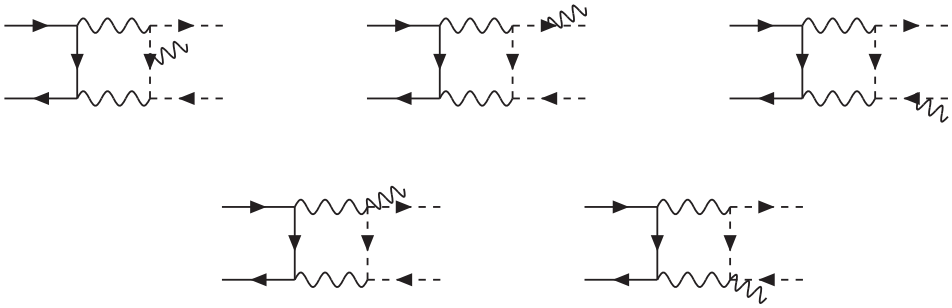

Figure 5.6: The gauge invariant class of scalar QED pentabox and box diagrams with the final state radiation. Cross diagrams are not shown.

Figure 5.7: The gauge invariant class of scalar QED triangle diagrams with the final state radiation.

pentabox-type virtual corrections for the pion-antipion pair can be presented schematically in the following way:

$$\mathcal{M}(e^+e^- \to \pi^+\pi^-\gamma_{ISR}) = F_\pi(Q^2)\mathcal{M}_{sQED}(e^+e^- \to \pi^+\pi^-\gamma_{ISR}), \quad (5.2)$$

$$\mathcal{M}(e^+e^- \to \pi^+\pi^-\gamma_{FSR}) = F_\pi(s)\mathcal{M}_{sQED}(e^+e^- \to \pi^+\pi^-\gamma_{FSR}), \quad (5.3)$$

where $\mathcal{M}$ is the amplitude for the pentabox-type diagrams, F_π is a pion form factor, s is Mandelstam variable, Q^2 invariant mass of the pions and $\mathcal{M}_{sQED}$ is the amplitude calculated within the scalar QED. In this model the pentabox-type virtual corrections to the amplitudes are assumed to be a product of the form factors, with parameterization adopted from [25] and

the amplitude calculated within the scalar QED. For a real emission the amplitudes are proportional to the pion form factor, which is calculated at Q^2 for amplitudes with the ISR photons and at s for amplitudes, which involve only the FSR photons. The factorization of the form factors for the pentabox diagrams provide that the interference terms of this contribution with the born amplitude are proportional to the same combination of the form factors as their counterparts with soft photons emission. This ensure that the result, which include sum of virtual and soft corrections, is infrared finite.

A Fortran code for the pentabox-type contributions have been prepared using a special Mathematica code, which used the trace method to calculate the necessary interference terms. The tensor integrals are calculated using the method described in [102, 103], which has been extended to include 5-point functions according to convention presented in [104]. The scalar one-loop integrals are calculated using QCDLoop library [105]. The pentabox-type diagrams are infrared divergent (IR) and ultraviolet (UV) finite. This divergence has been regularized using dimensional regularization scheme [106] and canceled by the appropriate soft photon contributions. The analytic expressions for the amplitudes are rather long (about 3000 lines of the FORTRAN code) and will not be presented in this thesis.

To assure necessary precision of the calculations and numerical stability of the code, the combined double and quadruple precision is used. The one-loop scalar integrals are calculated in double precision, while all other calculations are held in quadruple precision. The code, where only double precision is used, does not ensure numerical stability. The numerical cancellations, which occur for some specific points of the phase space cause loss of all significant digits of the result.

The following tests of the implementation of the amplitudes and check of the stability of the code have been performed:

- An independent code has been prepared, which was generated using FeynCalc [107], where a different method is used for calculating of the tensor integrals. Both the scalar and the tensor integrals were calculated in quadruple precision using LoopTools library [108]:
  - A perfect agreement between both codes has been observed for the kinematic points far from soft and collinear regions.
  - An agreement at the level 10^{-5} between both codes has been observed for soft and collinear regions.
- The implemented scalar integrals in double precision has been checked numerically using quadruple precision routines for different kinematic

points. The agreement at the level 10^{-15} has been observed for each scalar integral.

- Numerical test of the cancelation of the infrared divergences between the virtual and the soft parts has been performed. For the sum virtual+soft perfect cancelation of the divergences was found.

- Analytical and numerical tests of the gauge invariance have been performed. The substitution $\varepsilon(k) \to k$, where ε is the polarization vector of the photon with momentum k, in the amplitudes within the previously defined gauge invariant classes gives zero analytically. Numerically, no result different than numerical zero has been observed.

5.2.2 Virtual final state radiative corrections

In the frame of sQED the diagrams for the final state virtual corrections with the final state radiation, which were included in the calculations, are presented in Fig. 5.8. These diagrams include vertex correction and pion (antipion) self energy corrections. The diagrams with self energy corrections, where pion (antipion) is on mass shell have been omitted since after the renormalization procedure they will vanish (see Appendix C). The additional diagrams, which contain triangle and bubble topologies presented in Fig. 5.9, with three or two pion propagators cancel between themselves in the sum of these contributions. The full amplitude for the virtual corrections is the product of sQED amplitude and the pion form factor calculated at s.

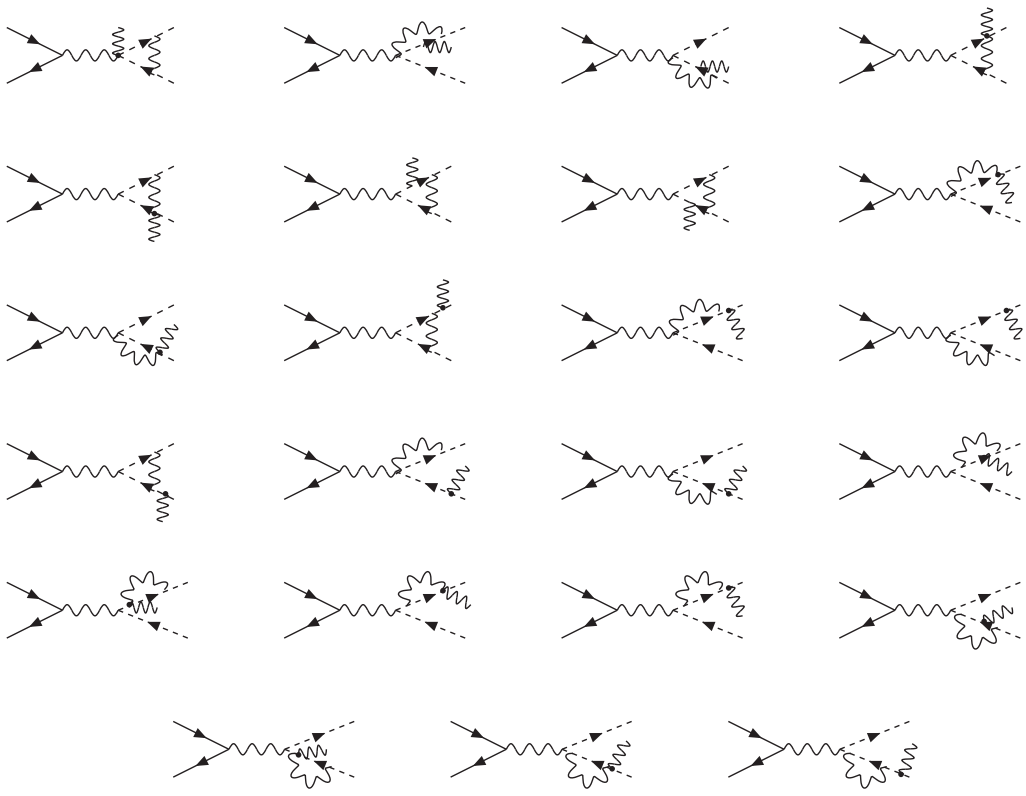

Figure 5.8: Diagrams for virtual final state radiative corrections with final state radiation contributing to the $e^+e^- \to \pi^+\pi^-\gamma$ amplitude within scalar QED.

A Fortran code for the virtual final state radiative corrections has been prepared using the same method as in the case of pentabox contributions

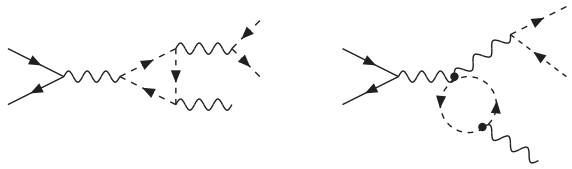

Figure 5.9: The classes of bubble and triangle diagrams, which do not contribute to the $e^+e^- \to \pi^+\pi^-\gamma$ amplitude within scalar QED.

(see Section 5.2.1). These corrections contain infrared (IR) and ultraviolet (UV) divergences, which have been regularized dimensionally. The infrared divergences have been removed by including the appropriate soft photon contributions and the ultraviolet divergences by including the counter-terms amplitudes. The procedure for determination of the renormalization coupling constants is presented in the Appendix C. As in the case of the pentabox contributions, the analytic expression for the virtual final state radiative corrections is quite long (about 1500 lines of the FORTRAN code) and will not be presented in this thesis.

For this part of the code, the use of the double precision was sufficient to ensure numerical stability. The following tests of the code have been performed to check the implementation of the amplitudes and the stability of the code:

- An independent code has been prepared. It was generated using FeynCalc [107], where a different method is used for calculating the tensor integrals. Both the scalar and the tensor integrals were calculated in quadruple precision using LoopTools library [108].
  - A perfect agreement between both codes has been observed for the kinematic points far from the soft and the collinear regions.
  - For soft and collinear regions only loss of a few digits was observed in double precision routine.
- The implemented scalar integrals has been checked numerically using quadruple precision routines for different kinematic points. The agreement at the level of 10^{-15} has been observed for each of the scalar integrals.
- A numerical test of the cancelation of the infrared divergences between

the virtual and the soft parts has been performed. For the sum virtual+soft perfect cancelation of the divergences was found.

- A numerical test of the cancelation of the ultraviolet divergences between the virtual and the counter-term amplitudes has been performed. The ultraviolet divergence for the virtual FSR amplitudes has been separated from the infrared divergence and the resulting terms have been compared numerically with the UV counter-terms. The sum of the both UV parts canceled exactly.

- A numerical test of the gauge invariance has been performed. No result different from numerical zero has been observed.

5.2.3 The hard and the soft photon emissions

The diagrams with two photons emitted from the final state in the framework of sQED, which are presented in Fig. 5.10 represent the following reaction:

$$e^+(p_1) + e^-(p_2) \to \pi^+(q_1) + \pi^-(q_2) + \gamma(k_1) + \gamma(k_2) \tag{5.4}$$

The amplitude for the two-photon emission can be written in the following form:

$$\begin{aligned} \mathcal{M}_{2FSR} &= \mathcal{M}_1(k_1,k_2) + \mathcal{M}_2(k_1,k_2) + \mathcal{M}_3(k_1,k_2) + \mathcal{M}_4(k_1,k_2) \\ &+\mathcal{M}_5(k_1,k_2) + \frac{1}{2}\mathcal{M}_6(k_1,k_2) + \frac{1}{2}\mathcal{M}_7(k_1,k_2) + (k_1 \leftrightarrow k_2), \end{aligned} \tag{5.5}$$

where k_1 and k_2 are photons momenta and $\mathcal{M}_i$ with $i = 1, ..., 7$ are the amplitudes for the diagrams presented in Fig. 5.10. The amplitude for the emission of two hard photons from the final state written in terms of leptonic (L^μ) and hadronic (J^μ) currents has the following form:

$$\mathcal{M}_{2FSR} = L^\mu J_\mu, \tag{5.6}$$

where $L^\mu = -ie\bar{v}(p1)\gamma^\mu u(p_2)$ and hadronic current has the following form:

$$J^\mu = ie^3 F_\pi(s)\Big(Ak_1^\mu + Bk_2^\mu + Cq_1^\mu + E\varepsilon_1^\mu + F\varepsilon_2^\mu\Big), \tag{5.7}$$

where s is Mandelstam variable, F_π is the pion form factor and $\varepsilon_i^\mu \equiv \varepsilon^\mu(k_i)$ is the polarization vector of the photon with momentum k_i. The scalar coefficients in hadronic current have the following form:

$$\begin{aligned} A &= 2(f_2+f_3), \quad B = 2(f_3+f_4), \quad C = 2(f_1+f_2+f_3+f_4), \\ &E = \frac{2q_1.\varepsilon_2}{k2.q_1} - \frac{2q_2.\varepsilon_2}{k2.q_2}, \quad F = \frac{2q_1.\varepsilon_2}{k2.q_1} - \frac{2q_2.\varepsilon_2}{k2.q_2}, \\ &f_1 = \frac{2\varepsilon_1.\varepsilon_2}{D_{k_1k_2q_2}} - \frac{2q_2.\varepsilon_1(k_1.\varepsilon_2 + q_2.\varepsilon_2)}{k_1.q_2 D_{k_1k_2q_2}} - \frac{2q_2.\varepsilon_2(k_2.\varepsilon_1 + q_2.\varepsilon_1)}{k_2.q_2 D_{k_1k_2q_2}}, \\ &f_2 = \frac{q_1.\varepsilon_1 q_2.\varepsilon_2}{k_1.q_1 k_2.q_2}, \\ &f_3 = \frac{2\varepsilon_1.\varepsilon_2}{D_{k_1k_2q_1}} - \frac{2q_1.\varepsilon_1(k_1.\varepsilon_2 + q_1.\varepsilon_2)}{k_1.q_1 D_{k_1k_2q_1}} - \frac{2q_1.\varepsilon_2(k_2.\varepsilon_1 + q_1.\varepsilon_1)}{k_2.q_1 D_{k_1k_2q_1}}, \\ &f_4 = \frac{q_2.\varepsilon_1 q_1.\varepsilon_2}{k_1.q_2 k_2.q_1}, \\ &D_{k_ik_jq_l} = (k_i + k_j + q_l)^2 - m_\pi^2, \end{aligned} \tag{5.8}$$

where m_π is the pion mass. The amplitudes for two photons emission from the final state have been implemented using the helicity amplitude formalism

developed in [53, 54]. The full amplitude for the two photons emission from the final state is the product of sQED amplitude and the pion form factor calculated at s.

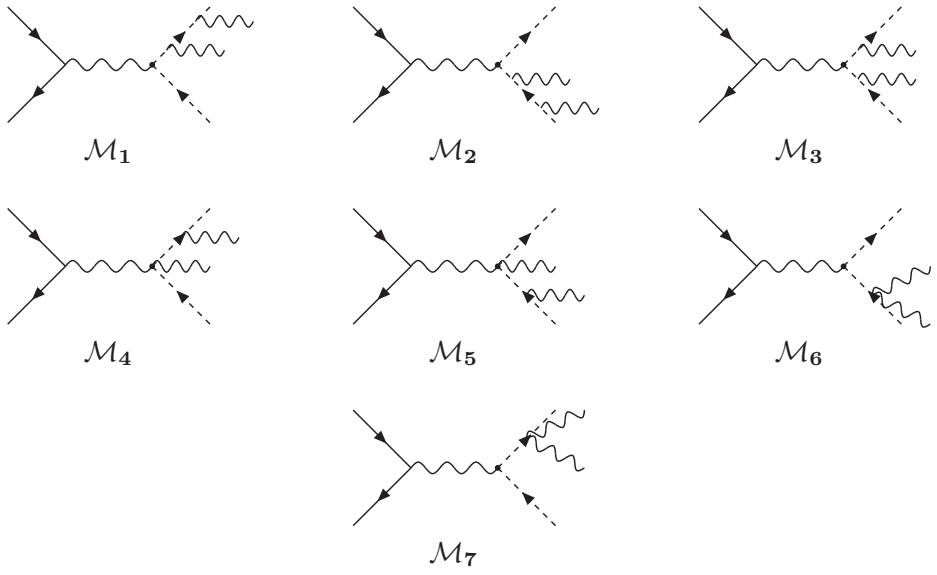

Figure 5.10: Diagrams with two photons emitted from the final state within scalar QED.

The cross section for the emission of one hard and one soft photon, which include the initial state radiation, the final state radiation and the interference can be written in the following form:

$$\sigma_{1h,1s} = \sigma_{1h}\frac{-\alpha}{4\pi}\int_{0\leqslant|k|\leqslant E_{max}}\frac{d^3k}{E_k}\left(\frac{p_1}{p_1\cdot k}-\frac{p_2}{p_2\cdot k}+\frac{q_1}{q_1\cdot k}-\frac{q_2}{q_2\cdot k}\right)^2, \quad (5.9)$$

where p_1, p_2, q_1, q_2 and k are momenta of positron, electron, pion, antipion and photon, σ_{1h} is the cross section for emission of one hard photon and E_{max} is maximal energy of soft photon. The infrared divergence, which appears in the integrals from Eq. 5.9 have been regulated using photon mass regulator λ. To calculate soft photon integrals the method described in [109] has been used. The relation between dimensional regularization and photon mass regulator scheme, which allows to relate infrared divergences from soft part to the one from the virtual part is given by the following formula [52]:

$$\log\left(\frac{\lambda^2}{s}\right) \to \Delta = \frac{(4\pi)^\epsilon}{\epsilon\Gamma(1-\epsilon)}\left(\frac{\mu^2}{s}\right)^\epsilon \quad (5.10)$$

The following tests of the part of the code for the hard and the soft photons emissions have been performed:

- The independent code for hard photon emission has been prepared, which is based on trace method. The numerical comparison between the code, which is based on the helicity amplitude method and the trace method has been done, which checked the implementation of the amplitudes in the PHOKHARA Monte Carlo event generator. A perfect agreement was found.

- A test of the independence of the total cross section (soft+hard) on the cutoff parameter (w), which separates the regions of the phase space for soft and hard photons have been performed. The agreement between the cross sections calculated with two different values of w was a the level of 10^{-5}.

- A numerical test of the gauge invariance for the amplitudes with emission of two hard photons have been performed. No result different than numerical zero has been observed

5.3 Monte Carlo simulations

The plots from Fig. 5.11, 5.12 and 5.13 show the relative size of the pentabox contributions with respect to the old PHOKHARA result [101] as a function of invariant mass of the pions pair. The typical experimental events selections have been used for KLOE, BES-III and BABAR experiments. The details can be found in Appendix D.

The size of the pentabox contributions is very small for typical experimental cuts and can reach up to few per mille of the result of PHOKHARA version used by the KLOE, BES-III and BABAR collaborations. The size of the virtual final state radiative corrections is presented on the plot from Fig. 5.14 for KLOE event selections. These corrections are of the similar size as it was observed in the case of pentabox contributions and can reach up to one per mille for the invariant mass of the pions close to 1 GeV. These corrections are even smaller for the BES and the BABAR event selections. The reason is that the virtual FSR corrections are proportional to the pion form factor calculated at the nominal energy of the experiment, which decreases with the increasing energy [25]. The size of these corrections for the BES event selections is 10 times smaller and for the BABAR event selections even 100 times smaller than the corrections for KLOE event selections.

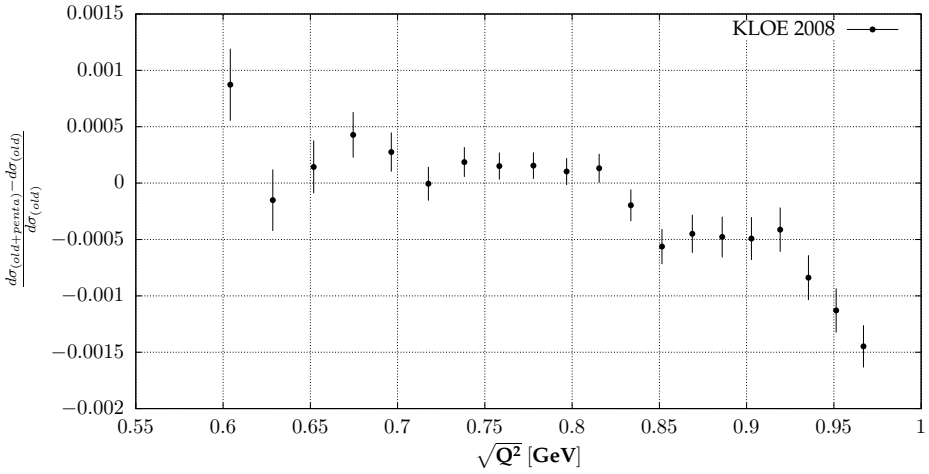

Figure 5.11: The size of the pentabox contributions for KLOE event selections.

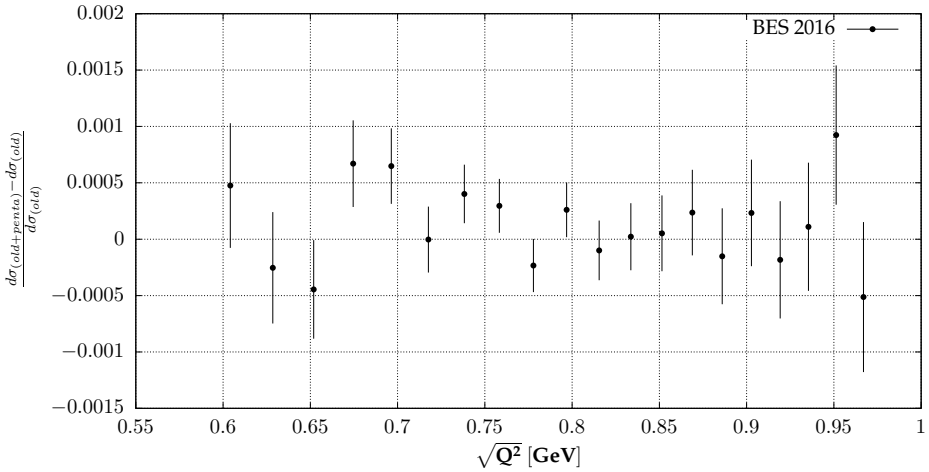

Figure 5.12: The size of the pentabox contributions for BES event selections.

Despite the relative smallness of the missing radiative corrections for the event selections used by KLOE, BES-III and BABAR the corrections are not negligible in the general case. The size of radiative corrections depends on the events selections and has to be analyzed for every specific experimental setup. In the plot from Fig. 5.15 the relative size of the pentabox contributions with respect to the PHOKHARA 7.0 version result [101] as a function of invariant mass of the pions pair for the following event selections is presented:

- $\sqrt{s} = 1.02$ GeV

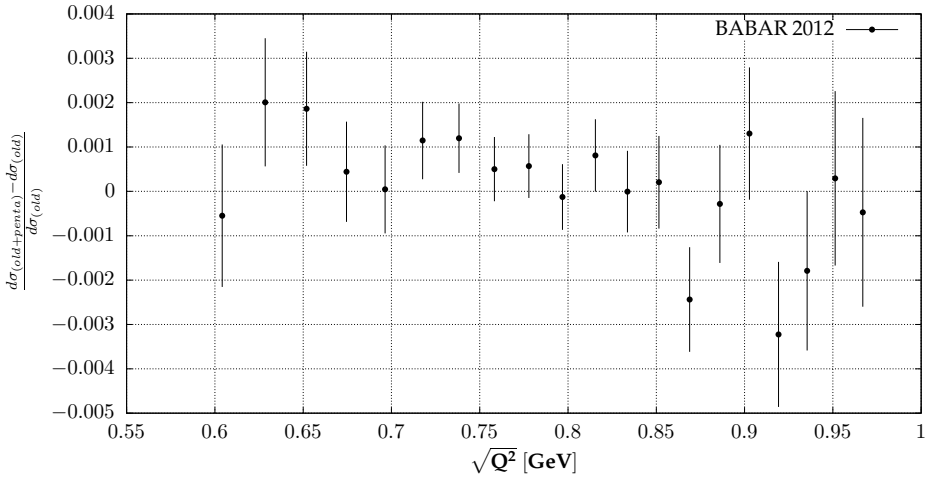

Figure 5.13: The size of the pentabox contributions for BABAR event selections.

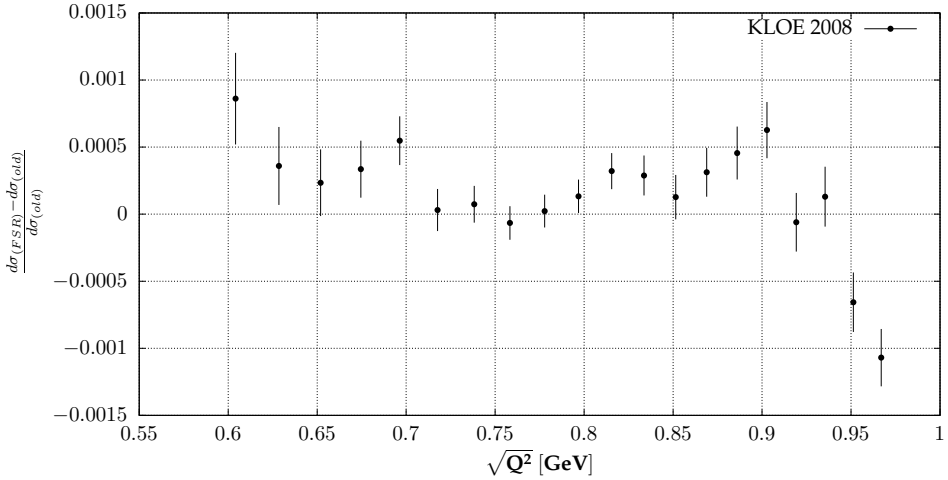

Figure 5.14: The size of the FSR radiative corrections for KLOE event selections.

- Pions and one of the photon polar angle: $20^o < \theta_{\pi^\pm,\gamma} < 160^o$
- $q^2 \in (0.35, 0.95)$

For this event selections the relative size of the pentabox contributions is at the percent level and cannot be neglected in the analysis. In the plot from Fig. 5.16 the relative size of the virtual final state radiative corrections with respect to the PHOKHARA 7.0 version result [101] is presented. The event

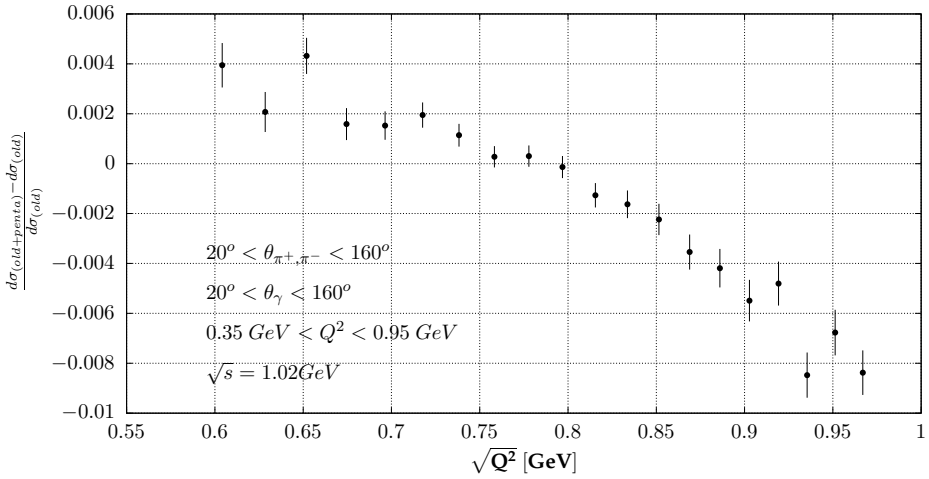

Figure 5.15: The size of the pentabox contributions for the event selections given on the plot.

selections are the same as in the plot for the pentabox contributions presented in Fig. 5.15. The size of the FSR corrections is bigger than it is observed for KLOE event selections but still at the per mille level.

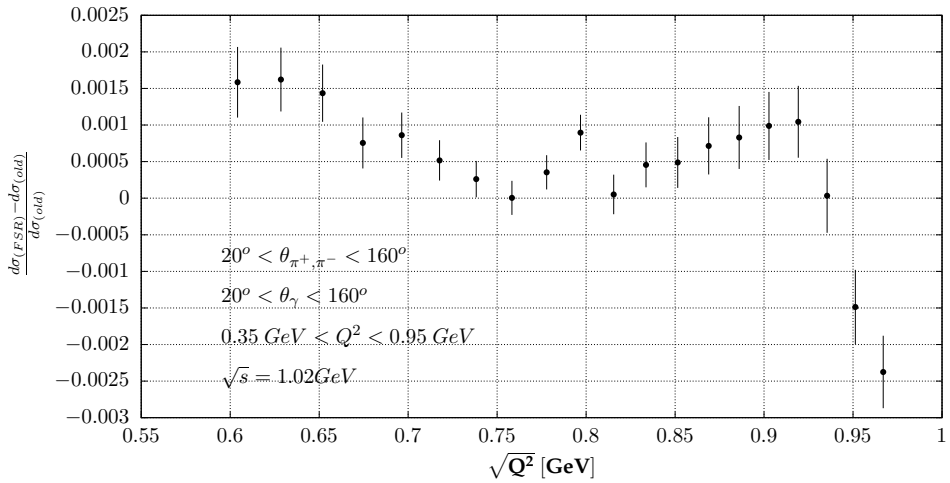

Figure 5.16: The size of the FSR radiative corrections for event selections given on the plot.

5.4 Conclusions

The missing NLO radiative corrections have been included in the new version of the PHOKHARA Monte Carlo event generator (PHOKHARA 10.0). The obtained results for the experimental events selections used by KLOE, BABAR and BES-III show that this corrections are negligible at the current sensitivity of the experiments. Thus the observed discrepancy between KLOE and BABAR measurements of the pions invariant mass distribution in the reaction $e^+e^- \to \pi^+\pi^-\gamma$ cannot be explained by missing NLO corrections. Together with the result of [52] it means that the source of the difference can only be of the experimental origin.

Chapter 6

Final conclusions

In Chapter 2 the model of the nucleon form factors [7] were presented, which well describe most of the experimental data. The analysis show that the effect of the final state radiative corrections beyond the Coulomb factor on the proton-antiproton cross section are small for typical experimental event selections.

In Chapter 3 the production of the χ_{c_1} and the χ_{c_2} states in the electron-positron annihilation was considered [9]. The results show that if the model of the electronic widths is correct the observation of these states should be possible e.g. in the BES-III experiment through the reaction $e^+e^- \to \chi_{c_J} \to \gamma J/\psi(\to \mu^+\mu^-)$ as the interference with the radiative return background.

Chapter 4 presents the results of modeling the two-photon transition form factors of the pseudoscalar mesons [11]. Excluding the data, which are in evident conflict, the model exhibit good agreement with all experimental measurements in the time-like and the space-like region. Analysis of the size of the radiative corrections in the case of BES-III events selections shows that they are large and need to be taken into account in future measurements.

The result presented in Chapter 5 for the missing radiative corrections to the reaction $e^+e^- \to \pi^+\pi^-\gamma$ [12] show that they are small for KLOE, BABAR and BES-III event selections. Thus the observed discrepancy between KLOE and BABAR measurements of the pions invariant mass distribution in the reaction $e^+e^- \to \pi^+\pi^-\gamma$ cannot be explained by missing NLO corrections.

Appendices

Appendix A

Calculation of the FSR amplitudes at the LO and the NLO in the reaction $e^+e^- \to p\bar{p}\gamma$

The FSR at the LO consists of two amplitudes, one with the emission of the photon from the proton ($\mathcal{M}_1$), and one with the emission of the photon from the antiproton ($\mathcal{M}_2$). The amplitudes read:

$$\mathcal{M}_1 = \frac{-ie^3}{s}\bar{v}(p_2)\gamma^\mu u(p_1)\bar{u}(p_3)\not{\epsilon}^*(k)\frac{\not{p}_3 + \not{k} + m_p}{2p_3\cdot k}F_\mu(P)v(p_4), \tag{A.1}$$

$$\mathcal{M}_2 = \frac{-ie^3}{s}\bar{v}(p_2)\gamma^\mu u(p_1)\bar{u}(p_3)F_\mu(P)\frac{-\not{p}_4 - \not{k} + m_p}{2p_4\cdot k}\not{\epsilon}^*(k)v(p_4), \tag{A.2}$$

where p_1, p_2, p_3, p_4 and k are momenta of positron, electron, proton, antiproton and photon, $P = p_1 + p_2$ and ϵ is polarization vector of photon and $\bar{v}(p_2) \equiv \bar{v}(p_2, \lambda_{e^+})$, $u(p_1) \equiv u(p_1, \lambda_{e^-})$, $\bar{u}(p_3) \equiv \bar{u}(p_3, \lambda_{\bar{p}})$, $v(p_4) \equiv u(p_4, \lambda_p)$ and $\epsilon^*(k) \equiv \epsilon^*(k, \lambda_\gamma)$, where λ_i are helicities of given particle. The four-vector $F_\mu(P)$ has the following form:

$$F_\mu(P) = F_1^p(P^2)\gamma_\mu - \frac{F_2^p(P^2)}{4m_p}[\gamma_\mu, \not{P}]. \tag{A.3}$$

Using two dimensional representations of spinors and and γ matrices from [93] one can transform leptonic parts and the amplitudes take the following form:

$$\mathcal{M}_1 = \frac{-ie^3}{s}\Big(v_I^\dagger\sigma_-^\mu u_I + v_{II}^\dagger\sigma_+^\mu u_{II}\Big)J_\mu^1 \tag{A.4}$$

$$\mathcal{M}_2 = \frac{-ie^3}{s}\Big(v_I^\dagger\sigma_-^\mu u_I + v_{II}^\dagger\sigma_+^\mu u_{II}\Big)J_\mu^2, \tag{A.5}$$

where J^1_μ and J^2_μ are the hadronic parts of the amplitudes $\mathcal{M}_1$ and $\mathcal{M}_2$ and $v_{I,II} \equiv v_{I,II}(p_2, \lambda_{e^+})$, $u_{I,II} \equiv u_{I,II}(p_1, \lambda_{e^-})$ and $\sigma_\pm = (I, \pm\sigma_i)$, where σ_i,$i = 1$, 2, 3 are the Pauli matrices and:

$$u(p) = \begin{pmatrix} u_I \\ u_{II} \end{pmatrix}, \qquad v(p) = \begin{pmatrix} v_I \\ v_{II} \end{pmatrix} \tag{A.6}$$

and

$$a_\pm = a_\mu \sigma^\mu_\pm = \begin{pmatrix} a^0 \mp a^3 & \mp(a^1 - ia^2) \\ \mp(a^1 + ia^2) & a^0 \pm a^3. \end{pmatrix} \tag{A.7}$$

After making use of the anticommutation relation of γ matrices and Dirac equation the hadronic currents $J^{1,2}_\mu$ can be rewritten in the following form:

$$J^1_\mu = \bar{u}(p_3) \frac{2\epsilon^*(k)\cdot p_3 + \not{\epsilon}^*(k)\not{k}}{2p_3 \cdot k} F_\mu(P) v(p_4), \tag{A.8}$$

$$J^2_\mu = \bar{u}(p_3) F_\mu(P) \frac{-2\epsilon^*(k)\cdot p_4 - \not{k}\not{\epsilon}^*(k)}{2p_3 \cdot k} v(p_4). \tag{A.9}$$

Inserting two dimensional representation of spinors and γ matrices one obtains:

$$\begin{aligned} J^1_\mu &= \frac{1}{2p_3\cdot k}\Big[F_1(s)\{u^\dagger_I(2\epsilon^*\cdot p_3 + \epsilon^*_- k^+)\sigma^-_\mu v_I + u^\dagger_{II}(2\epsilon^*\cdot p_3 + \epsilon^*_+ k^-)\sigma^+_\mu v_{II}\} \\ &- F_2\{u^\dagger_{II}(2\epsilon^*\cdot p_3 + \epsilon^*_+ k^-)(\sigma^+_\mu P^- - P^+\sigma^-_\mu)v_I \\ &+ u^\dagger_I(2\epsilon^*\cdot p_3 + \epsilon^*_- k^+)(\sigma^-_\mu P^+ - P^-\sigma^+_\mu)v_{II}\}\Big], \end{aligned} \tag{A.10}$$

$$\begin{aligned} J^2_\mu &= \frac{-1}{2p_4\cdot k}\Big[F_1(s)\{u^\dagger_I\sigma^-_\mu(2\epsilon^*\cdot p_4 + k^+\epsilon^*_-)v_I + u^\dagger_{II}\sigma^+_\mu(2\epsilon^*\cdot p_4 + k^-\epsilon^*_+)v_{II}\} \\ &- F_2\{u^\dagger_{II}(\sigma^+_\mu P^- - P^+\sigma^-_\mu)(2\epsilon^*\cdot p_4 + k^+\epsilon^*_-)v_I \\ &+ u^\dagger_I(\sigma^-_\mu P^+ - P^-\sigma^+_\mu)(2\epsilon^*\cdot p_4 + k^-\epsilon^*_+)v_{II}\}\Big], \end{aligned} \tag{A.11}$$

$$\tag{A.12}$$

where $\epsilon = \epsilon^*(k)$ and $v_{I,II} \equiv v_{I,II}(p_4, \lambda_{\bar{p}})$, $u_{I,II} \equiv u_{I,II}(p_3, \lambda_p)$.

The amplitudes with the definite helicities of incoming and outgoing fermions can be written in the following form:

$$\mathcal{M}_{1,2}(\lambda_{e^-}, \lambda_{e^+}, \lambda_p, \lambda_{\bar{p}}) = \frac{-ie^3}{s}\Big[v^\dagger_I J^{1,2}_-(\lambda_p, \lambda_{\bar{p}})u_I + v^\dagger_{II} J^{1,2}_+(\lambda_p, \lambda_{\bar{p}})u_{II}\Big]. \tag{A.13}$$

In the electron-positron center mass system (CMS) with the choice of the z axis along the positron momentum this formula simplifies further into:

$$\mathcal{M}_{1,2}(+,+,\lambda_p,\lambda_{\bar{p}}) = m_e\Big([J_-^{1,2}(\lambda_p,\lambda_{\bar{p}})]_{2,2} - [J_+^{1,2}(\lambda_p,\lambda_{\bar{p}})]_{2,2}\Big), \quad (A.14)$$

$$\mathcal{M}_{1,2}(-,-,\lambda_p,\lambda_{\bar{p}}) = m_e\Big([J_-^{1,2}(\lambda_p,\lambda_{\bar{p}})]_{1,1} - [J_+^{1,2}(\lambda_p,\lambda_{\bar{p}})]_{1,1}\Big), \quad (A.15)$$

$$\begin{aligned}\mathcal{M}_{1,2}(+,-,\lambda_p,\lambda_{\bar{p}}) &= -(E_e+|\bar{p_e}|)[J_-^{1,2}(\lambda_p,\lambda_{\bar{p}})]_{2,1} \\ &\quad + \frac{m_e^2}{(E_e+|\bar{p_e}|)}[J_+^{1,2}(\lambda_p,\lambda_{\bar{p}})]_{2,1}, \quad (A.16)\end{aligned}$$

$$\begin{aligned}\mathcal{M}_{1,2}(-,+,\lambda_p,\lambda_{\bar{p}}) &= \frac{-m_e^2}{(E_e+|\bar{p_e}|)}[J_-^{1,2}(\lambda_p,\lambda_{\bar{p}})]_{1,2} \\ &\quad + (E_e+|\bar{p_e}|)[J_+^{1,2}(\lambda_p,\lambda_{\bar{p}})]_{1,2}, \quad (A.17)\end{aligned}$$

where $[A]_{i,j}$ is i,j matrix element and E_e, $\bar{p_e}$ are energy and length of the momentum vector of electron (positron) in their CMS frame.

The amplitude at the NLO with an emission of one photon from initial and one photon from the final state can be written in the following form:

$$\mathcal{M}_{1FSR,1FSR} = \mathcal{M}_a(k_1,k_2)+\mathcal{M}_b(k_1,k_2)+\mathcal{M}_c(k_1,k_2)+\mathcal{M}_d(k_1,k_2)+(k_1 \leftrightarrow k_2), \quad (A.18)$$

where k_1 and k_2 are photons momenta. Individual amplitudes denoted by a, b, c and d have the following form:

$$\begin{aligned}\mathcal{M}_a(k_1,k_2) &= \frac{ie^4}{q_1^2}\bar{v}(p_2)\gamma^\mu\frac{\not{p}_1-\not{k}_1+m_e}{-2p_1\cdot k_1}\not{\epsilon}_1^* u(p_1) \\ &\quad \bar{u}(p_3)\not{\epsilon}_2^*\frac{\not{p}_3+\not{k}_2+m_p}{2p_3\cdot k_2}F_\mu(q_1)v(p_4), \quad (A.19)\\ \mathcal{M}_b(k_1,k_2) &= \frac{ie^4}{q_1^2}\bar{v}(p_2)\gamma^\mu\frac{\not{p}_1-\not{k}_1+m_e}{-2p_1\cdot k_1}\not{\epsilon}_1^* u(p_1) \\ &\quad \bar{u}(p_3)F_\mu(q_1)\frac{-\not{p}_4-\not{k}_2+m_p}{2p_4\cdot k_2}\not{\epsilon}_2^* v(p_4), \quad (A.20)\\ \mathcal{M}_c(k_1,k_2) &= \frac{ie^4}{q_1^2}\bar{v}(p_2)\not{\epsilon}_1^*\frac{\not{k}_1-\not{p}_2+m_e}{-2p_2\cdot k_1}\gamma^\mu u(p_1) \\ &\quad \bar{u}(p_3)\not{\epsilon}_2^*\frac{\not{p}_3+\not{k}_2+m_p}{2p_3\cdot k_2}F_\mu(q_1)v(p_4), \quad (A.21)\\ \mathcal{M}_d(k_1,k_2) &= \frac{ie^4}{q_1^2}\bar{v}(p_2)\not{\epsilon}_1^*\frac{\not{k}_1-\not{p}_2+m_e}{-2p_2\cdot k_1}\gamma^\mu u(p_1) \\ &\quad \bar{u}(p_3)F_\mu(q_1)\frac{-\not{p}_4-\not{k}_2+m_p}{2p_4\cdot k_2}\not{\epsilon}_2^* v(p_4), \quad (A.22)\end{aligned}$$

where $q_1 = p_1 + p_2 - k_1$. The hadronic parts are known from the LO amplitudes, so now it is sufficient to take care only of the leptonic parts. After some simplifications and inserting two dimensional representation of spinors and γ matrices for an arbitrary hadronic current ($\widetilde{J}$) one obtains two different amplitudes:

$$\widetilde{\mathcal{M}}_1 = \frac{1}{2p_1 \cdot k_1}\Big\{v_I^\dagger \widetilde{J}^-(-2p_1 \cdot \epsilon_1^* + k_1^+\epsilon_{1-}^*)u_I + v_{II}^\dagger \widetilde{J}^+(-2p_1 \cdot \epsilon_1^* + k_1^-\epsilon_{1+}^*)u_I\Big\}, \tag{A.23}$$

$$\widetilde{\mathcal{M}}_2 = \frac{1}{2p_2 \cdot k_1}\Big\{v_I^\dagger(2p_2 \cdot \epsilon_1^* - k_1^+\epsilon_{1-}^*)\widetilde{J}^- u_I + v_{II}^\dagger(2p_2 \cdot \epsilon_1^* - k_1^-\epsilon_{1+}^*)\widetilde{J}^+ u_I\Big\}. \tag{A.24}$$

The above amplitudes with the definite helicities have the following form:

$$\widetilde{\mathcal{M}}_1(\lambda_{e^-}, \lambda_{e^+}, \lambda_p, \lambda_{\bar{p}}) = \frac{-ie^3}{s}\Big[v_I^\dagger A_1(\lambda_p, \lambda_{\bar{p}})u_I + v_{II}^\dagger B_1(\lambda_p, \lambda_{\bar{p}})u_{II}\Big], \tag{A.25}$$

$$\widetilde{\mathcal{M}}_2(\lambda_{e^-}, \lambda_{e^+}, \lambda_p, \lambda_{\bar{p}}) = \frac{-ie^3}{s}\Big[v_I^\dagger A_2(\lambda_p, \lambda_{\bar{p}})u_I + v_{II}^\dagger B_2(\lambda_p, \lambda_{\bar{p}})u_{II}\Big], \tag{A.26}$$

with

$$A_1(\lambda_p, \lambda_{\bar{p}}) = \widetilde{J}^-(\lambda_p, \lambda_{\bar{p}})(-2p_1 \cdot \epsilon_1^* + k_1^+\epsilon_{1-}^*), \tag{A.27}$$

$$B_1(\lambda_p, \lambda_{\bar{p}}) = \widetilde{J}^+(\lambda_p, \lambda_{\bar{p}})(-2p_1 \cdot \epsilon_1^* + k_1^-\epsilon_{1+}^*), \tag{A.28}$$

$$A_2(\lambda_p, \lambda_{\bar{p}}) = (2p_2 \cdot \epsilon_1^* - k_1^+\epsilon_{1-}^*)\widetilde{J}^-(\lambda_p, \lambda_{\bar{p}}), \tag{A.29}$$

$$B_2(\lambda_p, \lambda_{\bar{p}}) = (2p_2 \cdot \epsilon_1^* - k_1^-\epsilon_{1+}^*)\widetilde{J}^+(\lambda_p, \lambda_{\bar{p}}). \tag{A.30}$$

$$\tag{A.31}$$

In the electron-positron center mass system (CMS) with the choice of the z axis along positron momentum the amplitudes $\widetilde{\mathcal{M}}_1$ and $\widetilde{\mathcal{M}}_2$ take the following

form:

$$\widetilde{\mathcal{M}}_{1,2}(+,+,\lambda_p,\lambda_{\bar{p}}) = m_e\Big([A_{1,2}(\lambda_p,\lambda_{\bar{p}})]_{2,2} - [B_{1,2}(\lambda_p,\lambda_{\bar{p}})]_{2,2}\Big), \quad \text{(A.32)}$$

$$\widetilde{\mathcal{M}}_{1,2}(-,-,\lambda_p,\lambda_{\bar{p}}) = m_e\Big([A_{1,2}(\lambda_p,\lambda_{\bar{p}})]_{1,1} - [B_{1,2}(\lambda_p,\lambda_{\bar{p}})]_{1,1}\Big), \quad \text{(A.33)}$$

$$\begin{aligned}\widetilde{\mathcal{M}}_{1,2}(+,-,\lambda_p,\lambda_{\bar{p}}) &= -(E_e+|\bar{p_e}|)[A_{1,2}(\lambda_p,\lambda_{\bar{p}})]_{2,1} \\ &\quad +\frac{m_e^2}{(E_e+|\bar{p_e}|)}[B_{1,2}(\lambda_p,\lambda_{\bar{p}})]_{2,1}, \quad \text{(A.34)}\end{aligned}$$

$$\begin{aligned}\widetilde{\mathcal{M}}_{1,2}(-,+,\lambda_p,\lambda_{\bar{p}}) &= \frac{-m_e^2}{(E_e+|\bar{p_e}|)}[A_{1,2}(\lambda_p,\lambda_{\bar{p}})]_{1,2} \\ &\quad +(E_e+|\bar{p_e}|)[B_{1,2}(\lambda_p,\lambda_{\bar{p}})]_{1,2}, \quad \text{(A.35)}\end{aligned}$$

Appendix B

Loop integrals for calculation of χ_{c_J} electronic widths

B.1 Loop integrals involved in the short distance approximation

The integrals to be calculated in the short distance approximation have the following form:

$$I_1 = \int d^4h \frac{1}{h^2[(h-l_l)^2-m^2]^2}, \tag{B.1}$$

$$I_2 = \int d^4h \frac{p_1^2+p_2^2}{p_1^2p_2^2[(h-l_l)^2-m^2]^2}, \tag{B.2}$$

$$I_3^{\mu\nu} = \int d^4h \frac{h^\mu h^\nu(p_1^2+p_2^2)}{h^2p_1^2p_2^2[(h-l_l)^2-m^2]^2}, \tag{B.3}$$

$$I_4 = \int d^4h \frac{1}{p_1^2p_2^2[(h-l_l)^2-m^2]^2}, \tag{B.4}$$

$$I_5^{\mu\nu\alpha} = \int d^4h \frac{h^\mu h^\nu h^\alpha}{h^2p_1^2p_2^2[(h-l_l)^2-m^2]^2}, \tag{B.5}$$

where $l_l = \frac{l_- - l_+}{2}$. The following relation allows to simplify the square of $[(h-l_l)^2-m^2]$ in the denominator:

$$[(h-l_l)^2-m^2]^{-2} = \frac{\partial}{\partial m^2}[(h-l_l)^2-m^2]^{-1}. \tag{B.6}$$

The scalar integrals I_1, I_2 and I_4, after applying the relation B.6, take the following form:

$$I_1 = = i\pi^2 \frac{\partial}{\partial m^2} B_0(l_l^2, 0, m^2), \tag{B.7}$$

$$I_2 = i2\pi^2 \frac{\partial}{\partial m^2} B_0(l_k^2, 0, m^2), \tag{B.8}$$

$$I_4 = i\pi^2 \frac{\partial}{\partial m^2} C_0(l_k^2, 4l_k^2, 0, m^2, 0), \tag{B.9}$$

where $l_k = -\frac{l_- + l_+}{2}$ and in the scalar 2-point and 3-point functions the following convention is used

$$B_0(q^2, m_1, m_2) = \frac{\mu^{4-n}}{i\pi^2} \int d^4k \frac{1}{[k^2 - m_1^2][(k-q)^2 - m_2^2]}, \tag{B.10}$$

$$C_0(q_1^2, q_2^2, m_1^2, m_2^2, m_3^2) = \frac{\mu^{4-n}}{i\pi^2} \int d^4k \frac{1}{[k^2 - m_1^2][(k-q_1)^2 - m_2^2][(k-q_1-q_2)^2 - m_3^2]}. \tag{B.11}$$

The tensor integral $I_{3\mu\nu}$, which is symmetric under the permutation of indices can be written as:

$$I_{3\mu\nu} = g_{\mu\nu} A + (l_\mu^+ l_\nu^- + l_\nu^+ l_\mu^-) B + l_\mu^+ l_\nu^+ C + l_\mu^- l_\nu^- D, \tag{B.12}$$

where coefficients A, B, C and D are scalar functions of the external momenta. Only constant A contributes to the integral $I_{3\mu\nu}$ because other parts after contracting with the external momenta and the metric tensor, and after making use of Dirac equation are proportional to the electron mass (see. Eq. 3.22 or 3.24). The solution for A has the the following form:

$$A = \frac{1}{2} I_{3\mu\nu} \Big(g^{\mu\nu} - \frac{4 l^{+\mu} l^{-\nu}}{M^2} \Big). \tag{B.13}$$

The algebraic manipulations were performed using FORM [110]. Inserting the expression for A into Eq. B.12 the following formula is obtained:

$$I_{3\mu\nu} = g_{\mu\nu} \int d^4h \Bigg(\frac{\frac{1}{2} - \frac{h\cdot l_+}{M^2}}{p_1^2[(h-l_l)^2 - m^2]^2} + \frac{\frac{1}{2} + \frac{h\cdot l_-}{M^2}}{p_2^2[(h-l_l)^2 - m^2]^2} + \frac{\frac{1}{4} + \frac{m^2}{M^2}}{h^2[(h-l_l)^2 - m^2]^2} + \frac{1}{M^2} \frac{1}{h^2[(h-l_l)^2 - m^2]} - \frac{1}{M^2} \frac{1}{[(h-l_l)^2 - m^2]} \Bigg). \tag{B.14}$$

In the first two integrals the changes of integration variables $h \to l_- - \bar{h}$ and $h \to \bar{h} - l_+$ are done. Then, after some simplification the following result is obtained:

$$\begin{aligned} I_{3\mu\nu} &= g_{\mu\nu} \int d^4h \Bigg(\frac{1}{2} \frac{1}{p_1^2[(h-l_l)^2 - m^2]^2} + \frac{1}{2} \frac{1}{p_2^2[(h-l_l)^2 - m^2]^2} \\ &- \frac{\frac{3}{4} + \frac{m^2}{M^2}}{h^2[(h-l_k)^2 - m^2]^2} - \frac{1}{M^2} \frac{1}{h^2[(h-l_k)^2 - m^2]} + \frac{1}{M^2} \frac{1}{[(h-l_k)^2 - m^2]^2} \\ &+ \frac{\frac{1}{4} + \frac{m^2}{M^2}}{h^2[(h-l_l)^2 - m^2]^2} + \frac{1}{M^2} \frac{1}{h^2[(h-l_l)^2 - m^2]} - \frac{1}{M^2} \frac{1}{[(h-l_l)^2 - m^2]^2} \Bigg), \end{aligned} \tag{B.15}$$

where in the integrals over $d^4\bar{h}$, $\bar{h} \to h$ has been renamed. Using the relation B.6 and the notation for scalar integrals from Eqs. B.10 and B.11 $I_{3\mu\nu}$ has the following:

$$\begin{aligned} I_{3\mu\nu} &= i\pi^2 g_{\mu\nu} \Big(\frac{1}{M^2} B_0(l_l^2, 0, m^2) - \frac{1}{M^2} B_0(l_k^2, 0, m^2) + \frac{1}{4} \frac{\partial}{\partial m^2} B_0(l_l^2, 0, m^2) \\ &+ \frac{m^2}{M^2} \frac{\partial}{\partial m^2} B_0(l_l^2, 0, m^2) + \frac{1}{4} \frac{\partial}{\partial m^2} B_0(l_k^2, 0, m^2) - \frac{m^2}{M^2} \frac{\partial}{\partial m^2} B_0(l_k^2, 0, m^2) \Big). \end{aligned} \tag{B.16}$$

The tensor loop integral $I_{5\mu\nu\alpha}$ which is symmetric under the permutation of indices can be written as:

$$\begin{aligned} I_{5\mu\nu\alpha} &= l_\alpha^- l_\mu^- l_\nu^- A + l_\alpha^+ l_\mu^+ l_\nu^+ B + (l_\alpha^- l_\mu^+ l_\nu^+ + l_\nu^- l_\alpha^+ l_\mu^+ + l_\mu^- l_\nu^+ l_\alpha^+) C \\ &+ (l_\alpha^+ l_\mu^- l_\nu^- + l_\nu^+ l_\alpha^- l_\mu^- + l_\mu^+ l_\nu^- l_\alpha^-) D + (l_{k_\alpha} g_{\mu\nu} + l_{k_\nu} g_{\alpha\mu} + l_{k_\mu} g_{\nu\alpha}) E \\ &+ (l_{l_\alpha} g_{\mu\nu} + l_{l_\nu} g_{\alpha\mu} + l_{l_\mu} g_{\nu\alpha}) F, \end{aligned} \tag{B.17}$$

where coefficients A, B, C, D, E and F are scalar functions of invariants created from the external momenta. Since terms with A, B, C and D are proportional to the electron mass after contraction with the external momenta and the metric tensor, and use of the Dirac equation only terms proportional to E and F contribute. The following solutions for E and F are obtained:

$$E = \frac{1}{M^2} I_5^{\mu\nu\alpha} \Big(g_{\mu\alpha} l_{-_\nu} - \frac{4}{M^2} l_{+_\nu} l_{-_\mu} l_{-_\alpha} \Big), \tag{B.18}$$

$$F = \frac{1}{M^2} I_5^{\mu\nu\alpha} \Big(g_{\mu\alpha} l_{+_\nu} - \frac{4}{M^2} l_{-_\alpha} l_{+_\mu} l_{+_\nu} \Big), \tag{B.19}$$

Tensor integral $I_{5\mu\nu\alpha}$ enters the amplitude $A(\chi_{c_2} \to e^+e^-)$ through the contraction with the term $\epsilon^{\mu\nu}\gamma_\alpha$. Inserting the expressions for E and F to the

equation for $I_{5\mu\nu\alpha}$ one gets:

$$\bar{v}(l_+)\epsilon^{\mu\nu}\int\frac{d^4h}{(2\pi)^4}\frac{1}{h^2p_1^2p_2^2[(h-l_l)^2-m^2]^2}\not{h}h_\mu h_\nu u(l_-) =$$
$$\bar{v}(l_+)\gamma_\mu(l_+^\nu - l_-^\nu)u(l_-)\epsilon_{\mu\nu}\int\frac{d^4h}{(2\pi)^4}\frac{1}{h^2p_1^2p_2^2[(h-l_l)^2-m^2]^2}$$
$$\Big(-h^2+\frac{p_1^2+p_2^2}{2}\Big)\Big(-M^2-h^2-\frac{p_1^2p_2^2}{h^2}+p_1^2+p_2^2\Big), \qquad \text{(B.20)}$$

Coming back to integral $I_{5\mu\nu\alpha}$, using the derived result and changing the integration variable $h \to \bar{h} + l_l$ one obtains:

$$\begin{aligned} I_{5\mu\nu\alpha} &= 2(l_{l\alpha}g_{\mu\nu}+l_{l\nu}g_{\alpha\mu}+l_{l\mu}g_{\nu\alpha})\int\frac{d^4\bar{h}}{(2\pi)^4}\Big(\frac{\frac{4(l_l\cdot\bar{h})^2}{M^4}-\frac{1}{4}}{(l_k-\bar{h})^2(l_k+\bar{h})^2(\bar{h}^2-m^2)^2} \\ &+ \frac{\frac{-l_l\cdot\bar{h}}{M^4}+\frac{1}{4M^2}}{(l_k-\bar{h})^2(\bar{h}^2-m^2)^2}+\frac{\frac{-l_l\cdot\bar{h}}{M^4}+\frac{1}{4M^2}}{(l_k+\bar{h})^2(\bar{h}^2-m^2)^2}-\frac{\frac{m^2}{M^4}+\frac{1}{4M^2}}{(\bar{h}^2-m^2)^2(\bar{h}+l_l)^2} \\ &+ \frac{1}{M^4}\frac{1}{(\bar{h}^2-m^2)^2}-\frac{1}{M^4}\frac{1}{(\bar{h}^2-m^2)(\bar{h}+l_l)^2}\Big), \qquad \text{(B.21)} \end{aligned}$$

The integral, which has $(l_l \cdot h)^2$ term in the numerator is only a function of l_k, and can be written in the general form:

$$T^{\mu\nu} = g^{\mu\nu}A + l_k^\mu l_k^\nu B, \qquad \text{(B.22)}$$

where $T^{\mu\nu}$ represents arbitrary tensor integral, which is a function of l_k, and scalar coefficients A and B depend only on l_k^2. After contracting with $g^{\mu\nu}$ and $l_k^\mu l_k^\nu$ the following results for A and B coefficients are obtained:

$$B = \frac{4}{M^2}(T_{\mu\nu}g^{\mu\nu}-4A), \qquad \text{(B.23)}$$
$$A = \frac{1}{M^2}T_{\mu\nu}(l_k^\mu l_k^\nu - \frac{M^2}{4}g^{\mu\nu}). \qquad \text{(B.24)}$$

Contracting the expression for $T^{\mu\nu}$ with $l_\mu l_{l\nu}$ lead to the following relation:

$$(\bar{h}\cdot l_l)^2 = -\frac{M^2}{12}\bar{h}^2+\frac{1}{3}(l_k\cdot\bar{h})^2. \qquad \text{(B.25)}$$

This relation allows to simplify the 2nd order tensor integral. The remaining 1st order tensor integrals, which contain first power of $l_l \cdot \bar{h}$ in the numerator depend only on l_k and can be written as $T^\mu = Al_k^\mu$ but since l_k is orthogonal to l_l the terms proportional to $l_l \cdot \bar{h}$ give zero. The result for I_5 after making

use of the relation B.6 and introducing notation from Eqs. B.10 and B.11 is the following:

$$\begin{aligned} I_{5\mu\nu\alpha} &= i\pi^2 2(l_{l\alpha}g_{\mu\nu}+l_{l\nu}g_{\alpha\mu}+l_{l\mu}g_{\nu\alpha})\Bigg(\frac{1}{M^4}B_0(l_l^2,0,m^2) \\ &- (\frac{m^2}{M^4}-\frac{1}{4M^2})\frac{\partial}{\partial m^2}B_0(l_l^2,0,m^2)+\frac{1}{3M^4}B_0(l_k^2,0,m^2) \\ &+ (\frac{m^2}{3M^4}+\frac{7}{12M^2})\frac{\partial}{\partial m^2}B_0(l_k^2,0,m^2)+\frac{2}{3M^4}\frac{\partial}{\partial m^2}A_0(m^2) \\ &- \frac{1}{3M^2}C_0(l_k^2,4l_k^2,0,m^2,0)-(\frac{1}{4}+\frac{m^2}{3M^2})\frac{\partial}{\partial m^2}C_0(l_k^2,4l_k^2,0,m^2,0)\Bigg), \end{aligned} \tag{B.26}$$

where $A_0(m^2)=\frac{\mu^{4-n}}{i\pi^2}\int d^4k\frac{1}{[k^2-m_1^2]}$.

B.2 Loop integrals involved in long distance calculations

The loop integrals involved in the calculations of long distance contributions have the following form:

$$\bar{I}_1 = \int d^4h \frac{p_2^2}{h^2[p_2^2-M_x^2][(h-l_l)^2-m^2]^2}, \tag{B.27}$$

$$\bar{I}_2 = \int d^4h \frac{p_1^2+p_2^2}{p_1^2[p_2^2-M_x^2][(h-l_l)^2-m^2]^2}, \tag{B.28}$$

$$\bar{I}_3^{\mu\nu} = \int d^4h \frac{h^\mu h^\nu(p_1^2+p_2^2)}{h^2p_1^2[p_2^2-M_x^2][(h-l_l)^2-m^2]^2}, \tag{B.29}$$

$$\bar{I}_4 = \int d^4h \frac{1}{p_1^2[p_2^2-M_x^2][(h-l_l)^2-m^2]^2}, \tag{B.30}$$

$$\bar{I}_5^{\mu\nu\alpha} = \int d^4h \frac{h^\mu h^\nu h^\alpha}{h^2p_1^2[p_2^2-M_x^2][(h-l_l)^2-m^2]^2}. \tag{B.31}$$

Canceling the p_2^2 in the numerator of integrals $\bar{I}_1$ and $\bar{I}_2$ and then making use of the relation B.6, the scalar integrals $\bar{I}_1$, $\bar{I}_2$ and I_4 can be written in

the following form:

$$\bar{I}_1 = i\pi^2 M^2 \Big(\frac{\partial}{\partial m^2} B_0(l_l^2, 0, m^2) + 2M_x^2 \frac{\partial}{\partial m^2} C_0(l_k^2, 0, m^2, 0, M_x^2) \Big), \tag{B.32}$$

$$\bar{I}_2 = i\pi^2 M^2 \Big(\frac{\partial}{\partial m^2} B_0(l_k^2, 0, m^2) + \frac{\partial}{\partial m^2} B_0(l_k^2, M_x^2, m^2) \Big) + M_x^2 \frac{\partial}{\partial m^2} C_0(l_k^2, 4l_k^2, m^2, 0, M_x^2), \tag{B.33}$$

$$\bar{I}_4 = i2\pi^2 \frac{\partial}{\partial m^2} C_0(l_k^2, 4l_k^2, m^2, 0, M_x^2), \tag{B.34}$$

The tensor integral $\bar{I}_{3\mu\nu}$ can be reduced in the same way as it was done for integral $I_{3\mu\nu}$ from Eq. B.3. After making use of Eqs. B.12 and B.13 with substitution $I_{3\mu\nu} \to \bar{I}_{3\mu\nu}$ one gets the following:

$$\begin{aligned} \bar{I}_{3\mu\nu} = g_{\mu\nu} \int d^4h \Bigg(& \frac{M_x^2}{M^2} \frac{4h \cdot l_+ h \cdot l_-}{p_1^2 h^2 [(h-l_l)^2 - m^2]^2 [p_2^2 - M_x^2]} \\ & + \frac{1}{M^2} \frac{4h \cdot l_+ h \cdot l_-}{p_1^2 h^2 [(h-l_l)^2 - m^2]^2} - \frac{M_x^2}{p_1^2 [(h-l_l)^2 - m^2]^2 [p_2^2 - M_x^2]} \\ & - \frac{1}{p_1^2 [(h-l_l)^2 - m^2]^2} + \frac{1}{M^2} \frac{4h \cdot l_+ h \cdot l_-}{h^2 [(h-l_l)^2 - m^2]^2 [p_2^2 - M_x^2]} \\ & - \frac{1}{[(h-l_l)^2 - m^2]^2 [p_2^2 - M_x^2]} \Bigg). \end{aligned} \tag{B.35}$$

This could be further simplified by canceling the double scalar products $l_\pm \cdot h$ in the numerator by some of the denominators. After this, the remaining tensor integrals contain only first powers of $l_\pm \cdot h$. Changing the integration variables $h \to \bar{h} + l_l$ one can rewrite $l_\pm$ in terms of l_l and l_k. After this procedure the only tensor integral that is left depends on l_k. For this integrals the tensor reductions leads to the terms in the numerator proportional to

$l_l \cdot l_k = 0$. Using the relation B.6 one obtains:

$$\begin{aligned}
\bar{I}_{3\mu\nu} &= i\pi^2 g_{\mu\nu}\Big(-\frac{1}{2}M^2 y C_0(l_k^2,0,m^2,0,M_x^2) - \frac{1}{4}M^2 y C_0(l_k^2,4l_k^2,m^2,0,M_x^2) \\
&- (\frac{1}{2}M^2M_x^2 + \frac{1}{2}m^2M^2y)\frac{\partial}{\partial m^2}C_0(l_k^2,0,m^2,0,M_x^2) \\
&- \frac{1}{4}(3M^2M_x^2 + m^2M^2y - M^2M_x^2y)\frac{\partial}{\partial m^2}C_0(l_k^2,4l_k^2,m^2,0,M_x^2) \\
&+ B_0(l_k^2,0,m^2) + \frac{1}{4}(4m^2 - M^2 + M^2y)\frac{\partial}{\partial m^2}B_0(l_k^2,0,m^2) \\
&- 2B_0(l_l^2,0,m^2) - \frac{1}{2}(4m^2+M^2)\frac{\partial}{\partial m^2}B_0(l_l^2,0,m^2) + B_0(l_k^2,M_x^2,m^2) \\
&+ \frac{1}{4}(4m^2 - M^2 + M^2y)\frac{\partial}{\partial m^2}B_0(l_k^2,M_x^2,m^2)\Big). \qquad \text{(B.36)}
\end{aligned}$$

The tensor integral $\bar{I}_{5\mu\nu\alpha}$ is simplified by making use of the following relation:

$$\begin{aligned}
&\bar{v}(l_+)\epsilon^{\mu\nu}\int\frac{d^4h}{(2\pi)^4}\frac{1}{h^2p_1^2[p_2^2-M_x^2][(h-l_l)^2-m^2]^2}\not{h}h_\mu h_\nu u(l_-) = \\
&\bar{v}(l_+)\gamma_\mu(l_+^\nu - l_-^\nu)u(l_-)\epsilon_{\mu\nu}\int\frac{d^4h}{(2\pi)^4}\frac{1}{h^2p_1^2[p_2^2-M_x^2][(h-l_l)^2-m^2]^2} \\
&\Big(-h^2+\frac{p_1^2+p_2^2}{2}\Big)\Big(-M^2-h^2-\frac{p_1^2p_2^2}{h^2}+p_1^2+p_2^2\Big), \qquad \text{(B.37)}
\end{aligned}$$

Applying this relation to the integral $\bar{I}_{5\mu\nu\alpha}$ after some algebraic manipulations one obtains the following result:

$$\begin{aligned}
\bar{I}_{5\mu\nu\alpha} &= 2(l_{l\alpha}g_{\mu\nu} + l_{l\nu}g_{\alpha\mu} + l_{l\mu}g_{\nu\alpha})\int d^4h\Bigg(\\
&\frac{1}{M^4}\frac{-2h\cdot l_l M_x^2 + 4h\cdot l_l M^2 + 8(h\cdot l_l)^2}{p_1^2[(h-l_l)^2-m^2]^2[p_2^2-M_x^2]} - \frac{1}{M^4}\frac{2h\cdot l_l}{p_1^2[(h-l_l)^2-m^2]^2} \\
&\frac{1}{M^4}\frac{4h\cdot l_k m^2 - h\cdot l_k M^2 + 4h\cdot l_l m^2 + h\cdot l_l M^2}{h^2[(h-l_l)^2-m^2]^2[p_2^2-M_x^2]} \\
&+\frac{1}{M^2}\frac{4h\cdot l_k - 2h\cdot l_l}{[(h-l_l)^2-m^2]^2[p_2^2-M_x^2]} + \frac{1}{M^4}\frac{4h\cdot l_k + 4h\cdot l_l}{[h^2(h-l_l)^2-m^2]^2[p_2^2-M_x^2]}\Bigg). \qquad \text{(B.38)}
\end{aligned}$$

Performing a shift of integration variable ($h \to \bar{h} + l_l$) the term $(\bar{h}\cdot l_l)^2$ is rewritten using the relation from Eq. B.25. Further algebraic manipulation allows to reduce the integral $\bar{I}_5$ to the form, where h appear in the numerator

only through the scalar product $h \cdot l_l$ in first power. The tensor integrals, which are contracted with l_l do not depend on it. The only momenta, which is involved in this integrals is l_k, so the tensor reduction can produce only terms proportional to $l_l \cdot l_k$, which is zero. Using the relation from Eq. B.6 one obtains the following:

$$\begin{aligned}
\bar{I}_{5\mu\nu\alpha} &= \frac{i\pi^2}{M^4}\Big(-2M_x^2 C_0(l_k^2,0,m^2,0,M_x^2) \\
&+(\frac{3}{3}m^2+\frac{2}{3}M_x^2-M^2)C_0(l_k^2,4l_k^2,m^2,0,M_x^2) \\
&-(2M_x^2m^2-\frac{1}{2}M^2M_x^2)\frac{\partial}{\partial m^2}C_0(l_k^2,4l_k^2,m^2,0,M_x^2) \\
&+(-\frac{13}{24}M^4-\frac{2}{3}m^4+\frac{2}{3}M_x^2m^2-M^2m^2+\frac{2}{3}M^2M_x^2) \\
&\frac{\partial}{\partial m^2}C_0(l_k^2,0,m^2,0,M_x^2)+\frac{4}{3}\frac{\partial}{\partial m^2}A_0(m^2) \\
&+(\frac{2}{3}m^2+\frac{2}{3}M^2)\frac{\partial}{\partial m^2}B_0(l_k^2,0,m^2)+\frac{2}{3}B_0(l_k^2,0,m^2)-\frac{2}{3}B_0(4l_k^2,0,M_x^2) \\
&-(2m^2+\frac{1}{2}M^2)\frac{\partial}{\partial m^2}B_0(l_l^2,0,m^2)-2B_0(l_l^2,0,m^2)+\frac{2}{3}B_0(l_k^2,M_x^2,m^2) \\
&+(\frac{2}{3}m^2+\frac{4}{3}M_x^2+\frac{2}{3}M^2)\frac{\partial}{\partial m^2}B_0(l_k^2,M_x^2,m^2)\Big). \qquad \text{(B.39)}
\end{aligned}$$

B.3 Analytic expressions for scalar loop integrals

$$A_0(m^2) = m^2\Big(\Delta+1-\log\Big(m^2\Big)\Big), \qquad \text{(B.40)}$$

$$\begin{aligned}
B_0(l_l^2,0,m^2) &= \Delta-\Big(\log(l_k^2)-i\pi+\frac{m^2}{l_l^2}(\log(m^2/l_k^2)+i\pi) \\
&+ \frac{l_l^2-m^2}{l_l^2}(\log\Big(\frac{m^2-l_l^2}{l_k^2}\Big)+i\pi))-2\Big), \qquad \text{(B.41)}
\end{aligned}$$

$$\begin{aligned}
B_0(l_k^2,0,m^2) &= \Delta-\Big(\log(l_k^2)+\frac{m^2}{l_k^2}\log(m^2/l_k^2) \\
&+ \frac{l_k^2-m^2}{l_k^2}(\log\Big(\frac{m^2-l_k^2}{l_k^2}\Big)-i\pi)-2\Big), \qquad \text{(B.42)}
\end{aligned}$$

$$B_0(4l_k^2,0,M_x^2) = \Delta - \Big(\log(4l_k^2) + \frac{M_x^2}{4l_k^2}\log(\frac{M_x^2}{l_k^2}) + (1-\frac{M_x^2}{4l_k^2})(\log(1-\frac{M_x^2}{4l_k^2}) - i\pi) - 2\Big), \quad \text{(B.43)}$$

$$B_0(l_k^2,M_x^2,m^2) = \Delta + \log(1-y_1)(y1-1) + \log(1-y_2)(y1-2) - y_1\log(-y_1) - y_2\log(-y_1) - \log(l_k^2) + 2, \quad \text{(B.44)}$$

$$C_0(l_k^2,4l_k^2,0,m^2,0) = \log(1-m^2/l_k^2)\Big(\frac{1}{l_k^2} - \frac{2}{m^2+l_k^2} + \log(m^2/l_k^2)\Big(-\frac{1}{l_k^2} + \frac{1}{m^2+l_k^2}\Big) + \frac{2}{m^2+l_k^2}\log(2) + i\pi(\frac{1}{l_k^2} + \frac{1}{m^2+l_k^2})\Big), \quad \text{(B.45)}$$

$$C_0(l_k^2,0,m^2,0,M_x^2) = \frac{4}{M^2(2+2x-y)}\Big\{2\log 2 - x\log(x) + y/2\log(y/2) - (1-x)(\log(1-x)-i\pi) + (2-y/2)(\log(2-y/2)-i\pi) + \frac{-1-x+y}{2}\log(x) - \frac{1-x+y}{2}\log(y) - 2r\Big(\operatorname{arc\,tg}\Big(\frac{1-x+y}{2r}\Big) - \operatorname{arc\,tg}\Big(\frac{-1-x+y}{2r}\Big)\Big)\Big\}, \quad \text{(B.46)}$$

$$C_0(l_k^2,4l_k^2,m^2,0,M_x^2) = \frac{-1-x+y}{2}\log(x) + \frac{3+x-y}{2}\log(2+2x-y) - 2 + 2r_1\Big(\operatorname{arc\,tg}\Big(\frac{-1-x+y}{2r_1}\Big) - \operatorname{arc\,tg}\Big(-\frac{3+x-y}{2r_1}\Big)\Big), \quad \text{(B.47)}$$

where $\Delta = \frac{1}{\epsilon} - \gamma_E + \log(4\pi)$, $l_k^2 = M^2/4$, $x = \frac{4m^2}{M^2}$, $y = \frac{4m^2}{M_x^2}$ and

$$y_{1,2} = \frac{l_k^2 + M_x^2 - m^2 \pm \sqrt{(l_k^2+M_x^2-m^2)^2 - 4M_x^2 l_k^2}}{2l_k^2}, \quad \text{(B.48)}$$

$$r = \sqrt{x - (1 - y + x)^2/4}, \tag{B.49}$$

$$r_1 = \sqrt{x - (1 + y - x)^2/4}. \tag{B.50}$$

Appendix C

Counter-terms and renormalization constants for virtual FSR corrections

The renormalization constants are extracted from the vertex correction and self-energy correction to the pion line. The one particle irreducible amplitude for the self-energy correction of the pion presented in he Fig. C.1 has the following form:

$$\mathcal{A}_{1PI} = \frac{\alpha}{4\pi^3}\int d^4q \frac{(P-q)^2}{(q^2-m_\pi^2)(q+P)^2}, \tag{C.1}$$

where P is a pion momentum and m_π is a pion mass. The integral, after Passarino-Veltman reduction takes the following form:

$$\mathcal{A}_{1PI} = \frac{\alpha}{4\pi}\Bigg(- A_0(m_\pi^2) + 2B_0(P^2,0,m_\pi^2)\Big(P^2+m_\pi^2\Big)\Bigg), \tag{C.2}$$

where A_0 and B_0 are scalar integrals defined according to the notation from [109].

The counter-term amplitude to the pion propagator has the following form:

$$\mathcal{A}_{P_c} = P^2\delta_4 - \delta_m, \tag{C.3}$$

where δ_4 is the pion field renormalization constant and δ_m is the pion mass renormalization constant.The on mass shell renormalization scheme is adopted. The renormalization conditions for the renormalized one particle irreducible amplitude $\bar{\mathcal{A}}_{1PI} = \mathcal{A}_{1PI} + \mathcal{A}_{P_c}$ have the following form:

$$\bar{\mathcal{A}}_{1PI}|_{P^2=m_\pi^2} = 0, \tag{C.4}$$

$$\frac{d\bar{\mathcal{A}}_{1PI}}{dP^2}|_{P^2=m_\pi^2} = 0. \tag{C.5}$$

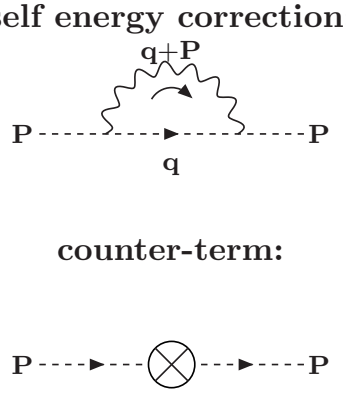

Figure C.1: Self energy correction to the pion line and propagator counter-term.

From the above conditions one obtains the following expressions for renormalization constants δ_4 and δ_m:

$$\delta_m = m_\pi^2\delta_4 - \frac{\alpha}{4\pi}\left(A_0(m_\pi^2) - 4m_\pi^2 B_0(m_\pi^2,0,m_\pi^2)\right), \tag{C.6}$$

$$\delta_4 = -\frac{\alpha}{\pi}\left(m_\pi^2\frac{dB_0(P^2,0,m_\pi^2)}{dP^2}|_{P^2=m_\pi^2} + \frac{1}{2}B_0(m_\pi^2,0,m_\pi^2).\right). \tag{C.7}$$

The pion-antipion-photon vertex corrections are represented by three diagrams from Fig. C.2. The amplitudes for this contributions have the following form:

$$\mathcal{A}_{v_1\mu} = \frac{i\alpha e}{4\pi^3}\int d^4q \frac{(2q-k+k')_\mu (q+2k)^\nu (q-2k')_\nu}{q^2[(q+k)^2-m_\pi^2][(q-k')-m_\pi^2]}, \tag{C.8}$$

$$\mathcal{A}_{v_2\mu} = \frac{i2\alpha e}{4\pi^3}\int d^4q \frac{(q-k')_\mu}{[q^2-m_\pi^2][q+k']^2}, \tag{C.9}$$

$$\mathcal{A}_{v_3\mu} = \frac{i2\alpha e}{4\pi^3}\int d^4q \frac{(q-k)_\mu}{[q^2-m_\pi^2][q+k]^2}, \tag{C.10}$$

$$\mathcal{A}_{v\mu} = \mathcal{A}_{v_1\mu} + \mathcal{A}_{v_2\mu} + \mathcal{A}_{v_3\mu}, \tag{C.11}$$

where k and k' are momenta of the pion and antipion. The amplitude $\mathcal{A}_v$ after Passarino-Veltman reduction and some simplifications take the following

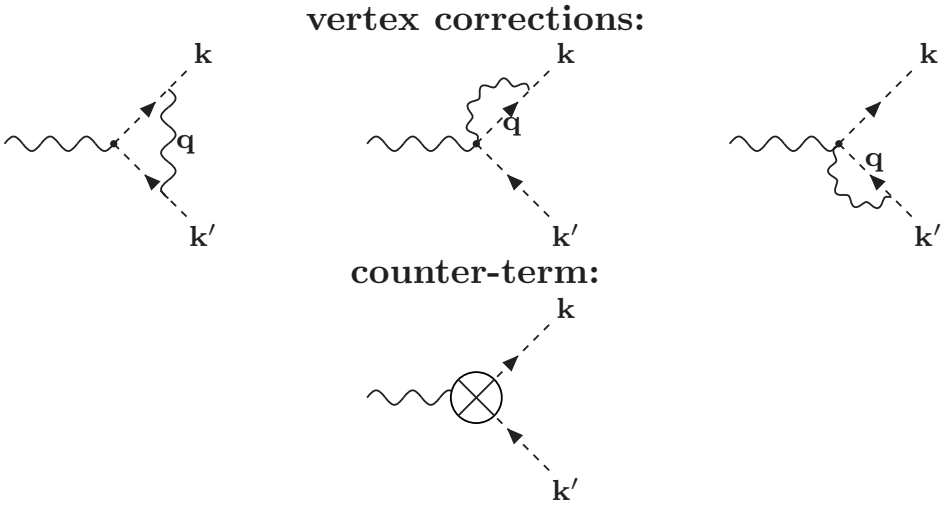

Figure C.2: Vertex corrections to the pion-antipion-photon interaction and vertex counter-term.

form:

$$\mathcal{A}_{v\mu} = \frac{i4\alpha e}{\pi(4m_\pi^2 - s)} k_\mu \Bigg(- sB_0(m_\pi^2, 0, m_\pi^2) + (2m_\pi^2 - s)\Big(- 2B_0(s, m_\pi^2 m_\pi^2) + (4m_\pi^2 - s)C_0(m_\pi^2, s, m_\pi^2, 0, m_\pi^2, m_\pi^2)\Big)\Bigg), \tag{C.12}$$

where $s = (k + k')^2$, B_0 and C_0 are scalar integrals defined according to the notation from [109]. The counter-term to the pion-antipion-photon vertex is also presented in Fig. C.2. It has the following form:

$$\mathcal{A}_{v_c\mu} = ie\Big(\frac{\delta_A}{2} + \delta_e + \delta_4\Big)k_\mu, \tag{C.13}$$

where δ_A is a renormalization constant of photon field and δ_3 is the renormalization constant of the charge. The renormalization condition for the renormalized vertex function $\bar{\mathcal{A}}_v = \mathcal{A}_v + \mathcal{A}_{v_c}$ has the following form:

$$\bar{\mathcal{A}}_v|_{s=0} = 0. \tag{C.14}$$

The above condition leads to the following expression for the combination

$\delta_A + 2\delta_e$, which enters the counter-term:

$$\begin{aligned}\delta_A + 2\delta_e &= \frac{\alpha}{\pi}\Bigg(B_0(0, m_\pi^2, m_\pi^2) - C_0(m_\pi^2, 0, m_\pi^2, 0, m_\pi^2, m_\pi^2) + B_0(m_\pi^2, 0, m_\pi^2) \\ &\quad + 2m_\pi^2 \frac{dB_0(P^2, 0, m_\pi^2)}{dk^2}|_{k^2=m_\pi^2}\Bigg). \end{aligned} \tag{C.15}$$

The separate expressions for δ_A and δ_e are not needed since the only combination of the renormalization constants, which is needed is the one given by the equation above. To obtain expressions for δ_A and δ_e separately one should include also the corrections to the self-energy of the photon, which is not considered in this thesis.

The scalar loop integrals A_0, B_0 and C_0, which are involved in the calculations of the renormalization constants have the following form:

$$A_0(M^2) = M^2\left(\Delta_{UV} + 1 - \log\left(\frac{M^2}{\mu^2}\right)\right), \tag{C.16}$$

$$B_0(0, M^2, M^2) = \Delta_{UV} - \log\left(\frac{M^2}{\mu^2}\right), \tag{C.17}$$

$$B_0(M^2, 0, M^2) = \Delta_{UV} + 2 - \log\left(\frac{M^2}{\mu^2}\right), \tag{C.18}$$

$$C_0(M^2, 0, M^2, 0, M^2, M^2) = \frac{1}{2M^2}\frac{(4\pi)^{\epsilon_{IR}}}{\epsilon_{IR}\Gamma(1-\epsilon_{IR})}\left(\frac{\mu^2}{M^2}\right)^{\epsilon_{IR}}, \tag{C.19}$$

$$\frac{dB_0(Q^2, 0, M^2)}{dQ^2} = -\frac{1}{Q^2}\left(1 + \frac{1}{2}\frac{(4\pi)^{\epsilon_{IR}}}{\epsilon_{IR}\Gamma(1-\epsilon_{IR})}\left(\frac{\mu^2}{Q^2}\right)^{\epsilon_{IR}}\right), \tag{C.20}$$

where $\Delta_{UV} = \frac{1}{\epsilon_{UV}} - \gamma_E + \log(4\pi)$.

Appendix D

Experimental event selections for the reaction $e^+e^- \longrightarrow \pi^+\pi^-\gamma$

KLOE:

- $\sqrt{s} = 1.02$ GeV
- Pion tracks: $50^o < \theta_{\pi^\pm} < 130^o$, $|p_{z_{\pi^\pm}}| > 90$ MeV
- Missing photon angle: $|\cos\theta_\gamma| > \cos 15^o$
- $q^2 \in (0.35, 0.95)$
- Track mass: $m_{trk} > 130$ MeV.

$$m_{trk} = \sqrt{\frac{a^2 - |\vec{q_1}|^2|\vec{q_2}|^2}{2a + |\vec{q_1}|^2 + |\vec{q_2}|^2}}, \tag{D.1}$$

$$a = \frac{1}{2}\Big((|\vec{q_1} + \vec{q_2}| - \sqrt{s})^2 - |\vec{q_1}|^2 - |\vec{q_2}|^2\Big), \tag{D.2}$$

  where q_1 and q_2 are the pion and the antipion momenta.

BES:

- $\sqrt{s} = 3.773$ GeV
- Pion tracks: $22.9^o < \theta_{\pi^\pm} < 157.1^o$, $|p_{T_{\pi^\pm}}| > 300$ MeV
- Minimal photon energy: $E_\gamma > 400$ MeV
- Missing photon angle: $|\cos\theta_\gamma| < 0.8$ or $0.86 < |\cos\theta_\gamma| < 0.92$
- $q^2 \in (0.35, 0.95)$

BABAR:

- $\sqrt{s} = 10.56$ GeV
- Pion tracks: $20^o < \theta_{\pi^\pm} < 160^o$, $|p_{T_{\pi^\pm}}| > 300$ MeV
- Minimal photon energy: $E_\gamma > 3$ GeV
- Missing photon angle: $20^o < \theta_\gamma < 160^o$
- $|q_1| > 1$ GeV (π^-) and $|q_2| > 1$ GeV (π^+)
- $q^2 \in (0.35, 0.95)$

Bibliography

[1] Georges Aad et al. Observation of a new particle in the search for the Standard Model Higgs boson with the ATLAS detector at the LHC. *Phys. Lett.*, B716:1–29, 2012.

[2] S. Actis et al. Quest for precision in hadronic cross sections at low energy: Monte Carlo tools vs. experimental data. *Eur. Phys. J.*, C66:585–686, 2010.

[3] Alexander Keshavarzi, Daisuke Nomura, and Thomas Teubner. Muon $g-2$ and $\alpha(M_Z^2)$: a new data-based analysis. *Phys. Rev.*, D97(11):114025, 2018.

[4] Michel Davier, Andreas Hoecker, Bogdan Malaescu, and Zhiqing Zhang. Reevaluation of the hadronic vacuum polarisation contributions to the Standard Model predictions of the muon g-2 and alpha(mZ) using newest hadronic cross-section data. 2017.

[5] Gilberto Colangelo, Martin Hoferichter, Bastian Kubis, Massimiliano Procura, and Peter Stoffer. Towards a data-driven analysis of hadronic light-by-light scattering. *Phys. Lett.*, B738:6–12, 2014.

[6] Randolf Pohl, Ronald Gilman, Gerald A. Miller, and Krzysztof Pachucki. Muonic hydrogen and the proton radius puzzle. *Ann. Rev. Nucl. Part. Sci.*, 63:175–204, 2013.

[7] Henryk Czy, Johann H. Khn, and Szymon Tracz. Nucleon form factors and final state radiative corrections to $e^+e^- \to p\bar{p}$. *Phys. Rev.*, D90(11):114021, 2014.

[8] Szymon Tracz and Henryk Czyż. χ_{c_1} and χ_{c_2} Production in e^+e^- Annihilation. *Acta Phys. Polon.*, B46(11):2273, 2015.

[9] Henryk Czyz, Johann H. Khn, and Szymon Tracz. χ_{c1} and χ_{c2} production at e^+e^- colliders. *Phys. Rev.*, D94(3):034033, 2016.

[10] Henryk Czyż, P. Kisza, and S. Tracz. Two-photon Transition Form Factors of Pseudoscalar Mesons in the PHOKHARA and the EKHARA Generators. *Acta Phys. Polon.*, B48:2197, 2017.

[11] Henryk Czy, Patrycja Kisza, and Szymon Tracz. Modeling interactions of photons with pseudoscalar and vector mesons. *Phys. Rev.*, D97(1):016006, 2018.

[12] F. Campanario, H. Czyż, J. Gluza, T Jeliński, G. Rodrigo, S. Tracz, and D. Zhuridov. Complete NLO radiative corrections to the reaction $e^+e^- \to \pi^+\pi^-\gamma$ and their implementation in the Monte Carlo event generator PHOKHARA(in preparation).

[13] Henryk Czyż, Patrycja Kisza, and Szymon Tracz. Monte Carlo generators for hadron physics: updates on PHOKHARA and EKHARA generators. *EPJ Web Conf.*, 142:01010, 2017.

[14] M. N. Rosenbluth. High Energy Elastic Scattering of Electrons on Protons. *Phys. Rev.*, 79:615–619, 1950.

[15] A. I. Akhiezer and Mikhail.P. Rekalo. Polarization phenomena in electron scattering by protons in the high energy region. *Sov. Phys. Dokl.*, 13:572, 1968. [Dokl. Akad. Nauk Ser. Fiz.180,1081(1968)].

[16] Norman Dombey. Scattering of polarized leptons at high energy. *Rev. Mod. Phys.*, 41:236–246, 1969.

[17] J. Arrington. How well do we know the electromagnetic form-factors of the proton? *Phys. Rev.*, C68:034325, 2003.

[18] Carl E. Carlson and Marc Vanderhaeghen. Two-Photon Physics in Hadronic Processes. *Ann. Rev. Nucl. Part. Sci.*, 57:171–204, 2007.

[19] M. Vanderhaeghen. Two-photon physics. *Few Body Syst.*, 41:103–115, 2007.

[20] Marc Vanderhaeghen. Overview of nucleon structure studies. *Nucl. Phys.*, A805:210–220, 2008.

[21] J. P. Lees et al. Study of $e^+e^- \to p\bar{p}$ via initial-state radiation at BABAR. *Phys. Rev.*, D87(9):092005, 2013.

[22] Szymon Tracz and Henryk Czyż. FSR Corrections to the Process $e^+e^- \to \bar{p}p\gamma$. *Acta Phys. Polon.*, B44(11):2281–2287, 2013.

[23] G. Peter Lepage and Stanley J. Brodsky. Exclusive Processes in Perturbative Quantum Chromodynamics. *Phys. Rev.*, D22:2157, 1980.

[24] J. Beringer et al. Review of Particle Physics (RPP). *Phys. Rev.*, D86:010001, 2012.

[25] Henryk Czyż, Agnieszka Grzelinska, and Johann H. Kühn. Narrow resonances studies with the radiative return method. *Phys. Rev.*, D81:094014, 2010.

[26] C. A. Dominguez. Pion form-factor in large N(c) QCD. *Phys. Lett.*, B512:331–334, 2001.

[27] V. Punjabi et al. Proton elastic form-factor ratios to $Q^2 = 3.5 - GeV^2$ by polarization transfer. *Phys. Rev.*, C71:055202, 2005. [Erratum: Phys. Rev.C71,069902(2005)].

[28] O. Gayou et al. Measurement of G(Ep) / G(Mp) in polarized-e p $\rightarrow$ e polarized-p to $Q^2 = 5.6 - GeV^2$. *Phys. Rev. Lett.*, 88:092301, 2002.

[29] O. Gayou et al. Measurements of the elastic electromagnetic form-factor ratio mu(p) G(Ep) / G(Mp) via polarization transfer. *Phys. Rev.*, C64:038202, 2001.

[30] A. J. R. Puckett et al. Recoil Polarization Measurements of the Proton Electromagnetic Form Factor Ratio to $Q^2 = 8.5 GeV^2$. *Phys. Rev. Lett.*, 104:242301, 2010.

[31] T. Pospischil et al. Measurement of G(E(p))/G(M(p)) via polarization transfer at $Q^2 = 0.4 - GeV/c^2$. *Eur. Phys. J.*, A12:125–127, 2001.

[32] G. Bardin et al. Determination of the electric and magnetic form-factors of the proton in the timelike region. *Nucl. Phys.*, B411:3–32, 1994.

[33] R. Madey et al. Measurements of G(E)n / G(M)n from the H-2(polarized-e,e-prime polarized-n) reaction to $Q^2 = 1.45 (GeV/c)^2$. *Phys. Rev. Lett.*, 91:122002, 2003.

[34] E. Geis et al. The Charge Form Factor of the Neutron at Low Momentum Transfer from the H-2-polarized (e-polarized, e-prime n) p Reaction. *Phys. Rev. Lett.*, 101:042501, 2008.

[35] D. Bisello et al. A Measurement of $e^+e^- \rightarrow \bar{p}p$ for 1975-MeV $\leqslant \sqrt{s} \leqslant$ 2250-MeV. *Nucl. Phys.*, B224:379, 1983.

[36] D. Bisello et al. Baryon pair production in e+ e- annihilation at $S^(1/2) = 2.4 - GeV$. *Z. Phys.*, C48:23–28, 1990.

[37] M. Ablikim et al. Measurement of the cross section for $e^+e^- \to$ p anti-p at center-of-mass energies from 2.0-GeV to 3.07-GeV. *Phys. Lett.*, B630:14–20, 2005.

[38] T. K. Pedlar et al. Precision measurements of the timelike electromagnetic form-factors of pion, kaon, and proton. *Phys. Rev. Lett.*, 95:261803, 2005.

[39] A. Antonelli et al. The first measurement of the neutron electromagnetic form-factors in the timelike region. *Nucl. Phys.*, B517:3–35, 1998.

[40] B. Delcourt et al. Study of the Reaction $e^+e^- \to p\bar{p}$ in the Total Energy Range 1925-MeV - 2180-MeV. *Phys. Lett.*, 86B:395–398, 1979.

[41] M. Castellano, G. Di Giugno, J. W. Humphrey, E. Sassi Palmieri, G. Troise, U. Troya, and S. Vitale. The reaction $e^+e^- \to$ p anti-p at a total energy of 2.1 gev. *Nuovo Cim.*, A14:1–20, 1973.

[42] G. Bardin et al. Measurement of the proton electromagnetic form-factor near threshold in the timelike region. *Phys. Lett.*, B255:149–154, 1991.

[43] G. Bardin et al. Precise determination of the electromagnetic form-factor of the proton in the timelike region up to $s = 4.2 - GeV^2$. *Phys. Lett.*, B257:514–518, 1991.

[44] T. A. Armstrong et al. Measurement of the proton electromagnetic form-factors in the timelike region at $8.9 - GeV^2 - 13 - GeV^2$. *Phys. Rev. Lett.*, 70:1212–1215, 1993.

[45] M. Ambrogiani et al. Measurements of the magnetic form-factor of the proton in the timelike region at large momentum transfer. *Phys. Rev.*, D60:032002, 1999.

[46] M. Andreotti et al. Measurements of the magnetic form-factor of the proton for timelike momentum transfers. *Phys. Lett.*, B559:20–25, 2003.

[47] L. Andivahis et al. Measurements of the electric and magnetic form-factors of the proton from $Q^2 = 1.75 - GeV/c^2 to 8.83 - GeV/c^2$. *Phys. Rev.*, D50:5491–5517, 1994.

[48] F. James and M. Roos. Minuit: A System for Function Minimization and Analysis of the Parameter Errors and Correlations. *Comput. Phys. Commun.*, 10:343–367, 1975.

[49] Henryk Czyz, Johann H. Kühn, Elzbieta Nowak, and German Rodrigo. Nucleon form-factors, B meson factories and the radiative return. *Eur. Phys. J.*, C35:527–536, 2004.

[50] Henryk Czyz, Agnieszka Grzelinska, Johann H. Kühn, and German Rodrigo. The Radiative return at phi and B factories: FSR for muon pair production at next-to-leading order. *Eur. Phys. J.*, C39:411–420, 2005.

[51] H. Czyz, M. Gunia, and J. H. Kühn. Simulation of electron-positron annihilation into hadrons with the event generator PHOKHARA. *JHEP*, 08:110, 2013.

[52] F. Campanario, H. Czy, J. Gluza, M. Gunia, T. Riemann, G. Rodrigo, and V. Yundin. Complete QED NLO contributions to the reaction $e^+e^- \to \mu^+\mu^-\gamma$ and their implementation in the event generator PHOKHARA. *JHEP*, 02:114, 2014.

[53] Fred Jegerlehner and Karol Kolodziej. The Hard bremsstrahlung correction to $e^+e^- \to 4f$ with finite fermion masses: Results for $e^+e^- \to$ u anti-d muon- anti-neutrino(muon). *Eur. Phys. J.*, C12:77–86, 2000.

[54] K. Kolodziej and M. Zralek. Helicity amplitudes for spin 0 or spin 1 boson production in e+ e- annihilation. *Phys. Rev.*, D43:3619–3625, 1991.

[55] J. Kaplan and Johann H. Kühn. Direct Production of 1^{++} States in e^+e^- Annihilation. *Phys. Lett.*, 78B:252–258, 1978.

[56] Johann H. Kühn, Jean Kaplan, and El Ghali Oudrhiri Safiani. Electromagnetic Annihilation of e+ e- Into Quarkonium States with Even Charge Conjugation. *Nucl. Phys.*, B157:125–144, 1979.

[57] Y. Lepetre and F. M. Renard. Two-photon terms in e^+e^- annihilation into $\pi\pi$ and $K\bar{K}$. *Lett. Nuovo Cim.*, 5S2(2):117–124, 1972. [Lett. Nuovo Cim.5S2,no.8,640(1972)].

[58] Deshan Yang and Shuai Zhao. $\chi_{QJ} \to l^+l^-$ within and beyond the Standard Model. *Eur. Phys. J.*, C72:1996, 2012.

[59] Chen-Ning Yang. Selection Rules for the Dematerialization of a Particle Into Two Photons. *Phys. Rev.*, 77:242–245, 1950.

[60] E. Eichten, K. Gottfried, T. Kinoshita, K. D. Lane, and Tung-Mow Yan. Charmonium: The Model. *Phys. Rev.*, D17:3090, 1978. [Erratum: Phys. Rev.D21,313(1980)].

[61] K. A. Olive et al. Review of Particle Physics. *Chin. Phys.*, C38:090001, 2014.

[62] Achim Denig, Feng-Kun Guo, Christoph Hanhart, and Alexey V. Nefediev. Direct X(3872) production in e^+e collisions. *Phys. Lett.*, B736:221–225, 2014.

[63] N. Kivel and M. Vanderhaeghen. $\chi_{cJ} \to e^+e^-$ decays revisited. *JHEP*, 02:032, 2016.

[64] Henryk Czyz and Johann H. Kühn. Strong and Electromagnetic J/psi and psi(2S) Decays into Pion and Kaon Pairs. *Phys. Rev.*, D80:034035, 2009.

[65] Henryk Czyż, Sergiy Ivashyn, Alexandr Korchin, and Olga Shekhovtsova. Two-photon form factors of the π^0, η and η' mesons in the chiral theory with resonances. *Phys. Rev.*, D85:094010, 2012.

[66] M. Benayoun, P. David, L. DelBuono, and F. Jegerlehner. Muon $g-2$ estimates: can one trust effective Lagrangians and global fits? *Eur. Phys. J.*, C75(12):613, 2015.

[67] M. Benayoun, P. David, L. DelBuono, and F. Jegerlehner. Upgraded Breaking Of The HLS Model: A Full Solution to the $\tau^-e^+e^-$ and ϕ Decay Issues And Its Consequences On g-2 VMD Estimates. *Eur. Phys. J.*, C72:1848, 2012.

[68] M. Benayoun, P. David, L. DelBuono, and F. Jegerlehner. An Update of the HLS Estimate of the Muon g-2. *Eur. Phys. J.*, C73:2453, 2013.

[69] G. Ecker, J. Gasser, H. Leutwyler, A. Pich, and E. de Rafael. Chiral Lagrangians for Massive Spin 1 Fields. *Phys. Lett.*, B223:425–432, 1989.

[70] G. Ecker, J. Gasser, A. Pich, and E. de Rafael. The Role of Resonances in Chiral Perturbation Theory. *Nucl. Phys.*, B321:311–342, 1989.

[71] Joaquim Prades. Massive spin 1 field chiral Lagrangian from an extended Nambu-Jona-Lasinio model of QCD. *Z. Phys.*, C63:491–506, 1994. [Erratum: Z. Phys.C11,571(1999)].

[72] Thorsten Feldmann. Quark structure of pseudoscalar mesons. *Int. J. Mod. Phys.*, A15:159–207, 2000.

[73] T. Feldmann, P. Kroll, and B. Stech. Mixing and decay constants of pseudoscalar mesons. *Phys. Rev.*, D58:114006, 1998.

[74] J. Wess and B. Zumino. Consequences of anomalous Ward identities. *Phys. Lett.*, 37B:95–97, 1971.

[75] Edward Witten. Global Aspects of Current Algebra. *Nucl. Phys.*, B223:422–432, 1983.

[76] S. Uehara et al. Measurement of $\gamma\gamma^* \to \pi^0$ transition form factor at Belle. *Phys. Rev.*, D86:092007, 2012.

[77] H. J. Behrend et al. A Measurement of the pi0, eta and eta-prime electromagnetic form-factors. *Z. Phys.*, C49:401–410, 1991.

[78] J. Gronberg et al. Measurements of the meson - photon transition form-factors of light pseudoscalar mesons at large momentum transfer. *Phys. Rev.*, D57:33–54, 1998.

[79] P. del Amo Sanchez et al. Measurement of the $\gamma\gamma^* \to \eta$ and $\gamma\gamma* \to \eta'$ transition form factors. *Phys. Rev.*, D84:052001, 2011.

[80] M. N. Achasov et al. Study of the $e^+e^- \to \eta\gamma$ process with SND detector at the VEPP-2M e+ e- collider. *Phys. Rev.*, D74:014016, 2006.

[81] M. N. Achasov et al. Study of the reaction $e^+e^- \to \pi^0\gamma$ with the SND detector at the VEPP-2M collider. *Phys. Rev.*, D93(9):092001, 2016.

[82] R. R. Akhmetshin et al. Study of the processes $e^+e^- \to \eta\gamma$, $\pi^0\gamma \to 3\gamma$ in the c.m. energy range 600-MeV to 1380-MeV at CMD-2. *Phys. Lett.*, B605:26–36, 2005.

[83] Bernard Aubert et al. Measurement of the eta and eta-prime transition form-factors at $q^2 = 112 - GeV^2$. *Phys. Rev.*, D74:012002, 2006.

[84] P. Adlarson et al. Measurement of the $\pi^0 \to e^+e^-\gamma$ Dalitz decay at the Mainz Microtron. *Phys. Rev.*, C95(2):025202, 2017.

[85] P. Adlarson et al. Measurement of the $\omega \to \pi^0 e^+ e^-$ and $\eta \to e^+ e^- \gamma$ Dalitz decays with the A2 setup at MAMI. *Phys. Rev.*, C95(3):035208, 2017.

[86] M. Ablikim et al. Observation of the Dalitz Decay $\eta' \to \gamma e^+ e^-$. *Phys. Rev.*, D92(1):012001, 2015.

[87] A. Anastasi et al. Measurement of the $\phi \to \pi^0 e^+ e^-$ transition form factor with the KLOE detector. *Phys. Lett.*, B757:362–367, 2016.

[88] D. Babusci et al. Study of the Dalitz decay $\phi \to \eta e^+ e^-$ with the KLOE detector. *Phys. Lett.*, B742:1–6, 2015.

[89] B. M. K. Nefkens et al. New measurement of the rare decay $\eta \to \pi^0 \gamma\gamma$ with the Crystal Ball/TAPS detectors at the Mainz Microtron. *Phys. Rev.*, C90(2):025206, 2014.

[90] C. Patrignani et al. Review of Particle Physics. *Chin. Phys.*, C40(10):100001, 2016.

[91] Bernard Aubert et al. Measurement of the $\gamma\gamma^* \to \pi^0$ transition form factor. *Phys. Rev.*, D80:052002, 2009.

[92] R. Arnaldi et al. Precision study of the $\eta \to \mu^+ \mu^- \gamma$ and $\omega \to \mu^+ \mu^- \pi^0$ electromagnetic transition form-factors and of the $\rho \to \mu^+ \mu^-$ line shape in NA60. *Phys. Lett.*, B757:437–444, 2016.

[93] German Rodrigo, Henryk Czyż, Johann H. Kühn, and Marcin Szopa. Radiative return at NLO and the measurement of the hadronic cross-section in electron positron annihilation. *Eur. Phys. J.*, C24:71–82, 2002.

[94] Bernard Aubert et al. Precise measurement of the e+ e- —¿ pi+ pi- (gamma) cross section with the Initial State Radiation method at BABAR. *Phys. Rev. Lett.*, 103:231801, 2009.

[95] A. Anastasi et al. Combination of KLOE $\sigma\Big(e^+e^- \to \pi^+\pi^-\gamma(\gamma)\Big)$ measurements and determination of $a_\mu^{\pi^+\pi^-}$ in the energy range $0.10 < s < 0.95$ GeV^2. *JHEP*, 03:173, 2018.

[96] M. Ablikim et al. Measurement of the $e^+e \to \pi^+\pi$ cross section between 600 and 900 MeV using initial state radiation. *Phys. Lett.*, B753:629–638, 2016.

[97] M. N. Achasov et al. Update of the $e^+e^- \to \pi^+\pi^-$ cross-section measured by SND detector in the energy region 400-MeV ¡ $\sqrt{s}$ ¡ file1000-MeV. *J. Exp. Theor. Phys.*, 103:380–384, 2006. [Zh. Eksp. Teor. Fiz.130,437(2006)].

[98] R. R. Akhmetshin et al. Measurement of the $e^+e^- \to \pi^+\pi^-$ cross section with the CMD-2 detector in the 370 - 520-MeV c.m. energy range. *JETP Lett.*, 84:413–417, 2006. [Pisma Zh. Eksp. Teor. Fiz.84,491(2006)].

[99] R. R. Akhmetshin et al. High-statistics measurement of the pion form factor in the rho-meson energy range with the CMD-2 detector. *Phys. Lett.*, B648:28–38, 2007.

[100] R. R. Akhmetshin et al. Reanalysis of hadronic cross-section measurements at CMD-2. *Phys. Lett.*, B578:285–289, 2004.

[101] Henryk Czyz, Agnieszka Grzelinska, Johann H. Kühn, and German Rodrigo. The Radiative return at Phi and B factories: FSR at next-to-leading order. *Eur. Phys. J.*, C33:333–347, 2004.

[102] Ansgar Denner and S. Dittmaier. Reduction schemes for one-loop tensor integrals. *Nucl. Phys.*, B734:62–115, 2006.

[103] T. Binoth, J. Ph. Guillet, G. Heinrich, E. Pilon, and C. Schubert. An Algebraic/numerical formalism for one-loop multi-leg amplitudes. *JHEP*, 10:015, 2005.

[104] Francisco Campanario. Towards $pp \to VVjj$ at NLO QCD: Bosonic contributions to triple vector boson production plus jet. *JHEP*, 10:070, 2011.

[105] R. Keith Ellis and Giulia Zanderighi. Scalar one-loop integrals for QCD. *JHEP*, 02:002, 2008.

[106] Gerard 't Hooft and M. J. G. Veltman. Regularization and Renormalization of Gauge Fields. *Nucl. Phys.*, B44:189–213, 1972.

[107] R. Mertig, M. Bohm, and Ansgar Denner. FEYN CALC: Computer algebraic calculation of Feynman amplitudes. *Comput. Phys. Commun.*, 64:345–359, 1991.

[108] T. Hahn and M. Perez-Victoria. Automatized one loop calculations in four-dimensions and D-dimensions. *Comput. Phys. Commun.*, 118:153–165, 1999.

[109] Gerard 't Hooft and M. J. G. Veltman. Scalar One Loop Integrals. *Nucl. Phys.*, B153:365–401, 1979.

[110] J. A. M. Vermaseren. The Symbolic manipulation program FORM. 1992.